T-Junction Resonant Modulators and Detectors in CMOS

by Dinis Cheian

B.S. MASSACHUSETTS INSTITUTE OF TECHNOLOGY, CAMBRIDGE (2016)

Submitted to the
Department of Electrical Engineering and Computer Science
in Partial Fulfillment of the Requirements for the Degree of

Master of Engineering in Electrical Engineering and Computer Science

at the

Massachusetts Institute of Technology

September 2016

Author: ____
Department of Electrical Engineering and Computer Science
August 16, 2016

Certified by: ____
Prof. Rajeev Ram, Thesis Supervisor
August 16, 2016

Accepted by: ____
Christopher Terman, Chairman, Masters of Engineering Thesis Committee

T-Junction Resonant Modulators and Detectors in CMOS

by Dinis Cheian

Submitted to the Department of Electrical Engineering and Computer Science

August 16, 2016

in Partial Fulfillment of the Requirements for the Degree of Masters of Engineering in Electrical Engineering and Computer Science

ABSTRACT

Design of optical modulators and detectors is investigated. A new design idea is proposed for optical modulators – T-junction. The T-junction allows to decouple the Extinction Ratio from the Bandwidth and to optimize each separately. Initial T-junction modulator provides an increase in bandwidth – 13 GHz versus 3 GHz, for the previous designs. An analytical model is created and is verified against the experimental data of the T-junctions. The model is then used to optimize the modulators and to achieve a design operating at above 35 GHz.

The bandwidth increase with optical intensity is investigated in detectors. The unusual behavior is reproduced in Sentaurus. The severe depletion of the N and P regions is found to be responsible for the bandwidth variations. Increasing the doping of the P and N regions proves to successfully tackle the problem.

0. Table of Contents

0. Table of Contents 1
1. Introduction 4
    1.1. Argument for Optical Links 5
        1.1.1. General Overview of the Problem 6
        1.1.2. Future of Electrical Interconnects 8
        1.1.3. Optical Links 9
        1.1.4. Argument for CMOS compatible photonics 10
        1.1.5. Conclusions 11
    1.2. Modulators 12
        1.2.1. Device Types 13
        1.2.2. Ring Modulator Theory 14
        1.2.3. Various Types of PN Junctions 18
        1.2.4. State-of-the-Art Modulators 21
    1.3. Detectors 22
    1.4. Demonstrated Optical Links 25
    1.5. Summary 26
2. Modulators: Interleaved vs T-junctions 27
    2.1. The Waveguide 27
    2.2. Electrical Modeling 30
        2.2.1. The Parasitic RC 30
        2.2.2. Constant Capacitance 31
        2.2.3. Distributed RC 35
        2.2.4. The T-junction 38
        2.2.5. The Optical Limitations 41
    2.3. Conclusions 44
3. Modulators: Experimental Results, Simulation, and Optimization 45
    3.1. The Sentaurus Model 45
        3.1.1. Simulating the Modulators 47
    3.2. The Experimental Setup 50

  - 3.3. Results and Discussions 53
  - 3.4. Energy Optimization 61
  - 3.5. Geometry Optimization 64
  - 3.6. Conclusions 67
- 4. Detectors: Bandwidth’s Dependency on Intensity 69
  - 4.1. The Detector 70
  - 4.2. Sentaurus Model 70
  - 4.3. Analyzing the data 73
  - 4.4. Explaining the Effect 79
  - 4.5. Parasitics 86
  - 4.6. Conclusions 88
- 5. Summary and Future Work 90
  - 5.1. Modulators 90
  - 5.2. Detectors 92
- 6. Appendix A: Code Reference 94
  - 6.1. Modulator 94
    - 6.1.1. MATLAB_Theory_Doping_Optimization 94
    - 6.1.2. MATLAB_Theory_Geometry_Optimization 100
    - 6.1.3. MATLAB_Energy_Check 105
    - 6.1.4. MATLAB_ER_Check 105
    - 6.1.5. MATLAB_IL_Check 105
    - 6.1.6. MATLAB_Resistivity 105
    - 6.1.7. MATLAB_Sentaurus_Data_Analysis 106
    - 6.1.8. MATLAB_Take_FFT 107
    - 6.1.9. MATLAB_Experiment_Data_Analysis 107
    - 6.1.10. SENTAURUS_Draw_T_Junction 108
    - 6.1.11. SENTAURUS_Vary_w_spoke 110
    - 6.1.12. SENTAURUS_Vary_w_intrinsic 113
    - 6.1.13. SENTAURUS_Modulator 116
    - 6.1.14. SVISUAL_Extract_Data 119
  - 6.2. Detector 119
    - 6.2.1. MATLAB_Optical_Simulation_Data_Analysis 119

6.2.2. MATLAB_Electrical_Simulation_Data_Analysis 120
6.2.3. SENTAURUS_Optical_Simulation... 120
6.2.4. SENTAURUS_Electrical_Simulation 124
7. Bibliography 128

1. Introduction

In this thesis, we will discuss the design of devices composing an optical photonic link. One focus of this project will be simulating, designing and testing an optical modulator. Another part of the thesis will focus on design issues regarding optical detectors. These two devices are tightly connected since an optical modulator is the transmit (TX) device of a photonic link and a detector is the receive (RX) device. Moreover, these devices will be CMOS compatible, enabling the use of advanced CMOS processes.

An optical modulator is a device that converts electrical bits of information into optical bits. A modulator acts like a “faucet” for light, by changing the voltage at the terminals we can decide how much light will pass through, thus imitating electrical bits. Modulators can be manufactured using a variety of electro-optical material, we will focus on CMOS compatible modulators. Here the main application for optical modulators is communication between memory and logic, therefore it is essential for the modulators to be integrated with electronics. Developing CMOS compatible modulators will allow us to make use of high yield CMOS processes, this will decrease the cost and increase the reliability of our optical components. As in every system, we need to minimize the size and energy cost of a modulator. The target specs for our modulator will be 5 dB extinction ratio at 12-15 Gbps while using less than 1V peak-to-peak. The justification for these specs can be found later in this chapter.

An optical detector is the RX device in a photonic link. The detector is positioned at the RX side of the link and its role is opposite to that of the modulator. A detector detects the amount of light and outputs current proportional to the light detected. Since the modulator and the detector will ultimately be integrated as part of the same system, the detector needs to be at least as fast as the modulator. The detector also needs to be CMOS compatible. This will further increase the yield and will decrease the cost of the fabrication, as custom processes are expensive to develop and implement. The main focus of this thesis will be examining an unexpected behavior observed in detectors. While testing detectors we observed bandwidth variation with input power variation. This issue will be tackled in great detail in this project and design solutions will be developed.

The following section provides some background on optical links in general and stand-alone modulators and detectors. We'll start with the motivation for photonic links in Section 1.2, and discuss why the system needs to be CMOS integrated. Modulators and detectors will be discussed in Sections 1.3 and 1.4 respectively. State-of-the-art integrated photonic links will be discussed in Section 1.5.

1.1. Argument for Optical Links

The increasing number of transistor in logical elements and their increasing computational capabilities pose a serious challenge to interconnects. Up to 15 metal layers are currently used to provide off chip communication between memory and CPUs and I/Os and memory. The high density of the interconnect networks present a real problem since it is complicated to route. This leads to increased cross-talk and thus decreased bandwidth. In the past, CPUs turned out to be severely underused due to underperformance of the interconnects. Optical interconnects can provide a viable solution to this overgrowing problem. By implementing photonic links on chip we can reduce power and alleviate congestion problems.

1.1.1. General Overview of the Problem

Multicore processors have three main components: computation, clock distribution, and communication. The later group includes core-to-core communication, socket-to-socket communication, and core-to-memory communication. The main factor that dictates the tradeoffs between the subsystems is how much energy can be allocated for each of the components. Typical total power consumption is on the order of 100W and a standard breakdown would be: 60% for computation, 20% for clock distribution and on-chip communication, and 20% for the off-chip communication [1].

Today, when tested against a popular floating-point benchmark - Linpack HPL [2] , the limiting factor, of the CPU performance, is fetching and storing the data, not computing it. In the past the metal interconnects failed to exploit the full potential of the cores, using them only at about 50% of their full capacity [3]. The biggest challenge is the number of the I/O pins and the energy cost associated with I/O. Solutions such as increased cache size (Figure 1. Graph indicating increasing size of L2 and L3 caches with time to account for slow metal interconnects. Adapted from .) were deployed to make use of the full capacity of the cores. This is far from optimal, because the increased area of the cache decreases the amount of area that is left for the processors.

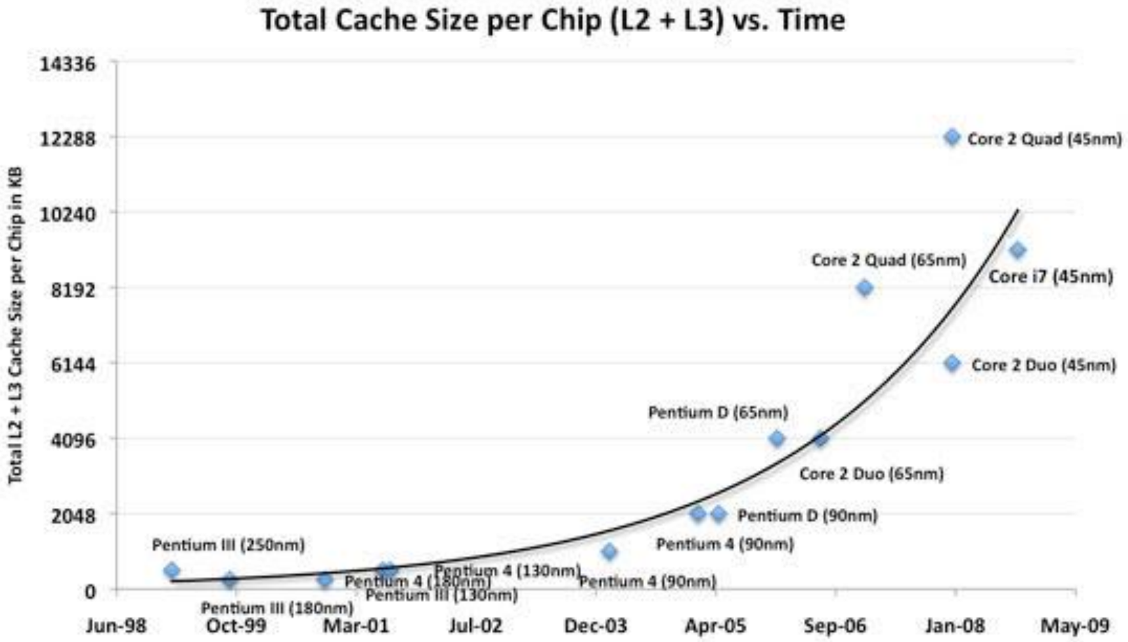

Figure 1. Graph indicating increasing size of L2 and L3 caches with time to account for slow metal interconnects. Adapted from [4].

A typical power consumption for a processor is 100 W, as the heat dissipation prevents us from going much higher [5]. Roughly 20% is reserved for the off-chip communications. Because the off-chip communication has to power the connectivity and the memory interface, roughly 10 W is available for memory interfacing. Modern computers, running memory intensive processes, have to maintain a 1 B/FLOP target speed [6], the read and write data paths each require 48 Tbit/s yielding a 96 Tbit/s for the optical links. The arguments above set a 10 W limit of power dissipation and 96 Tbit/s for the data transfer of the optical links.

1.1.2. Future of Electrical Interconnects

Now that we’ve defined the requirement for the interconnect system we can take a look at what the electrical interconnects promise to achieve in the near future. In the past, continuous scaling down of the transistor enabled faster and more energy efficient logic blocks. Unfortunately the bulky metal interconnect did not share this success. As the logic becomes faster, the interconnects often turn out to be the bottleneck for performance.

Although it is often believed that photonics will allow for increased bandwidth of the electrical networks, this is impractical. Photonic links will probably operate at the same bit rates as the electrical links. The reason being, that due to power hungry circuitry, to serialize or deserialize the signals, it is impractical to push the interconnect clock frequency much higher than that of the computational clock. To maintain energy efficiency, a photonic link of 12-15 Gbps is required [7].

The high channel density of the electrical interconnects is the main problem causing small off-chip bandwidth. A die of 1cm^2 is limited to approximately 10,000 pins for an overall package cost of $100. Approximately 2000 pins will be consumed for power delivery, of the rest about 4000 will be used for memory interfaces. Due to high bandwidth and signal integrity requirements, most of the signals are differential, resulting in 2000 communication channels. Given the above speed requirements this limits an electrical system to about 20 Tbit/s, very far away from the target 96Tbit/s [8].

The energy density of the grid is hard to predict. Today’s systems operate at well above 10 pJ/bit. A realistic estimate seems to be 5 pJ/bit to 10 pJ/bit in the near future.

Even if we allow some room for optimism and assume that the future electrical networks will operate at 1 pJ/bit to 2 pJ/bit this still yields a 48W to 96W of power, if we want to operate at 96 Tbit/s. Even this optimistic estimate is well above the target 10W.

From the above estimations we see that electrical connections fall short of meeting the power or the channel density specs. A 20Tbit/s instead of the required 96 Tbit/s is all the electrical connections will be able to provide. If we want to operate at 96Tbit/s we will have to support the prohibitively high cost of 96W of power. This suggest that we should seek alternatives to electrical interconnects.

1.1.3. Optical Links

The main advantage of an optical link is the possibility of wavelength-division multiplexing (WDM). This allows multiple signals, at different wavelengths, to share the same waveguide. 8-channel WDM banks have been demonstrated in the literature, with a theoretical maximum of 32. The cross-talk requirement between the channels of -20dB, which translates into 110 GHz separation, and the wavelength variation in a specific waveguide (around 20 nm) set the theoretical channel number at 32. This implies that the needed amount of channels could be scaled down by a factor of 32 when compared to electrical connections. A potential 32-channel WDM bank would allow for 250 fibers running through the chip, an amount achievable in the state-of-the-art single-mode fiber connectors [8].

The total photonic link energy that is predicted based on current state-of-the-art is approximately 200 fJ/bit, this includes 100 fJ/bit for thermal tuning of the components, 40 fJ/bit to drive the modulators and 60 fJ/bit to receive the signal. The total on-chip power dissipation sums up to around 9W just within the target 10W [8].

From the short analysis above, the photonic links promise a better alternative for interconnects than the electrical links. WDM allows for multiple data channels in one waveguide, reducing the amount of space necessary for routing. A crude analysis also promises 9W of power consumption at the required 96 Tbit/s bandwidth.

On top of that the optical links have to maintain a signal with at least a Bit Error Rate (BER) of 10^{-12} [9]. To achieve the desirable BER we can increase the ER or increase the laser power, it has been shown that the optimal ER, for saving power, is around 5dB [10].

1.1.4. Argument for CMOS compatible photonics

A number of photonic platforms have been demonstrated in III-V elements such as InGaAsP heterojunctions. These material have significant advantage when compared to silicon devices. One of the plusses is increased hole and electron mobility, meaning that the devices will be intrinsically faster. Another significant advantage is the direct bandgap thus allowing band transitions with only a photon, without an additional phonon required to adjust the momentum.

This thesis will focus primarily on CMOS compatible devices. Since the final application includes interconnects for electronics, it is important that the photonics is integrated on the same chip as the electronics. First of all, this allows higher yield, higher than 99% [11]. The yield for III-V devices is around 95% [12], which is good enough for single devices but can have disastrous consequences when targeting high volume integration. On top of low yield, the III-V devices require very expensive, custom fabrication processes to manufacture the photonic devices.

CMOS compatible devices have been demonstrated while modifying old CMOS processes. However, since the main application targets modern CPUs, the use of 5 year old CMOS processes is highly undesirable. Working in an up to date CMOS process implies a lot of constraints. The number of metal layers is restricted, thus complicating the integration of numerous photonic devices. The minimum width of elements is restricted. The depth of implants is fixed and optimized for MOSFETS, thus making it complicated to manufacture a vertical junction. Another important downside to standard CMOS is the restrictive set of masks, thus the doping of the devices cannot be controlled with arbitrary precision.

1.1.5. Conclusions

As a result of this short analysis we have identified the problem – modern logic is significantly faster than the interconnects. Electrical interconnects cannot meet the density of packaging requirement nor the power requirements in order to stay competitive in modern microelectronics. A clear candidate, photonic links, emerges. Optical communication promises better density and less power consumption at the right speed. Another important detail is that the photonics needs to be integrated with electronics, thus we need to use standard CMOS processes in order to achieve high yields and low costs.

1.2. Modulators

The optical modulator is the device that acts as the TX side in a photonic link. The modulator regulates the amount of light that passes through the waveguide. The main goal of the modulator is to convert electrical bits of information to optical bits of information. If the bit is “1” the modulator lets the light pass unattenuated, if the bit is “0” the modulator will absorb the light and less of it will be transmitted.

The light is modulated by applying a certain bias voltage at the terminals of the modulator. The change in bias causes the change in the width of depletion region and thus changes the volume density of charges. The concentration of carriers changes the refractive index changes due to the plasma dispersion effect. The amount of change is dictated by Soref’s equations [13], which at around 1150 nm takes the following form:

$$\Delta n = -(3.6 * 10^{-22} \Delta N_e + 3.5 * 10^{-18} \Delta N_h^{0.8});$$

The change in the refractive index (on the order of 10^{-3}) of the modulator will change the phase that the light acquires passing through the device. This allows transmission of less or more light depending on the bias voltage. There are two types of electrical modulation: injection and depletion. Since injection occurs during forward bias more carriers are injected into the junction and thus it takes more time to extract them, thus making injection slower than depletion: carrier depletion is better in terms of speed and thermal dissipation. However modulating by injection changes the number of carrier more significantly and thus the extinction ratio is bigger.

1.2.1. Device Types

There are also two different structures used to modulate the light. The first structure is a Mach–Zehnder interferometer (MZI). This is a device with two arms with light running through both of them (Figure 2a). By applying a bias voltage on one of the arms but not the other we create a phase difference between the two waves. The phase difference should be calibrated so the two waves interfere destructively at the exit of the modulator, where the two arms recombine.

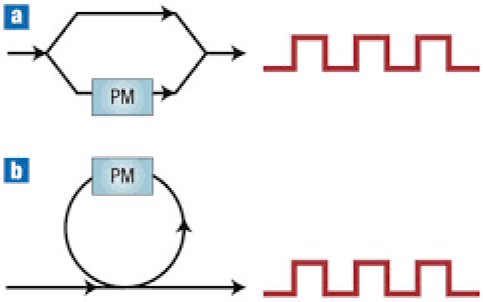

Figure 2. a) an MZI modulator consisting of two arms. The light is divided equally between the two arms and one of the arms is phase modulating (PM) the light, causing it two interfere constructively or destructively at the end of the MZI. b) an Optical Ring modulator, light is coupling into the ring and the PM imposed determines if the light interferes constructively or destructively with the light travelling through the waveguide [14].

MZIs where widely used when the research community just started building modulators. They are not very suitable for off-chip communications. First of all MZIs have a significantly bigger area than the ring modulators – 1000 um^2 vs 100 um^2. This is due to the fact that the electromagnetic wave through one of the legs of the MZI has to acquire a π phase relative to the other one. The phase shift between the two legs is:

$$\frac{2\pi L n_1}{\lambda} - \frac{2\pi L n_2}{\lambda} = \pi = \frac{\pi L \Delta n}{\lambda};$$

where L is the length of the arm. From Soref's equation, we can estimate that Δn is on the order of 10^{-3}. Thus to achieve a π phase shift at a typical $\lambda = 1500\ nm$, we need $L \propto 750\ \mu m$, which yields an area of around 1000 μm. The large size also comes with a significant power consumption, typically above 1 pJ/bit, which makes these type of modulators prohibitively power hungry for off-chip applications. The voltage required to obtain good extinction ratio (ER) is above 5V, which implies a higher CV^2 and thus a bigger energy consumption per bit. The advantage of the MZIs is that they are much faster, since they usually require higher voltages which reduces junction capacitance, than the optical rings. Nevertheless, as established in 1.1, we are not interested in bandwidths much higher than 15 Gbps. Overall MZIs are a bad choice of modulator design when targeting off-chip communication applications.

The Optical Ring (OR) is a second device suitable for modulator design. The ring is placed close to a waveguide (Figure 2b). As light travels through the waveguide it couples into the ring. The phase change that the light acquires after travelling around the ring determines if the waves will interfere constructively or destructively at the coupling point.

1.2.2. Ring Modulator Theory

The structure of the modulators that will be discussed in this paper is the optical ring design. As the light is travelling in the waveguide, some of the light couples inside the modulator (Figure 3).

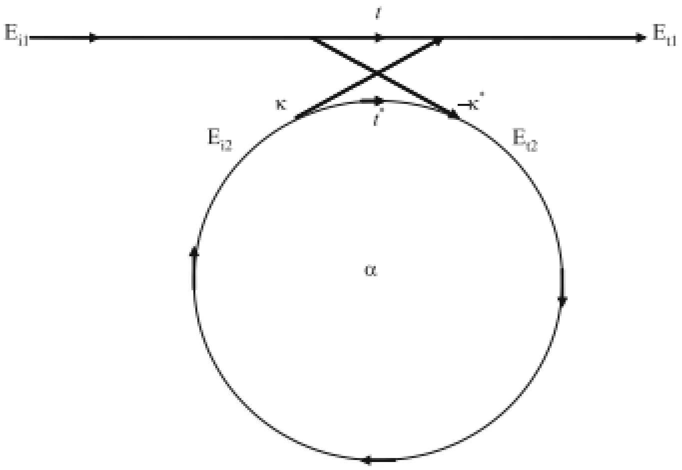

Figure 3. A ring modulator positioned next to a waveguide. As light travels through the waveguide it couples into the modulator [15].

The interaction between the modulator and the waveguide can be described through the following matrix:

$$\begin{pmatrix} E_{t1} \\ E_{t2} \end{pmatrix} = \begin{pmatrix} t & \kappa \\ -\kappa^* & t^* \end{pmatrix} \begin{pmatrix} E_{i1} \\ E_{i2} \end{pmatrix};$$

Where the mode amplitudes E, are normalized and consistent with Figure 3. t and κ are coupling coefficients and * denotes the complex conjugates. It can be shown [15] that:

$$P_{t1} = |E_{t1}|^2 = \frac{\alpha^2 + |t|^2 - 2\alpha|t|\cos(\theta + \varphi_t)}{1 + \alpha^2|t|^2 - 2\alpha|t|\cos(\theta + \varphi_t)};$$

Where α represents the loss in the ring, φ_t is the phase of the coupler and:

$$\theta = \frac{\omega L}{c} = k n_{eff} 2\pi r = \frac{4\pi^2 n_{eff} r}{\lambda};$$

The formula for P_{t1},at resonance, becomes:

$$P_{t1} = \frac{(\alpha - |t|)^2}{(1 - \alpha|t|)^2};$$

To minimize the transmission at resonance, we want to design rings where $\alpha = |t|$.

Figure 4 illustrates how the transmission changes with various |t|.

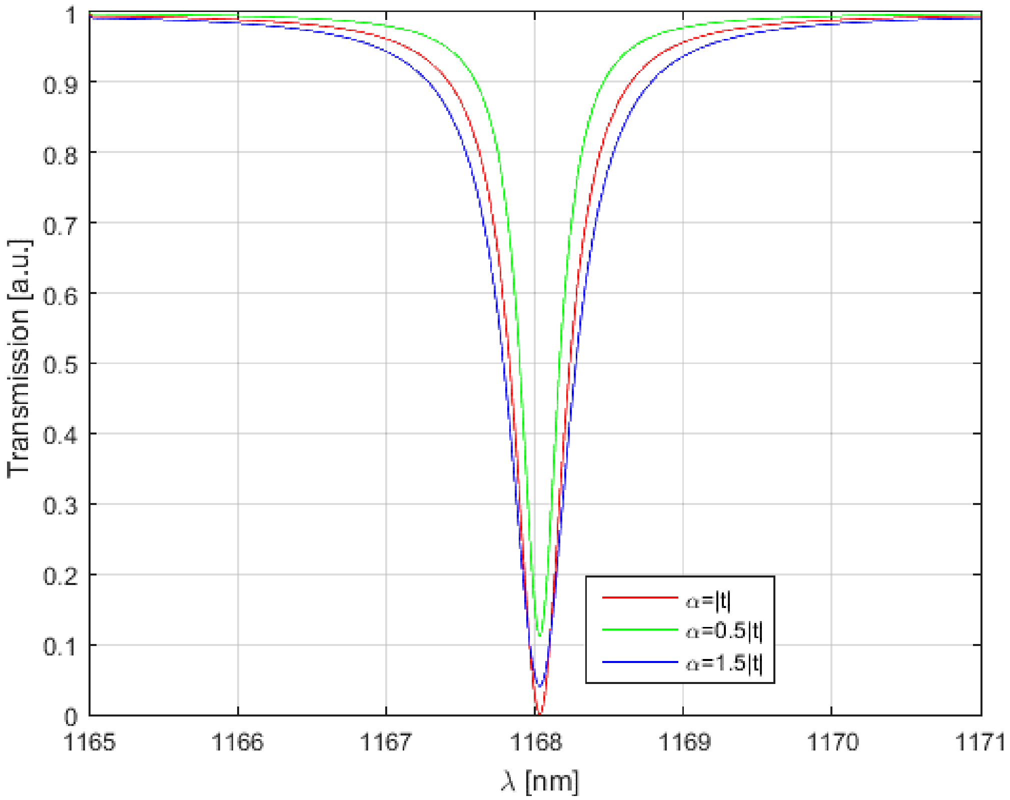

Figure 4. Transmission of a Critically Coupled, Under-coupled and Over-coupled ring. The transmission reaches 0 at resonance when $\alpha = |t|$.

As one would expect, the phase shift that the wave acquires, after one circle in the ring, reaches π at the resonant frequency (Figure 5).

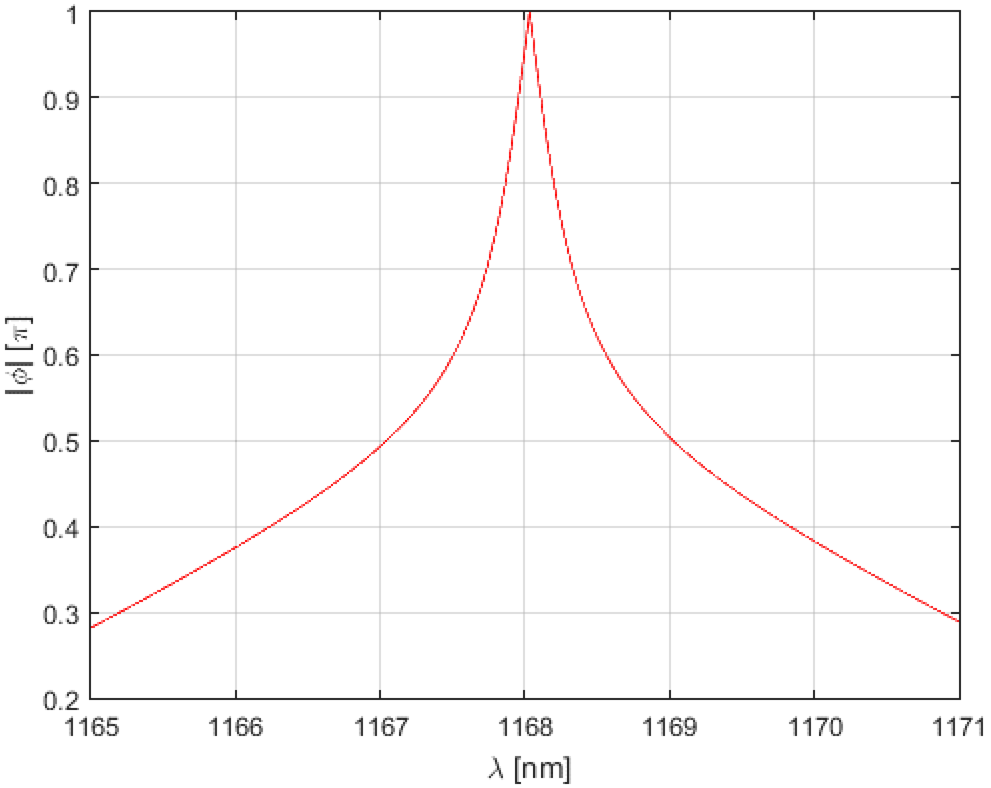

Figure 5. The phase difference after one circle in the ring reaches π, thus causing destructive interference at the coupling port.

Also, from the formula above we can clearly see the dependence of P_{t1} on n_{eff} which is the effective refractive index of the ring. P_{t1} is represented in Figure 6 as the wavelength varies. When we change the voltage applied at the terminals of the PN junctions we vary the width of the depletion region ($W \propto \sqrt{\varphi_{built} - V_{bias}}$) and thus change the carrier density in the device which leads to a change in the refractive index through the plasma dispersion effect.

Another important parameter that can be approximated from the P_{t1}versus λ plots is the Q factor of the ring. The quality factor is a measure of how lossy the ring is. Usually Q is defined as the energy stored in the ring divided by the energy lost during one cycle. In the case of optical rings, it is also important that Q suggests how narrow the absorption spectrum is: $Q = \frac{\lambda}{2\delta\lambda}$, where λ corresponds to the minimum of the transmission (1250nm for the blue curve in Figure 6) and $2\delta\lambda$ is the Full Width Half Maximum (FWHM) of the spectrum (around 0.05 nm for the curves in Figure 6). Thus the ring whose spectrum is illustrated in Figure 4 has a Q of around 25,000. The bigger the Q at a specific wavelength, the narrower the absorption spectrum is and thus we can have more WDM channels for a specific wavelength zone.

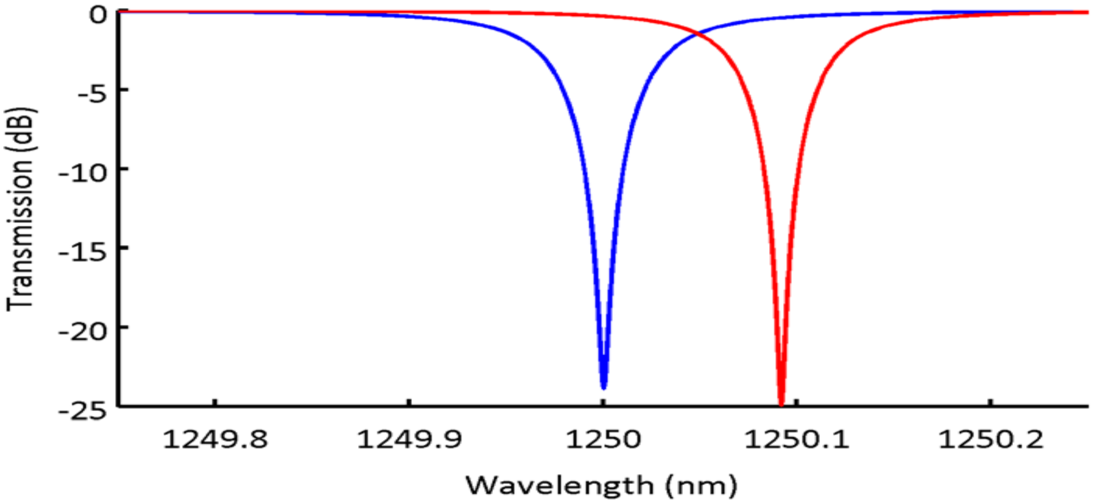

Figure 6. The transmission of the ring under various voltage bias.

1.2.3. Various Types of PN Junctions

When designing a ring modulator we can use various types of PN junction, each with its own tradeoffs. A designer must keep a small junction capacitance in order to create a fast device. However junction capacitance is required in order to obtain the needed 5 dB of ER. The width of the ring must also be big enough so to prevent the optical mode, travelling along the outer side of the device, from getting absorbed by the metal contacts, positioned inside the ring. The 3 most popular types of junctions are: lateral, interleaved and vertical junctions (Figure 7). The corresponding capacitances are specified below the pictures of the junctions. The calculations are performed for a width $W = 1\ \mu m$, thickness $H = 0.22\ \mu m$ and length of a single PN junctions of $L_{p-n} = 0.6\ \mu m$.

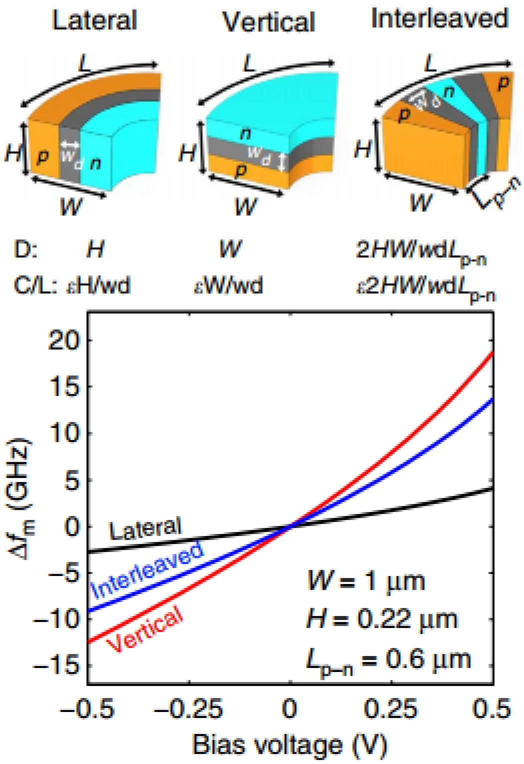

Figure 7. Different types of junction and the corresponding theoretical frequency performance [16].

When we change the bias voltage of a junction, we change its depletion region width and thus the excess of electrons and holes has either to be supplied or extracted from the junctions. From Figure 7 we can observe that the vertical junction is the fastest junction in reverse bias. This is due to the fact that the electrons and holes have to travel a small distance until they reach the depletion regions, thus encountering a smaller R and minimizing the RC delay, which sets the 3dB frequency. For a L_{p-n} of $0.6\ \mu m$, the slowest junction is the lateral junction, because the carriers that are travelling to the p region slow down the device significantly.

Even though the vertical junction has an advantage over other geometries, it is not possible to manufacture such a junction in a non-modified CMOS process. The reason is that the implants have a constant depth of penetration. It is possible to use the so-called “shallow implants” to achieve a vertical junction but the “shallow implants” are usually heavily doped and will significantly increase the optical losses due to free carrier absorption.

From a theoretical perspective the bandwidth is limited by the bias voltage, minimum width of the ring and maximum doping values. Higher bias voltages create a wider depletion region thus minimizing the capacitance ($C \propto \sqrt{\varphi - V_{bias}}$, where φ is the build in potential of the junction). From Figure 7 we can conclude that bandwidth increases at higher bias voltages, however this comes at an increased energy cost. On top of this, as already mentioned, the device has to possess some capacitance in order to have a significant ER ($ER \propto \Delta n \propto \frac{dQ}{dV} = C$). The minimum width of the junction as well as the finite doping have to be maintained in order to avoid excessive losses in the modulator. In Chapter 2 we will discuss another type of junction, the T-junction, which minimizes the RC, for higher bandwidth, and maximizes the capacitance seen by the optical mode, to provide a good ER. We will show that the bandwidth, of the T-junctions, is limited to around 25 – 30 GHz, due to the above mentioned tradeoffs.

1.2.4. State-of-the-Art Modulators

Table 1 summarizes the state-of-the-art modulators produced in the previous years. We can note that the MZIs are faster than the rings but at the same time consume much more power and require a significantly higher peak-to-peak voltage.

Table 1. Summary of the state-of-the-art modulators in Silicon.

Author	**Architecture**	**Junction**	**ER [dB]**	**Voltage [V]**	**Speed [Gbps]**	**Energy [fJ/bit]**
Green 2007 [17]	MZI	N/A	6	7.6	10	5000
Thomson 2012 [18]	MZI	N/A	3.1	6.5	50	4200
Xu 2007 [19]	Ring	Lateral	9	3.5	12.5	300
Watts 2011 [20]	Disk	Vertical	3	1	12.5	3
Shainline 2013 [21]	Ring	Interleaved	5.2	3	5	40
Wade 2014 [22]	Ring	Interleaved	5.2	3.6	5	40
Timurdogan 2014 [16]	Ring	Vertical	6.2	0.5	25	0.9
Alloatti 2016 [23] (This Work)	Ring	T-shaped	5	2.46	25	17.7

The best modulator reported so far is the one from Timurdogan et al., which makes use of the vertical junctions. The author used a ring modulator and achieved a 25 Gbps modulation at 0.5 V peak-to-peak which resulted in 0.9 fJ/bit. The high bandwidth of the device demonstrated in [16] is in good agreement with the analyses presented in Figure 7 that shows that the vertical junctions are the fastest for given geometric parameters. Unfortunately the device makes use of vertical junctions and thus it is not possible to manufacture in a standard CMOS process.

The primary goal of this thesis is to design and test a modulator which corresponds to the metrics listed in 1.2 but in the same time is CMOS compatible. The design of the PN junctions can also be useful for the design of the photodetectors.

1.3. Detectors

The detectors are the devices that are on the receiving side of a photonic link. Their role is opposite to those of the modulators – they convert optical bits into electrical bits. The detector senses light and outputs a proportional current, thus transferring the information to the electrical realm.

There are multiple ways of implementing a detector. One way would be to place the detector's sensing part directly in the waveguide. Once the light reaches the detector, current is generated and it is being sensed by the electronics. These detectors usually have transistor like shapes.

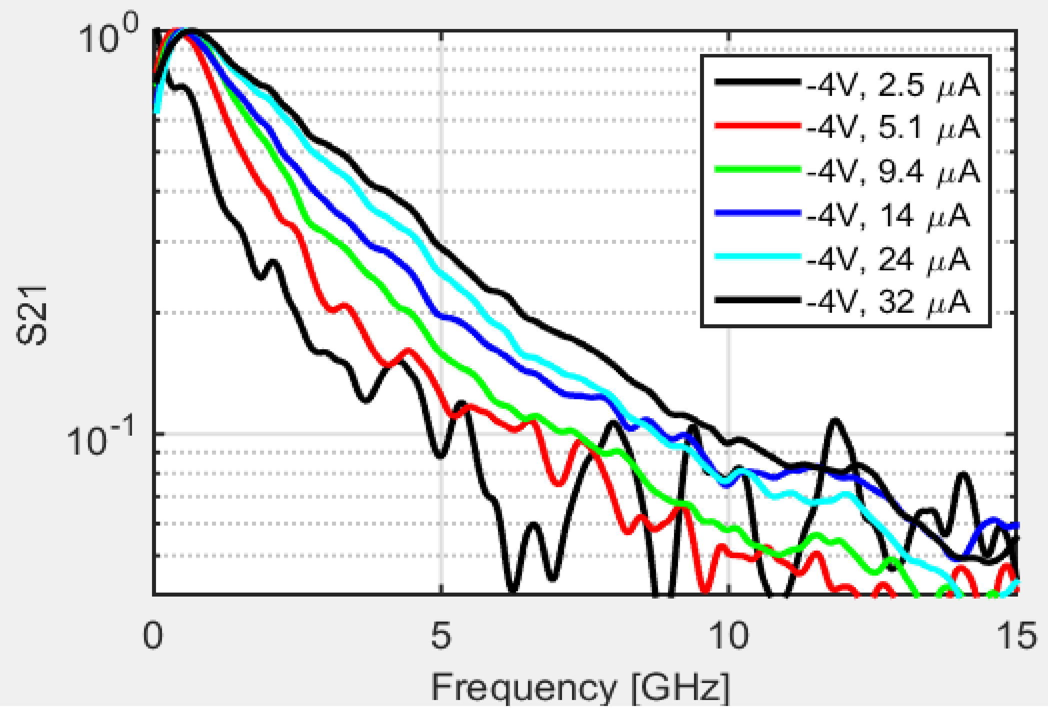

Figure 8. Measurement of the bandwidth of a detector versus frequency for different photo currents. The bandwidth increases as the laser power gets bigger. The bias is held at -4V and the photo current increases with incident laser power.

Another way to sense light in a waveguide is to place a ring detector next to the waveguide. If the light is of needed frequency it will couple in the detector and circulate inside until it gets absorbed. This will also generate current that can be read out and interpreted as data.

Table 2. Summary of the state-of-the-art detectors in standard CMOS.

Author	Lee 2010 [24]	Meng 2015 [25]	Chou 2013 [26]	Iiyama 2014 [27]	Alloatti 2016 [28]
Gain	28.4	1	15.4	10	1
Responsivity [A/W]	0.35	0.35	0.48	0.05	0.55
Bandwidth [GHz]	10	1	7.6	10	5
Bias Voltage [V]	10.0	25.0	10.25	8.3	4
Technology [nm]	130	45	180	180	45
Geometry	P^+/N-well	Ring (PN)	N^+/P-sub	N^+/P-well	Ring (PN)
Materials	Ge	SiGe	PolySi	PolySi	SiGe

Unlike the modulators we will not cover design of detectors from scratch. The problem that we will tackle here is the observed bandwidth increase with intensity of illumination. Figure 8 shows the data measured from a recently fabricated detector [28]. We can see that the 3dB frequency improves with higher laser power. Our goal will be to investigate the reasons for this and then to propose design solutions that will solve the problem. Analogous behavior has been observed in the literature, however it was demonstrated that it is due to trap saturation [29]. Once the intensity increases, the traps are filled and do not further slowdown the device. However in our device, the concentration of traps is very small because the dark current is only 20pA.

Table 2 presents state-of-the-art detectors. As can be observed the bias voltage for detectors is well above those for the modulators. This is one of the reasons why we reserve more power for detection rather than modulation.

1.4. Demonstrated Optical Links

Now that we have discussed the best modulators and detectors we have to take a look at the state-of-the-art optical links that have been demonstrated. This is more complex than just selecting the best modulator and detector and connecting them together. For example, some modulators are designed for 1180nm, in the same time some detectors are optimized at 1550nm. Not only the performance can degrade but the device might not operate at all at the needed frequency. A good example of this is a detector that makes use of the SiGe to sense the light, while SiGe absorbs light at 1180nm it does not do so at 1550 nm, making the device unusable at the needed frequency. Table 3summarizes the state-of-the-art photonic links that have been demonstrated.

Table 3. Summary of state-of-the-art photonic links.

Author	Chen 2015 [30]	Rakowski 2015 [31]	Yu 2015 [32]	Li 2014 [33]	Liu 2012 [34]	Sun 2016 [35]
RX Data-rate [Gbps]	5	20	24	8	10	10
RX Energy [pJ/bit]	1.73	0.58	0.71	0.28	0.35	0.35
TX Data-rate [Gbps]	5	20	25	5	10	5
TX Energy [pJ/bit]	0.35	1.31	2.47	0.81	0.14	0.03
Technology [nm]	180nm Bulk	130nm SOI	130nm SOI	130nm SOI	130nm SOI	45nm SOI

1.5. Summary

Electrical interconnects cannot keep pace with the progresses of computation and scaling of the transistor. The density of metal layers and their power consumption makes the research community consider alternative methods for implementing off-chip communications. Optical links promise to satisfy the area requirements due to the possibility of deploying WDM. Photonics has also demonstrated that it can create communication at a power consumption suitable for computer requirements.

In Chapter 2 we will evaluate the main metrics in the performance of a modulator and will create extensive MATLAB models for them. A new PN junction architecture will be proposed, that will maximize bandwidth and extinction ratio.

Chapter 3 will be devoted to measuring the devices designed in the second section and adjusting the models with Sentaurus, a Synopsis simulation tool, and actual measurements of the devices.

Chapter 4 will focus on detectors. We will tackle the problem of increasing bandwidth with increasing laser power. We will use Sentaurus to reproduce the experimental results and then identify the source of such behavior. Solutions on how to fix the problem will be proposed. The last chapter will provide a summary of the key findings and make suggestion for future research.

2. Modulators: Interleaved vs T-junctions

In this Chapter we will present an analytical model for spoked ring optical modulators. Building an analytical model of the modulator allowed us to develop a deeper understanding of how an optical modulator works. It also allows us to identify the main assumptions and to evaluate their validity. After the model is built, it allows us to run different optimization to design a better modulator.

The ultimate goal is to develop intuition about tradeoffs in optical modulators using MATLAB simulations. In the next Chapter we will test our MATLAB simulations against Sentaurus, a numerical device physics simulator, and measurements of physical devices.

We will start with a short note on the design of waveguides to allow efficient coupling into the ring. The bulk of the chapter will be dedicated to studying the electrical properties of the modulator. In the end we will briefly discuss how the optical response limits the electrical one.

2.1. The Waveguide

A typical ring is illustrated in Figure 9 [21], and contains metal contacts, to electrically access the PN junction, on the inside of the device. The metal contacts are illustrated in yellow. The PN junctions have to be made long enough to prevent the optical mode from overlapping with the metal junctions, causing significant loss.

One solution is to increase the length of the PN junction, but this is not favorable because it will increase the RC and thus slow down the device. Another solution is to engineer the waveguide that forces the optical mode to be confined tighter. This can be achieved by allowing only the 1st optical mode to couple into the device.

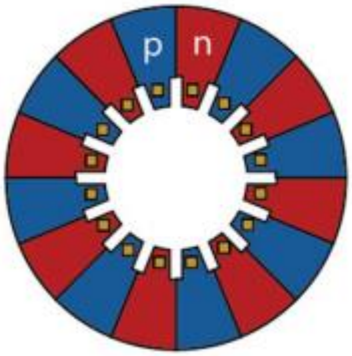

Figure 9. Typical optical ring design, containing metal contacts (yellow) on the inner side of the device.

This was achieved in [8]. By creating a sinusoidal-coupler, it was possible to excite only a single mode in the cavity (Figure 10). The result, is a mode that is confined to the outer side of the ring, avoiding the metal contacts on the metal contacts on the inside of the ring (Figure 11).

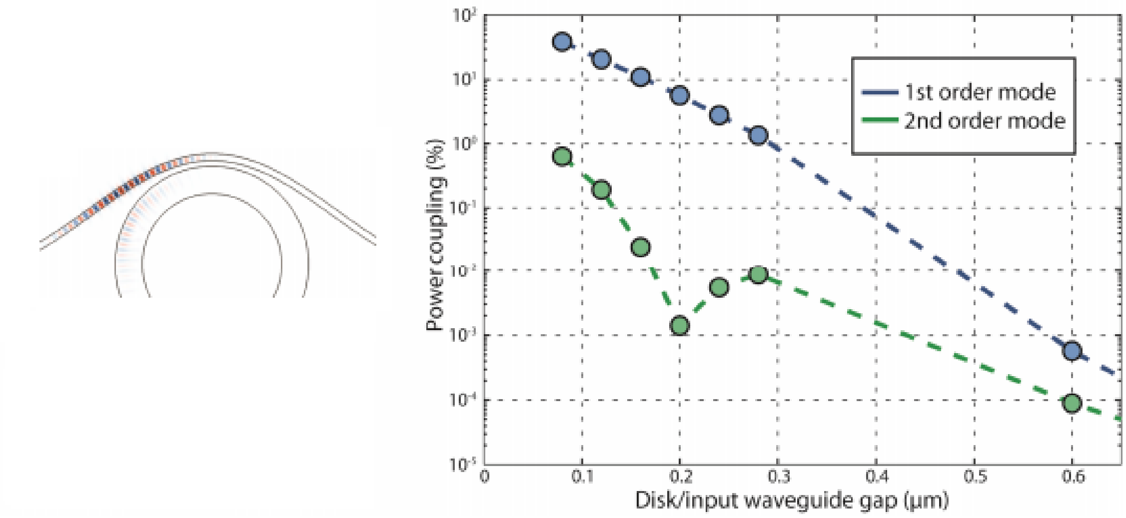

Figure 10. By creating a sine-like waveguide, the 2nd order mode was significantly decoupled from the cavity. The leads to a tighter confined mode in the ring and thus allows for a shorter PN junction and a faster device [22].

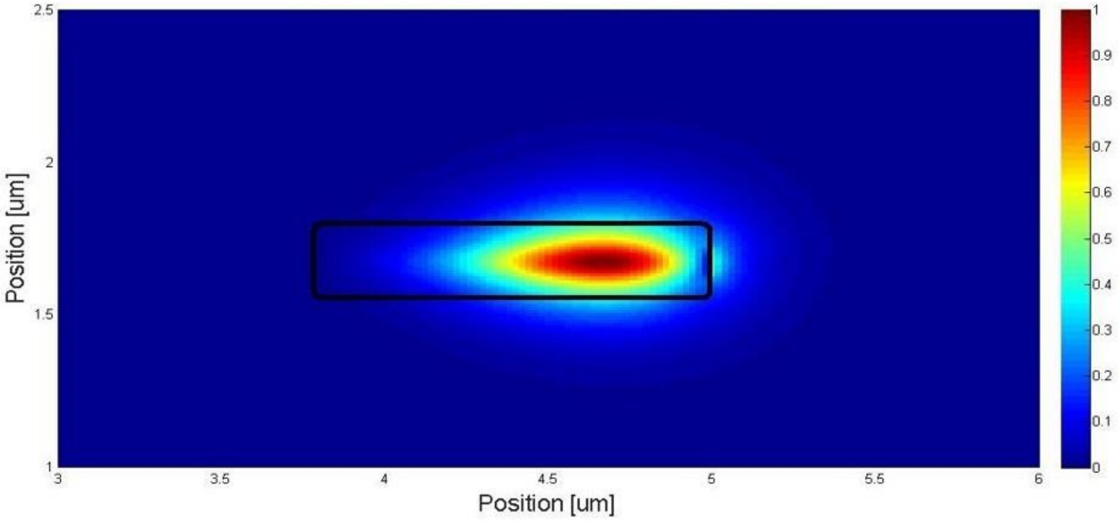

Figure 11. The optical mode shape inside the modulator with a radius of 5μm. The shape of the PN junction is represented by the black rectangle. It is clear that the mode is confined towards the outer part of the ring and is not significant near the metal contacts, thus avoiding loss.

2.2. Electrical Modeling

We will now work towards understanding how charges are supplied to the PN junction. When we change the voltage on the PN junctions we change the widths of the depletion regions, thus increasing or decreasing the depletion region. When the width of the depletion region changes, the number of carriers in the device changes. This affects, through Soref's equations, the refractive index of the ring, causing the resonance to shift.

Throughout this analysis we will examine the modulator reported in [21] and illustrated in Figure 9. The length of the PN junction (outer radius minus inner radius), l, is taken to be 1.75 μm, the average width, w, of a spoke is 0.25 μm, and the thickness, h, is roughly 80 nm. The doping, N_A and N_D of P and N sides, is taken to be $5*10^{17}$ cm^{-3}.

2.2.1. The Parasitic RC

Before concentrating our efforts on optimizing the electrical RC of the modulator we first want to make sure that the parasitic resistance of the metal layers and the capacitance of the metal pads do not limit us in our pursuit of higher bandwidth.

The PDK of the process suggests that a median resistance per micrometer is about $2\ \Omega/\mu m$ and that the average capacitance can be estimated to be $0.1\ fF/\mu m$. With pads of length 60 μm and an approximative length of the metal being 1 μm we can estimate a 3dB frequency:

$$f_{parasitics} = \frac{1}{2\pi RC} = 13000\ GHz;$$

Well above our 15 GHz target. Thus the parasitic capacitances and resistances do not significantly impede us from reaching the needed bandwidth.

2.2.2. Constant Capacitance

Let us first analyze the above mentioned device and try to increase its bandwidth while keeping its capacitance constant. Since the energy consumption is $E = CV^2/2$, the power will stay constant. So we are trying to increase the bandwidth, while keeping the energy per bit constant.

Since we are operating mostly in reverse bias, the junction capacitance is the dominating capacitance:

$$C = A * \sqrt{\frac{q\varepsilon_s}{2(\varphi_{in} - V)} * \frac{N_A N_D}{N_A + N_D}};$$

Where, A is the area of the junction (in our case $A = hl$), q is the elementary charge, ε_s is the electrical permittivity of the silicon, φ_{in} is the built in potential of the junction, and V is the bias voltage (we will take it to be -1V). As $\varphi_{in} = 60\ mV * \log_{10}(\frac{N_A N_D}{n_i^2})$, with $n_i = 1 * 10^{10} cm^{-3}$, is weakly dependent on doping, it is usually assumed to have an average value for the respective doping range. We will also conveniently define $K = N_A N_D/(N_A + N_D)$, since we will be optimizing over doping. As of now we will use the lumped RC model to estimate the 3dB frequency at which the junction can operate.

Figure 12 illustrates constant K and thus constant capacitance curves in the N_A and N_D space. The graph is symmetric, as expected, around the f(x) = x . It also exhibits the characteristic that at high N_D, N_A is constant, since K converges to N_A, the converse is also true. Anywhere on the curves illustrated in Figure 12, the energy consumption is constant. Our goal is to choose an operating point that will increase our 3dB frequency.

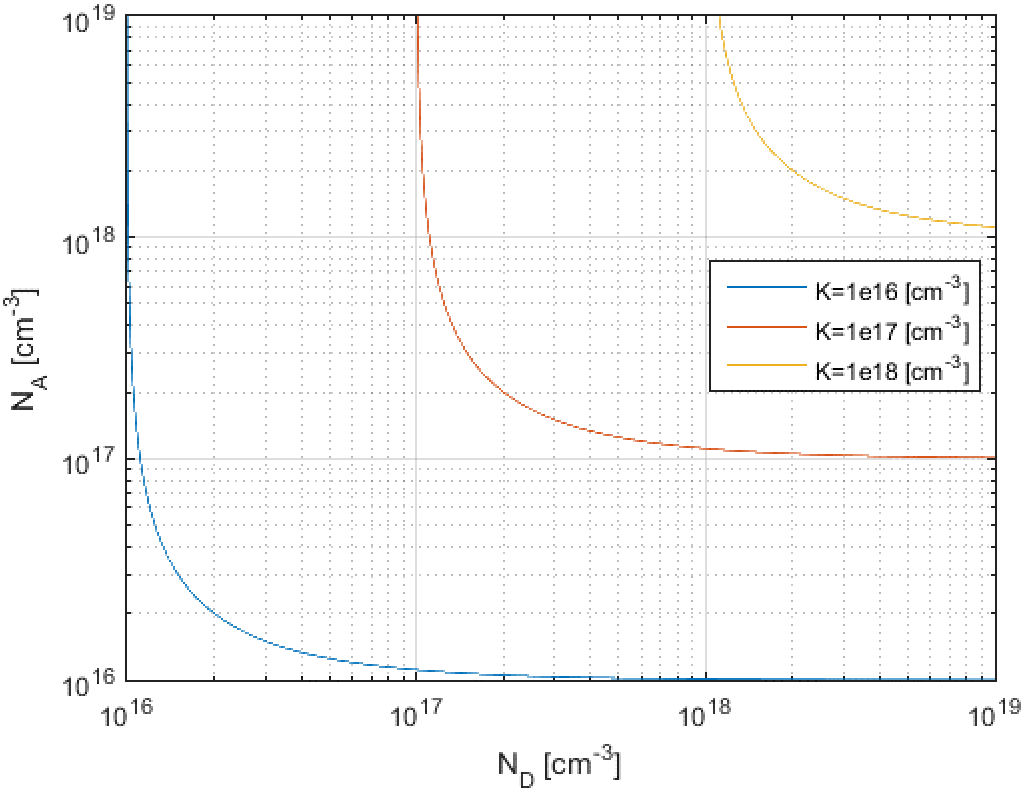

Figure 12. Constant capacitance curves in the N_A and N_D space for different values of capacitance.

Since C is kept constant, the only thing to optimize in the RC product is R. Figure 13 illustrates the resistivity of holes and electrons. We can observe that at high doping, the resistivity of holes and electrons are almost equal. However when the doping is small electrons will provide us with a much smaller resistivity. If we go back to Figure 12, we can again observe that, the two extreme scenarios are high N_D and low N_A or the other way around. From the observations presented by Figure 13, we can conclude that a faster device will be achieved for low N_D and thus high N_A.

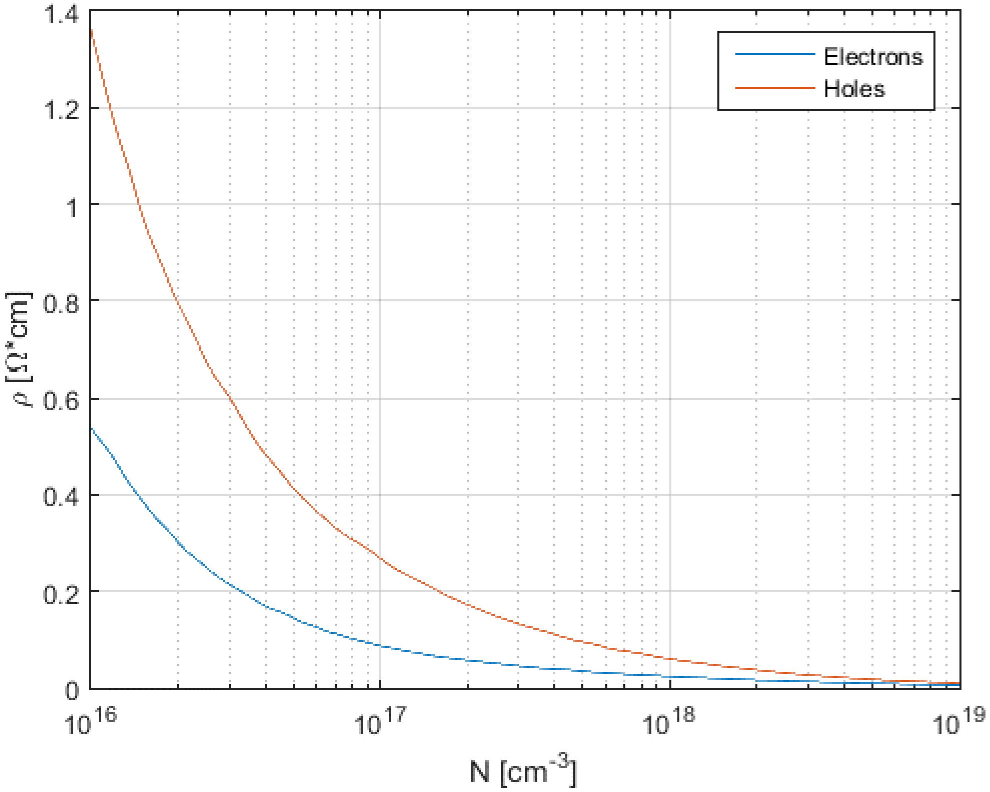

Figure 13. Resistivity of Electrons and Holes. We can observe that for high N, the resistivity is the same for both Electrons and Holes. However at low doping, Electron's resistivity is much smaller thus suggesting that picking a higher N_A will increase the bandwidth of the device, on a constant K curve [36].

The above mentioned finding can be graphically observed in Figure 14. We can see that the frequency at low N_D and high N_A is much higher than the one for high N_A and low N_D. As already mentioned, this is due to same resistivity at high doping and a significantly lower resistivity for electrons, for lower doping (Figure 13). Going from equal doping for the P and N sides will roughly increase the bandwidth of the modulator by a factor of 2X, while keeping the power constant.

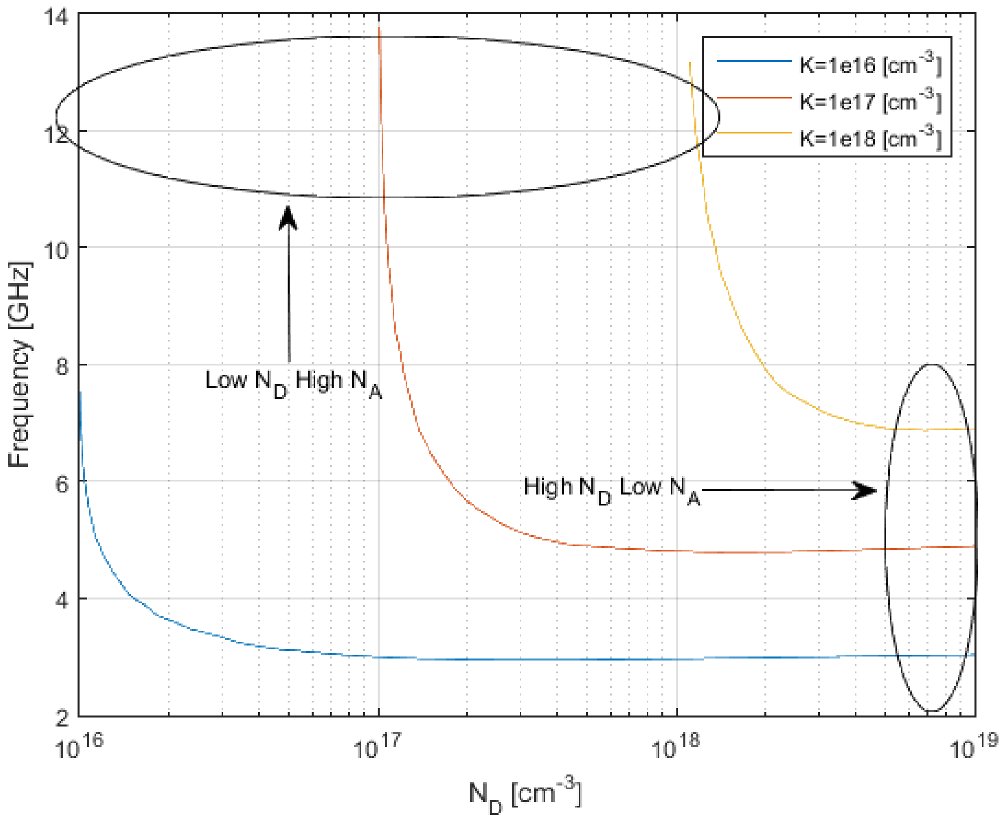

Figure 14. Frequency versus N_D plots, for constant K. As expected, we observe a higher frequency for low N_D and high N_A, due to different resistivity at small doping, illustrated in Figure 13.

However, the downside of increasing the doping is that the absorption, according to Soref's equations [13], will increase by:

$$\Delta\alpha = 3.5 * 10^{-18} * \Delta N_e + 2 * 10^{-18} * \Delta N_h;$$

Thus going from both spokes being doped at 10^{17} to 10^{18} for P and 10^{16} for N will cause an increase in absorption from roughly 1.55 cm^{-1} to 3 cm^{-1}, this will thus change Q and affect the ER.

$$Q = \frac{\lambda_0}{2\delta\lambda};$$

Where λ_0 is the resonance wavelength and $2\delta\lambda$ is the full width at half maximum (FWHM) for the transmission as a function of wavelength, which is described by a Lorentzian with $x_0 = \lambda_0$ and $\gamma = \delta\lambda$. Using Soref's equation for the refractive index we can estimate that modifying the doping, as described above, at $\lambda_0 = 1150\ nm$ will cause a shift in resonant wavelength by roughly 0.25 nm. The overall Q will thus decrease by a factor of 2, due to change in absorption. For a Lorentzian it can be shown that the peak derivative (thus the biggest ER) can be achieved for $|x - x_0| = \frac{\gamma}{\sqrt{3}}$ and that $ER\ \propto \frac{1}{\gamma^2}$. Thus changing only the doping of the ring will decrease ER by a factor of 4, which is very detrimental for an ER of 5-6 dB. Care should be taken to hold Q relatively constant, either operating at different wavelengths or by under coupling or over coupling the ring.

2.2.3. Distributed RC

Let us now examine the performance of the device while considering a distributed instead of a lumped RC model, as in the previous section. If we treat the PN junction as a very long ladder of RC, instead of just one big RC circuit, it is intuitively clear that the voltage will take some time to propagate through the junction. Thus the end of the junction will experience a different RC limit than the beginning.

According to [37], the distributed RC's transient is governed by the following equation, for t << RC:

$$V(t) = 2erfc\left(\sqrt{\frac{RC}{4t}}\right);$$

and for t >> RC:

$$1 - 1.366 * \exp\left(-\frac{2.5359t}{RC}\right) + 0.366 * \exp\left(-\frac{9.4641t}{RC}\right);$$

A detailed derivation can be found in [38] and is a Taylor expansion, for t << RC and t >> RC, of the Fourier response of the distributed RC ladder, given by:

$$V(s) = \frac{1}{s\ cosh\sqrt{sRC}};$$

The resulting voltage lag can be observed in Figure 15. As we get further and further away from the metal terminals, the voltage takes longer and longer to reach the junction. This has implication for the PN junction, since the bandwidth of the junction itself is not as important as the bandwidth that the optical mode is observing.

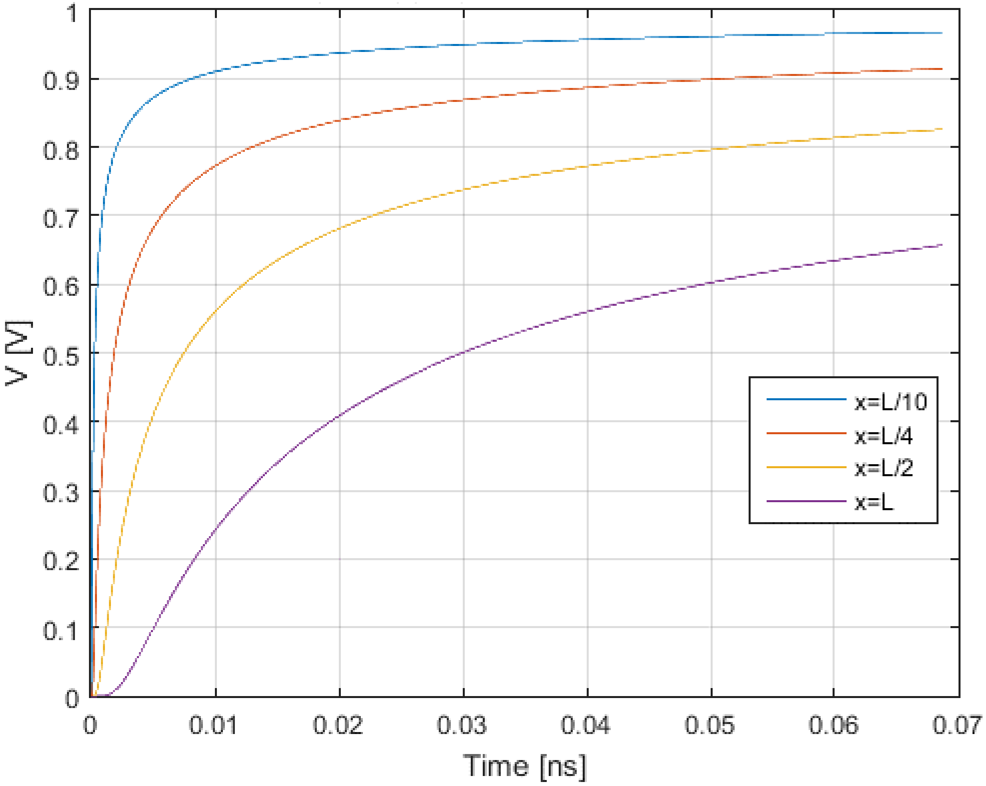

Figure 15. Voltage lag due to a distributed RC ladder. The further away from the metal contacts the higher is the voltage lag.

From Figure 11, we can observe that the mode is concentrated at the outer side of PN junction, thus it will experience a slower bandwidth than the pure electrical junction. For l = 1.75 μm the mode is concentrated roughly between 1.2 and 1.75 μm. Figure 16 illustrates the evolution of the "local frequency" as we get away from the metal contacts. Unsurprisingly, the lumped RC model yields the frequency experienced roughly in the middle of the PN junction. The optical mode however, observes a much smaller frequency compared to the lumped RC model.

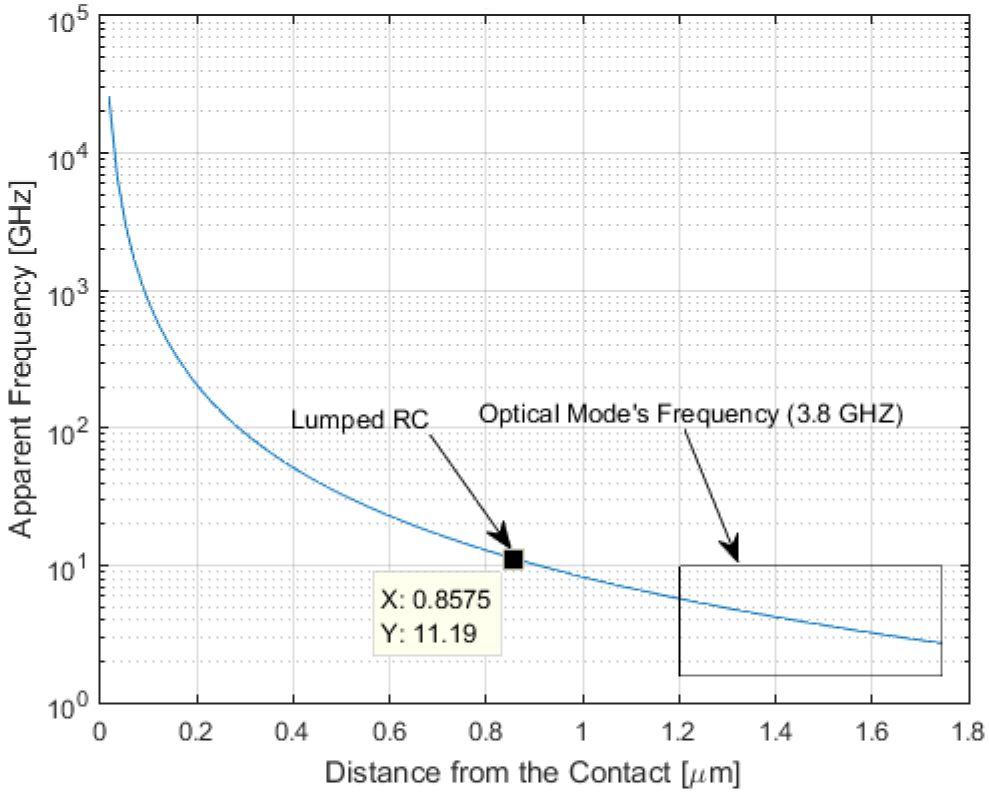

Figure 16. Frequency dependence on the position in the PN junction, at 1V reverse bias. Unsurprisingly the Lumped RC model yields the average RC frequency. The optical mode observes a much smaller frequency compared to the lumped RC.

Another final remark should be made regarding the bias. Since $C \propto 1/\sqrt{\varphi_{in} - V}$ we expect the frequency to go up with increased V, since the RC will go down.

Figure 17 illustrates this dependence, with a rough dependence of $1/\sqrt{V}$, as expected from the formula for C.

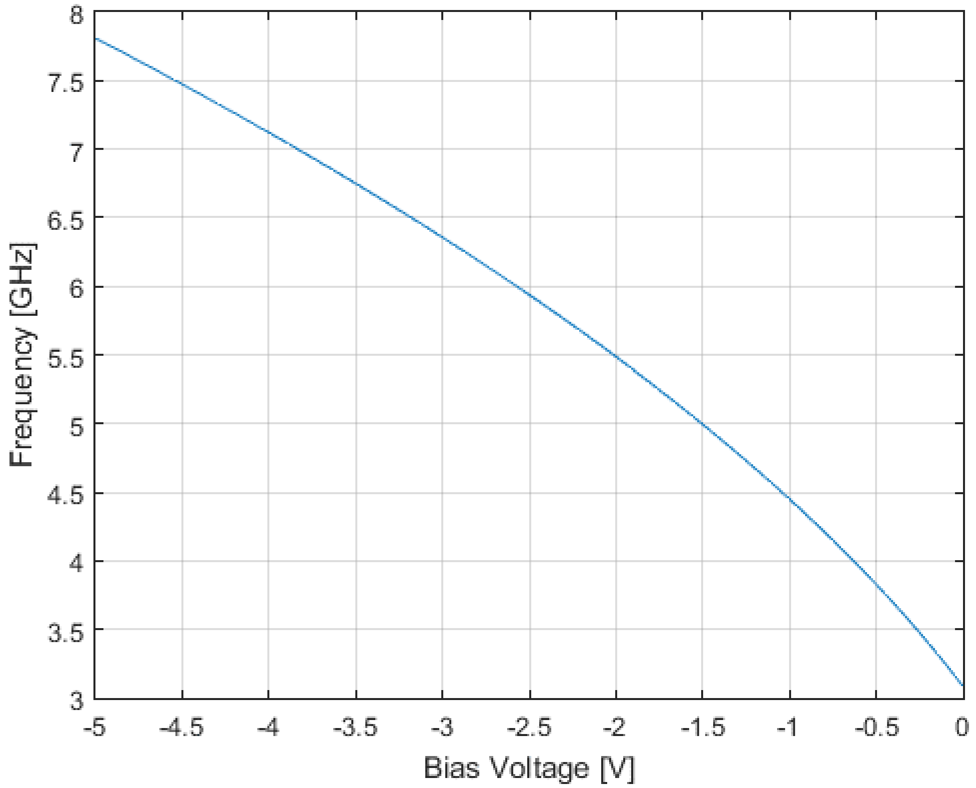

Figure 17. The dependence on the "optical frequency" on the bias voltage, for a doping of 5*10^{17} for P and N. A roughly 1/ $\sqrt{V}$ dependency is observed, as expected from the C dependence on the bias voltage.

2.2.4. The T-junction

From the previous section we can observe that we can categorize the capacitances in our PN junction as "modulating capacitance" and "parasitic capacitance" (Figure 18). The "modulating capacitance" is the capacitance seen by the optical mode and the capacitance that actually generates charges that will influence the ER. The "parasitic capacitance" is useless for optical purposes, slowing down the device and consuming power. The T-junction, is a junction elaborated to minimize the “parasitic capacitance” and maximize the optical one.

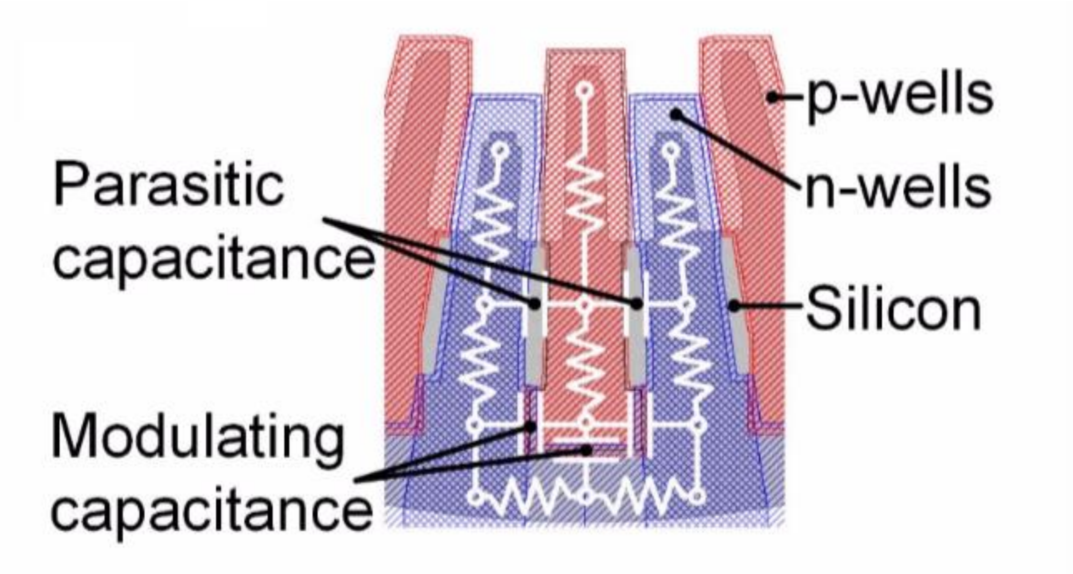

Figure 18. Structure of a T-junction. The capacitance located where the optical mode is travelling is considered "Modulating Capacitance" and is maximized. The capacitance closer to the metal contacts is the "Parasitic Capacitance" since it does not contribute to the ER and only slows down the device and consumes power. Parasitic capacitance is minimized by inserting an intrinsic region between the P and N junctions.

The T-Junction is presented in Figure 18. The capacitance located closer to the metal contacts is the parasitic capacitance, it is minimized by introducing intrinsic silicon in between the P and N spokes. The modulating capacitance is located in the zone where the optical mode is concentrated. The N region also goes over the P spoke in order to create and additional capacitance right in the center of the optical mode.

To determine the 3dB frequency of the T-Junction, we are using the open-circuit time constant. It is a technique, used to approximate the 3dB frequency of complex electrical circuits. Each capacitor, at its turn, is replaced by a short while all the other capacitances are replaced with opens. The overall resistance seen by that capacitor is computed and the corresponding time constants is $\tau_i = R_{eq}C_{i\_short}$. This is repeated for all the capacitors and the time constants are then summed up to determine the 3dB frequency, $f_{3dB} = \frac{1}{2\pi\sum\tau_i}$. The resistance of a segment is calculated as $R = \frac{\rho l}{h*(w-2w_d)}$ where ρ is the resistivity, l is the length of the segment, h is the thickness, w is the width, and w_d is the width of the depletion region. The factor of 2 next to w_d accounts for the fact that each junction is depleted from both sides, since the PN junctions are positioned in a ring. The capacitances is calculated as in 2.2.2.

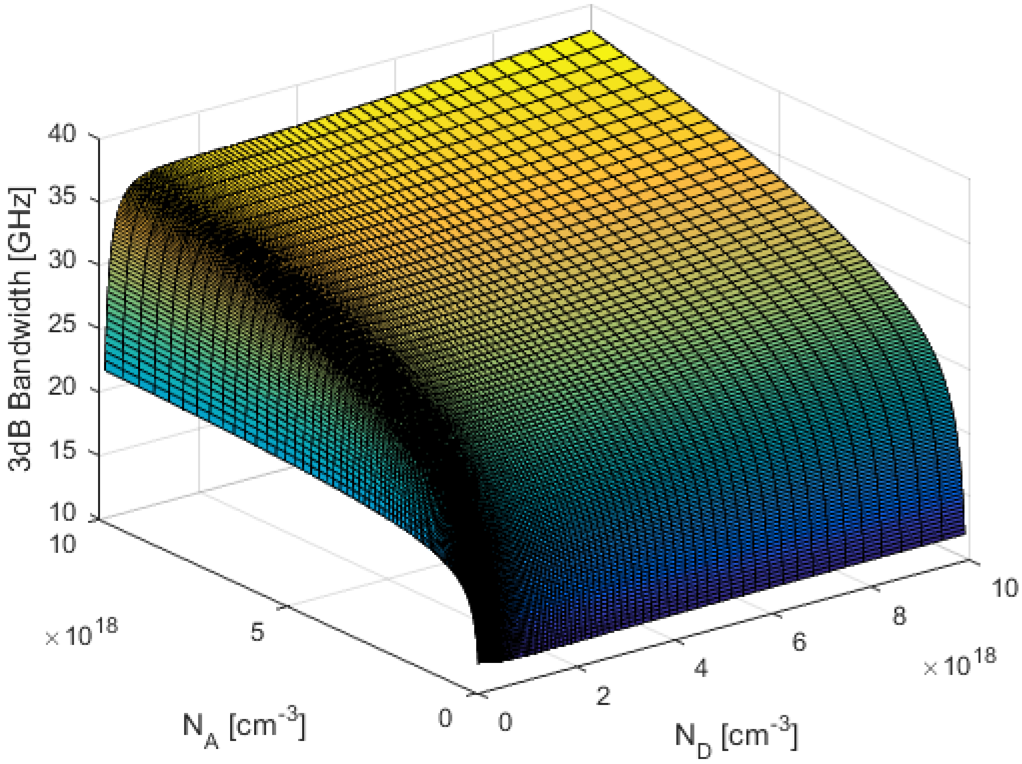

Figure 19. Frequency of the T-Junction as a function of N_D and N_A, at 1V reverse bias. The maximum predicted frequency for the T-Junction is 38.0 GHz for N_A=N_D=10^{19}cm^{-3}.

Figure 19 shows the 3dB frequency of the T-Junction as a function of doping of the P and N spokes. We can again observe the predicted effect of higher frequency for high N doping than for high P doping. The maximum achievable frequency 38.0 GHz, which is far beyond the target 15GHz.

Figure 20 demonstrates the bias dependence of the 3dB frequency for the T-Junction. We can observe that it is much faster than the regular PN junction from Figure 16 (the doping was kept the same).

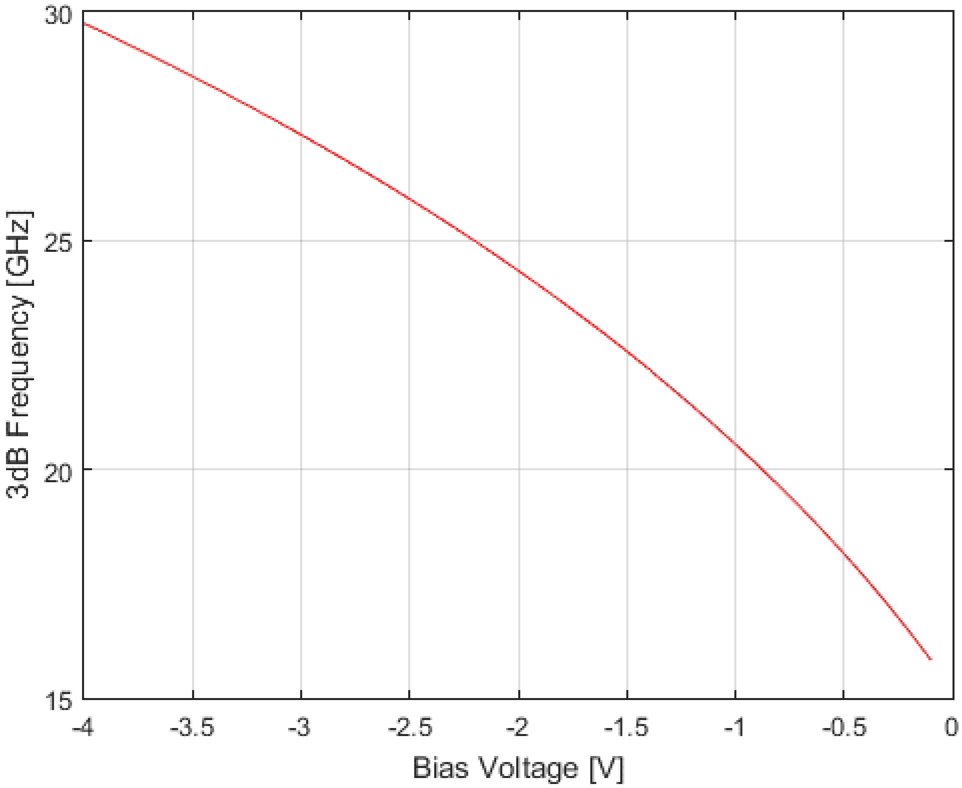

Figure 20. 3dB frequency of the T-Junction at N and P doping of $5*10^{17}cm^{-3}$ for an apple to apple comparison to the interleaved PN junction (Figure 17). We can see that the T-Junction is much faster in the same conditions as the interleaved junction.

2.2.5. The Optical Limitations

The simulations above examine the modulator from an electrical point of view. Now let us determine what is the speed of the response of the ring to electromagnetic perturbations and if it limits our electrical bandwidth. The quality factor of the ring, Q, can be defined in the following way:

$$Q = 2\pi * \frac{Energy\ Stored}{Energy\ Dissipated\ per\ Cycle} = \frac{2\pi f_r W}{P};$$

Where f_r is the frequency of the radiation – around 250 THz for a typical 1200 nm wavelength. W is the energy stored in the ring, and P is the power loss. We can conclude that, the field E is:

$$E(t) = E_0 * \exp\left(-\frac{t}{\tau}\right);$$

With τ:

$$\tau = \frac{Q}{2\pi f_r};$$

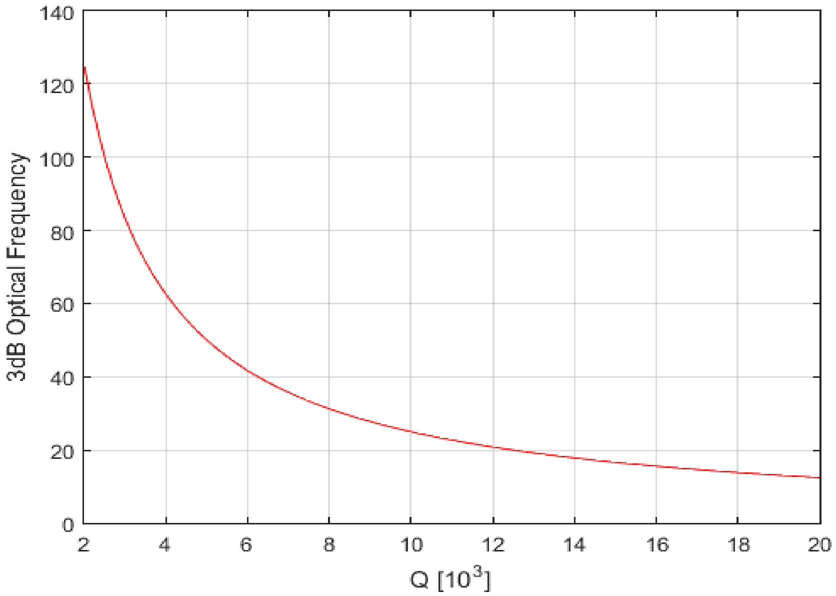

Figure 21. Optical 3dB frequency as a function of Q at 1200nm. We can see that for Q higher than 15,000 the optical bandwidth can start limiting the electrical performance.

Figure 21 illustrates the dependence of the 3dB optical frequency on Q, with the 3dB frequency defined as $f = \frac{1}{2\pi\tau}$. We can see that if Q exceeds 15,000 the 3dB optical frequency falls below 17 GHz thus potentially limiting the electrical performance of the PN diode, which aims for 15 GHz. Thus care should be taken not to engineer a ring with Q much higher than 15,000.

In the same time, we cannot afford a too low of a Q, since low Q is associated with high loss. If we desire a 1dB insertion loss, then:

$$10\log_{10}\left(\frac{P}{P_0}\right) = -1 = 10\log_{10}(\exp(-\alpha l));$$

Where α is the loss of the ring and $l = 2\pi R_{ring} = 31.4\ \mu m$ for a $5\ \mu m$ ring. In the same time:

$$\alpha = \frac{2\pi n_g}{Q_{int}\lambda_0};$$

With $n_g = 3.5$, being the group index of refraction in silicon, $\lambda_0 = 1200\ nm$, the wavelength of the operation and Q_{int}, being the intrinsic Q of the ring, which at critical coupling becomes:

$$Q_{int} = 2Q;$$

Thus we estimate that we need a Q above 1,250 to fulfill the 1dB insertion loss requirement.

In conclusion, to operate at 15 GHz with 1dB insertion loss or lower, we need a Q above 1,250 and below 15,000. If, however, we want to consider operating at 50 GHz, the maximum theoretical limit of the T-junction, we will need a Q above 1,250 and below 5,000 which is a much tighter interval and therefore requires careful engineering of the Q.

2.3. Conclusions

In this Chapter we presented MATLAB simulations of the existing CMOS compatible junctions (the PN interleaved junction). We identified a problem –the frequency that is observed by the optical mode is not the same as the electrical frequency. We also realized that not all the capacitance is “useful” and that the parasitic capacitance only slows down the device, and consumes power without contributing to the ER. We further proposed a new design, the T-Junction, that alleviates this issue by concentrating the capacitance in the optical region and that minimized the parasitic capacitance. MATLAB simulations have proven the T-Junctions to be significantly faster than the interleaved PN junctions.

In Chapter 3 we will measure actual devices that were fabricated and will also contra pose the MATLAB simulations against Sentaurus simulations and experimental measurements, to ensure the accuracy of our models and findings.

3. Modulators: Experimental Results, Simulation, and Optimization

Once the T-Junction devices have been fabricated we had the chance to check our models against the experimental data. In this Chapter we will present experimental results from a recently fabricated device. We will also compare the results generated by a MATLAB model to the results of the simulations and experiments. We will make sure that the MATLAB model and the simulations can accurately predict the behavior of the fabricated devices. In the final part of this chapter we will propose a design of a faster modulator, based on the simulations and theoretical predictions.

3.1. The Sentaurus Model

Sentaurus is a device physics simulator that allows the user to define the shapes, doping, and meshes of the device. The simulator also allows the user to run transient, quasi-stationary, small signals and optical simulations. Sentaurus solves the electron and hole continuity equations and the Poisson equations to determine a set of physical parameters characterizing the device. The set can include parameters such as Fermi levels, electrical fields, space charge, etc. Plenty of documentation can be found in the Sentaurus manuals [39]. There are also plenty of simulation examples in the manuals and archives that come with Sentaurus. It is useful to start with the most basic simulations that analyze the device in steady state, and then work your way towards more complex simulations. The easiest way to start with Sentaurus is to pick a simulation example that is similar to what you want to do (for example a small signal simulation) and then modify the code accordingly. The manuals contain a significant amount of simulation code explained step by step, so modifying the code will not be particularly complicated. Once you have modified the code, you should devise tests to check that the new code does what you expect it to do. For example, if the code was modified to include an optical beam in a particular region, you should plot the Beam Generation in the needed regions and check if all the parameters of the beam are what you expect them to be. Sentaurus contains a fair amount of silent default values that can lead to unexpected results. For example, the Beam Generation's spatial decay is defaulted to a Gaussian decay, thus carriers may be generated in unwanted regions (Figure 22). Sentaurus is an incredibly powerful tool but it will take some time for a new user to figure how things work exactly, you just have to grind through it.

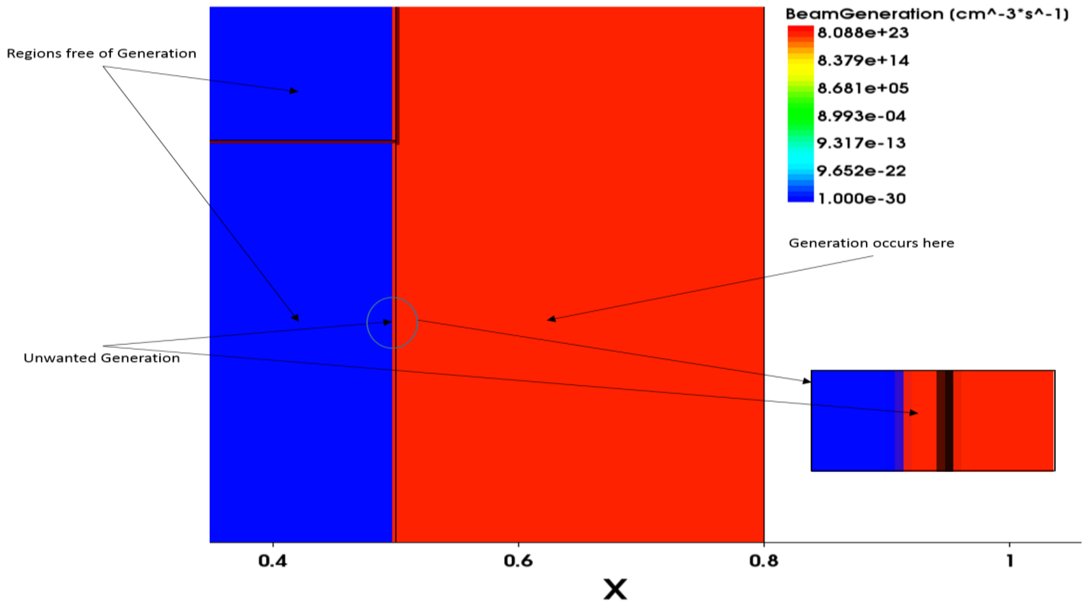

Figure 22. Generation was designed to happen in the rightmost region only. However due to default Gaussian spatial decay, there are carriers generated outside the required region.

3.1.1. Simulating the Modulators

We made use of the periodic structure of the PN ring and only simulated one PN junction instead of the whole ring. Simulating only one PN junction significantly reduces simulation time. The PN junction is presented in Figure 23 a), with the P region in blue, N region in red and the intrinsic region in green. The metal contacts are in grey with a pink outline, they are located on the left of the PN junctions. The periodic boundary conditions are imposed on the top and bottom of the junctions illustrated. The characteristic T shaped junction is traced by the boundaries of the P region. Initially we tried to simulate a full P junction and then a full N junction, next to it. Upon checking the log files it was discovered that this posed convergence problems. The periodic boundary conditions were imposed in the depletion regions thus complicating the physics. Picking a periodic structure (as in Figure 23 a)) with one half N region, a full P region and one more half N region allows us to impose periodic boundary conditions in the middle of the N region, thus avoiding the depletion regions and the complicated physics. This solved the convergence problems.

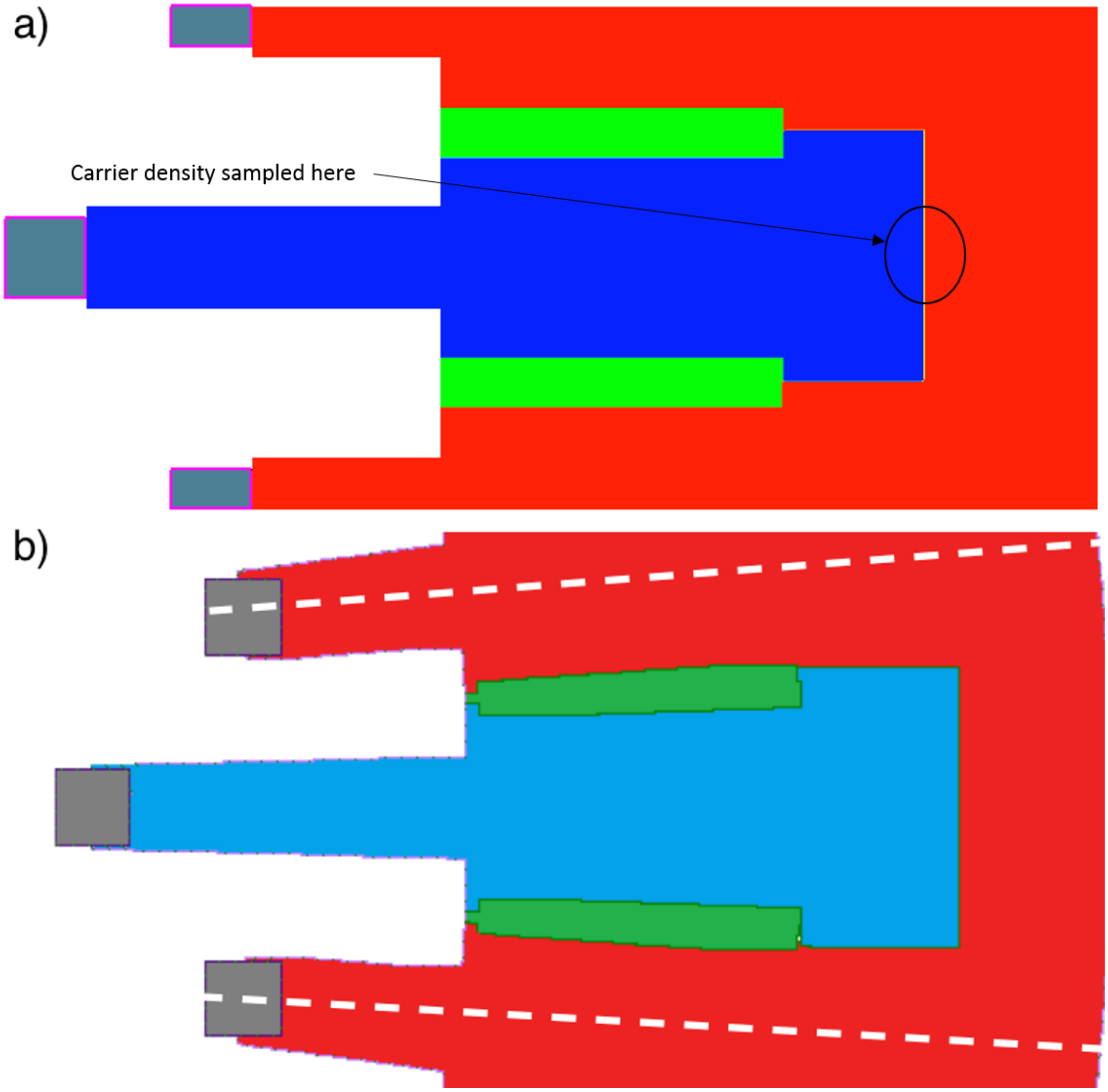

Figure 23. One PN junction. a) The simulated PN junction. The P region is in blue, the N region is in red and the intrinsic region is in green (the doping is on the order of 10^{17} cm^{-3}). The metal contacts are in grey and are outlined in pink. Periodic boundary conditions are imposed on the top and on the bottom of the presented PN junction. We can observe the characteristic T-shape traced by the boundaries of the P junction. To determine the 3dB frequency the carrier densities were sampled at the top of the T-junction. b) Snapshot of the ring from the GDS file. The color scheme is consistent with a). The white dotted lines represent the periodic boundary conditions. We can see that the width of the junction is varying as we approach the outer radius.

We have made the approximation of a rectangular shaped junction instead of a cone like shape that is formed by the real ring (Figure 23 b)) because Sentaurus does not allow users to define cone like shapes. To account for the varying width of the junctions, the Sentaurus simulation used the average value of the widths found in the GDS.

To determine the 3dB response of the PN junction a small signal step was applied to the bias of the junction and the variation of the hole density (monitoring electrons yielded similar results) was monitored in the top part of the spoke (the top of the “T”). The FFT of this data was taken to determine the 3dB frequency (Figure 24). The reason why the current was not monitored is because, as mentioned, in 2.2.3 this will yield an overestimation of the 3dB response as we only care about what happens in the regions where the optical mode is concentrated.

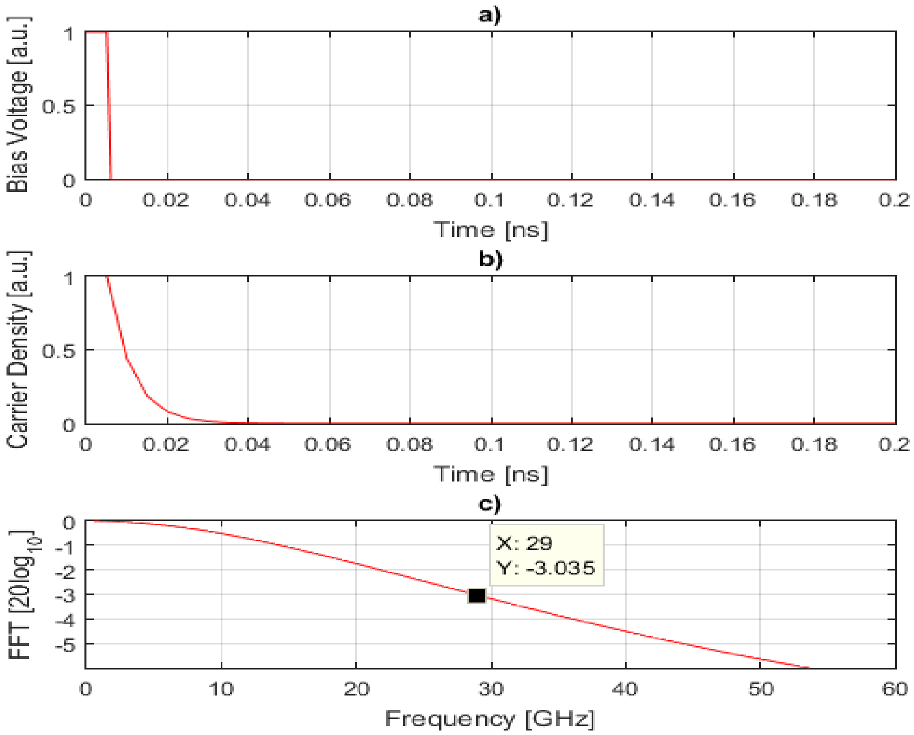

Figure 24. Determining the 3dB frequency from Sentaurus simulations. Figure a) illustrates the time dependency of the Bias Voltage. b) depicts the time variation of the carrier density. Figure c) is the FFT of figure b) and suggests a 3dB frequency of 29 GHz, in this case.

3.2. The Experimental Setup

In order for our simulations to be significant, we have to confirm their results through experiment. The device's layout and a microscope image of the device are presented in Figure 25 and were laid out by Luca Alloatti. Figure 25 a) represents a microscope picture of the chip and illustrates the grating couplers (GC) that allows the light to couple into the waveguide. The signal (S) and ground (G) pads are placed perpendicularly to the modulator and allow for an electrical contact to be made so that the device is biased at the needed voltage. Figure 25 b) illustrates a GDS snapshot of the device. Every quadrant has different masks highlighted. The top right quadrant has the metal, the P and the N masks shown. The metal contacts are placed inside the ring in order to overlap as little as possible with the optical mode, thus avoiding excessive loss. The top left quadrant illustrates the P wells. The bottom left quadrant highlights the N wells and the bottom right quadrant shows us the silicon ring, without any masks present.

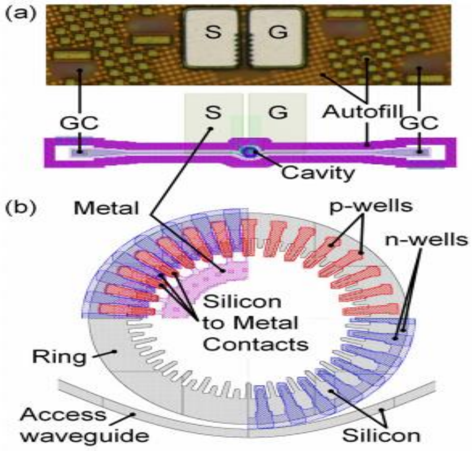

Figure 25. The measured modulator. a) A microscope picture of the chip. The grating couplers (GC) allow the light to couple into the waveguide. The signal (S) and the ground (G) pads are placed perpendicularly to the device and allow landing a probe to supply the needed bias voltage. b) A

snapshot of the GDS representing the modulator. Every quadrant has different masks highlighted/ hidden [23].

The experimental set up used to measure the bandwidth of the modulators is illustrated in Figure 26. The source is a QD Laser (Model QLD1161-8030) controlled by a Laser Diode Controller (LDC) from ILX LightWave (Model LDC-3714). The weak arm of the 10dB coupler is connected to the Bristol Wavelength Meter (Model 621). The bias on the modulator is set up using a 50Ω GS Probe and a Keysight Precision Power Unit (Model B2902A). The optical amplifier used is an Innolume SOA (Model 1170-20-PM-24dB), the temperature and current through which was controlled via a Newport LDC (Model 6000). The Koshin Kogaku adjustable filter (Model FC-1200B-1-1) was at the output of the amplifier, providing a better SNR. The photodetector used was a Discovery Semiconductors (Model DSC 2010) biased at 3V reverse bias by a Hewlett Packard (HP) DC Power Supply (Model E3633A). The Vector Network Analyzer (VNA) was an HP Network Analyzer (Model 8722D).

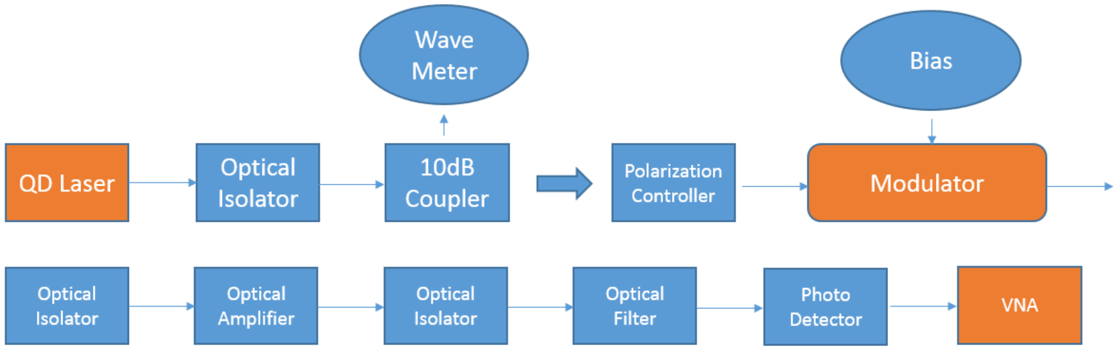

Figure 26. The experimental setup to measure the bandwidth of the modulator.

To obtain good measurements of the 3dB frequency it is recommended to start with simply finding the resonance of the modulator (Figure 27). Further, the power into the modulator should be maximized, if the power into the device is not high enough, the noise generated by the optical amplifier will make the modulation signal undetectable by the VNA. Once we have a detectable signal at the VNA, the wavelength should be further fine-tuned to provide the maximum signal, this usually happens around -3dB in reference to the off-resonance signal.

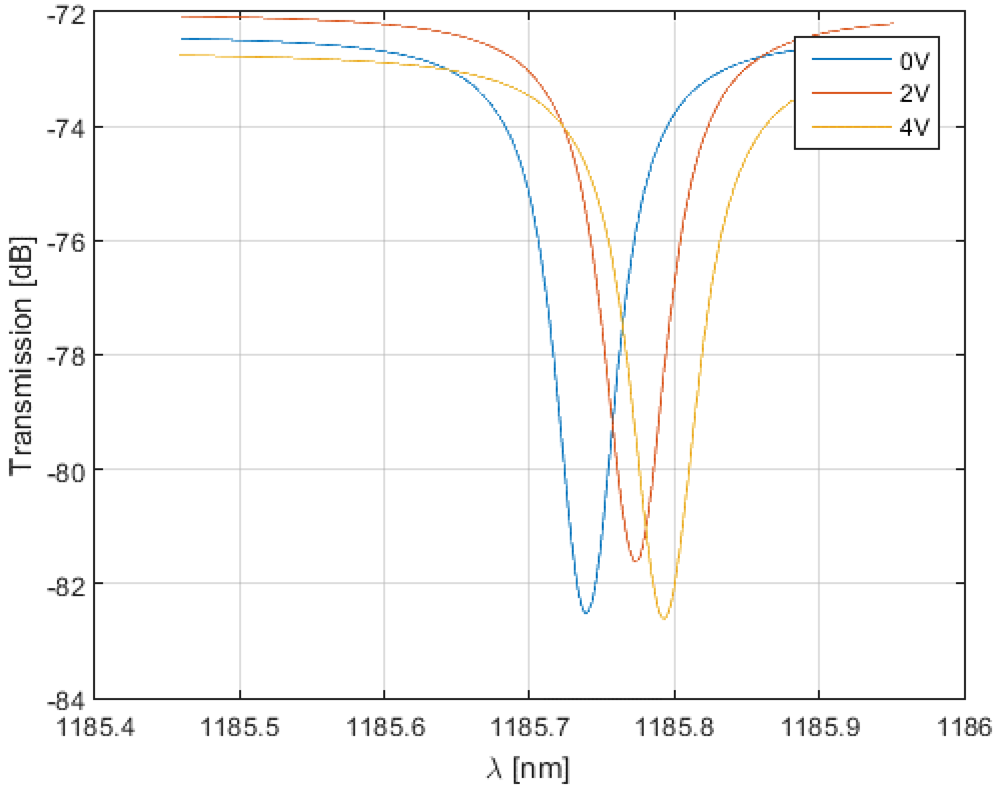

Figure 27. Resonance at 0V, 2V, and 4V reverse bias.

As advised, the VNA and the Keysight Power Precision Unit were turned on roughly one hour before the measurement would start. The signal at the VNA was then maximized by changing the wavelength and the data was recorded. To determine the 3dB frequency of the modulator, the detector's response (provided in the datasheet) and the response of the RF cables (recorded after taking the measurements) were subtracted (in dB scale) from the VNA's data before the 3dB was computed (Figure 28).

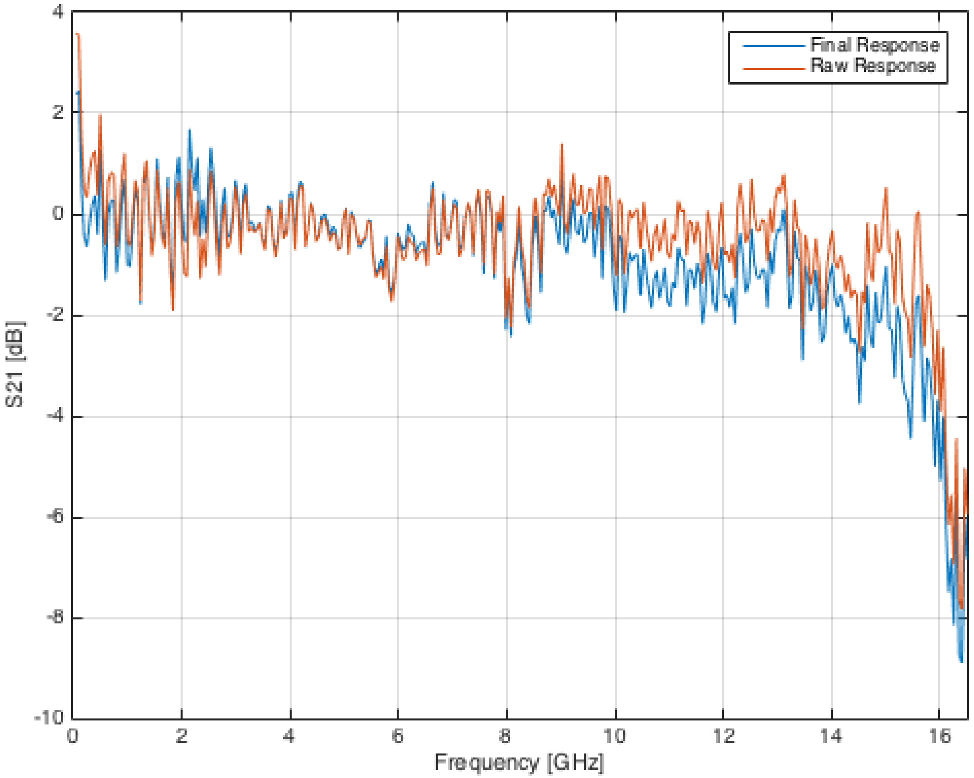

Figure 28. The raw modulator response presents the data measured from the VNA. In order to determine the 3dB frequency we need to subtract the RF wires' response and the detector's response. The final response is the response of the modulator itself and can provide us with accurate 3dB frequency estimates. The 3dB was determined using the MATLAB "power2" fit which fits to an equation of the form $ax^b + c$. "power2" fit was chosen because it was showing the best R^2.

3.3. Results and Discussions

The measurement results of the 3dB bandwidth versus voltage bias, of the fastest modulator are shown in Figure 29. After the experimental results were available, the doping was used as a fitting parameter, the Sentaurus simulations were further run with the same doping as the MATLAB model. We can see good agreement between the experiment, the theory (MATLAB) and the simulations, for low bias voltages.

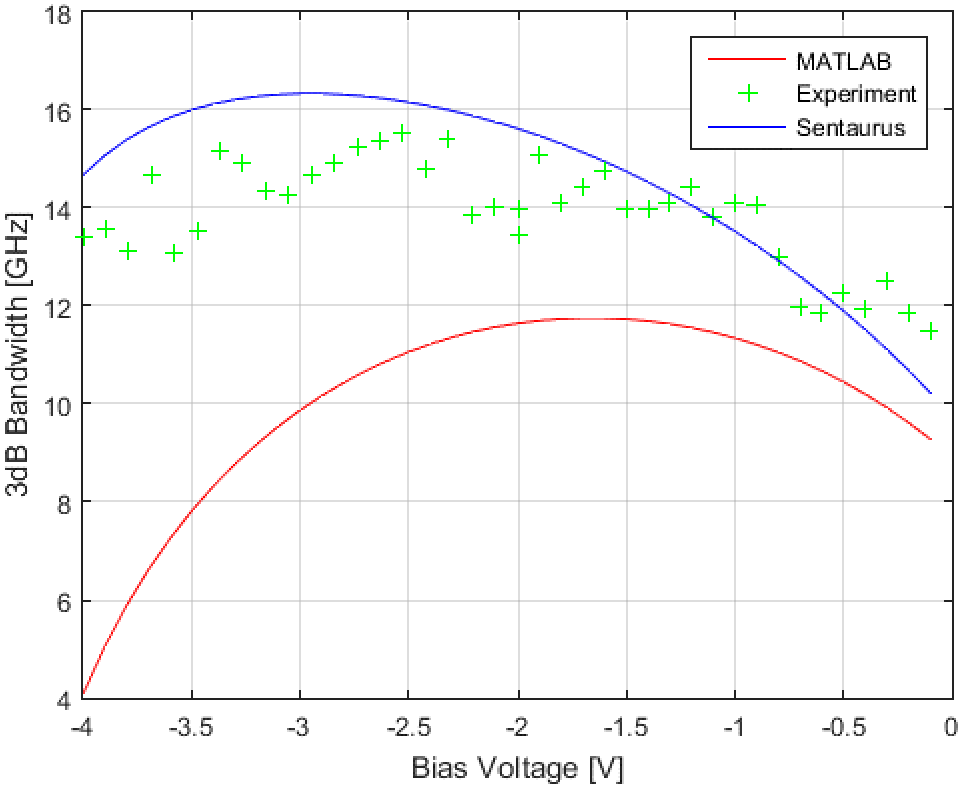

Figure 29. The results of the experiment. The doping was used as a fitting parameter to adjust the MATLAB model, the Sentaurus simulations were run with the same doping as the MATLAB model. The optimal voltage for operation is around -2.6V.

We can see that there is bigger discrepancy between the MATLAB model and the Sentaurus simulations at higher voltages. This is due to the fact that the depletion geometry becomes a 2D problem as the reverse bias voltage increases. The 2D effects are especially prominent at the tip of the P junction (Figure 30) where the junction is depleted from the sides as well as from the bottom. Because the side depletion region is overlapping with the bottom depletion region, this becomes a 2D problem. We were not able to come up with an analytic 2D model for the depletion regions. However for a specific aspect ratio of the junctions, we can account for the 2D model and correct the depletion regions (Figure 31) using the widths of the depletion regions computed by Sentaurus.

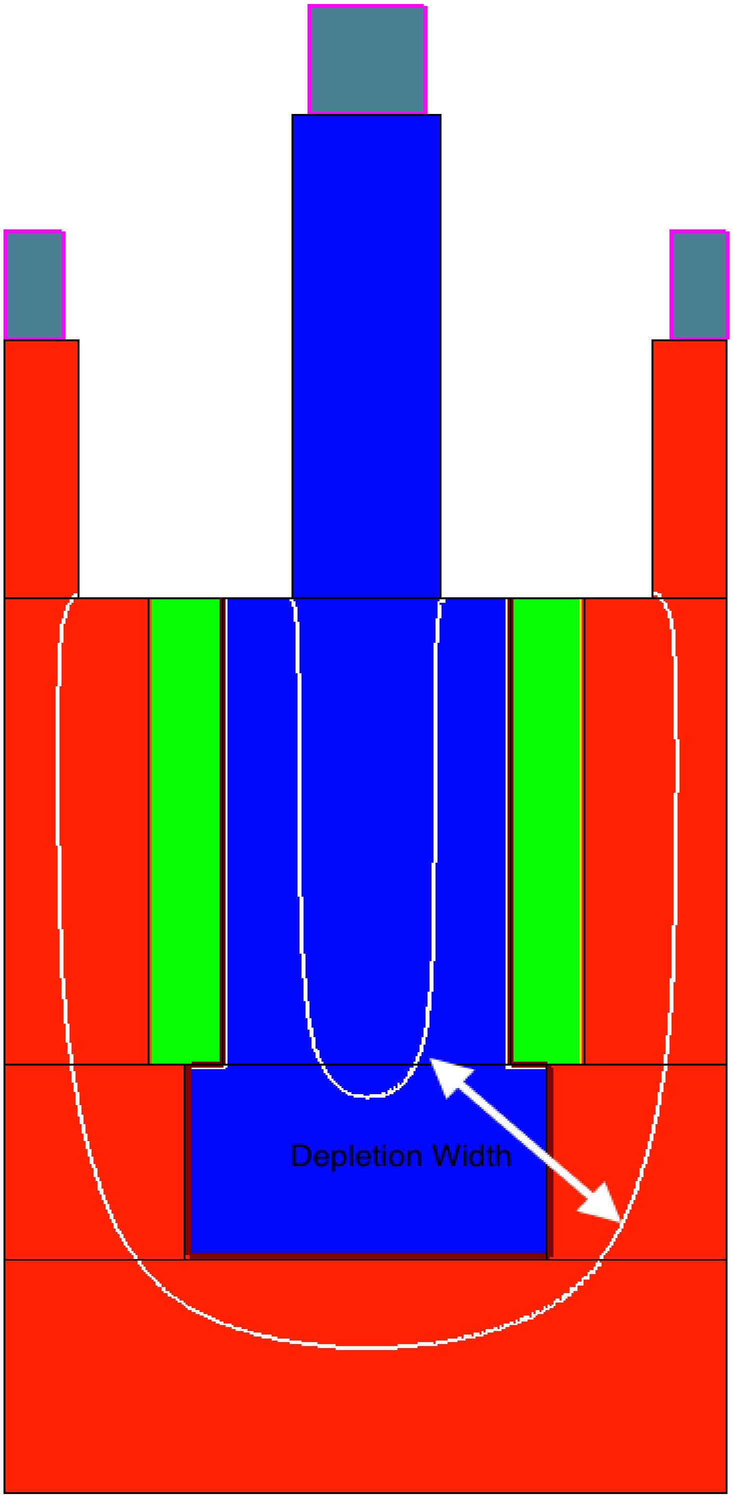

Figure 30. The PN junction at a bias of -3V. The colors are consistent with Figure 23, the white contour illustrates the depletion regions. Even if the P region is doped higher than the N region we can see that at the tip of the T-junction the depletion region is bigger on the P side. This is due to the fact that the tip of the T-junction is depleted from the bottom as well as from the sides making the approximation of the depletion widths a 2D problem.

As we will further show, it is beneficial to operate the modulator at lower bias voltages, where the initial MATLAB model is in good agreement with the Sentaurus simulations. Also the model in Figure 31 requires using depletion widths computed by Sentaurus rather than using depletion widths estimated from the 1D equations, solved in MATLAB. Given all of the above we need to use the initial MATLAB model to perform optimization over geometry, at lower bias voltages.

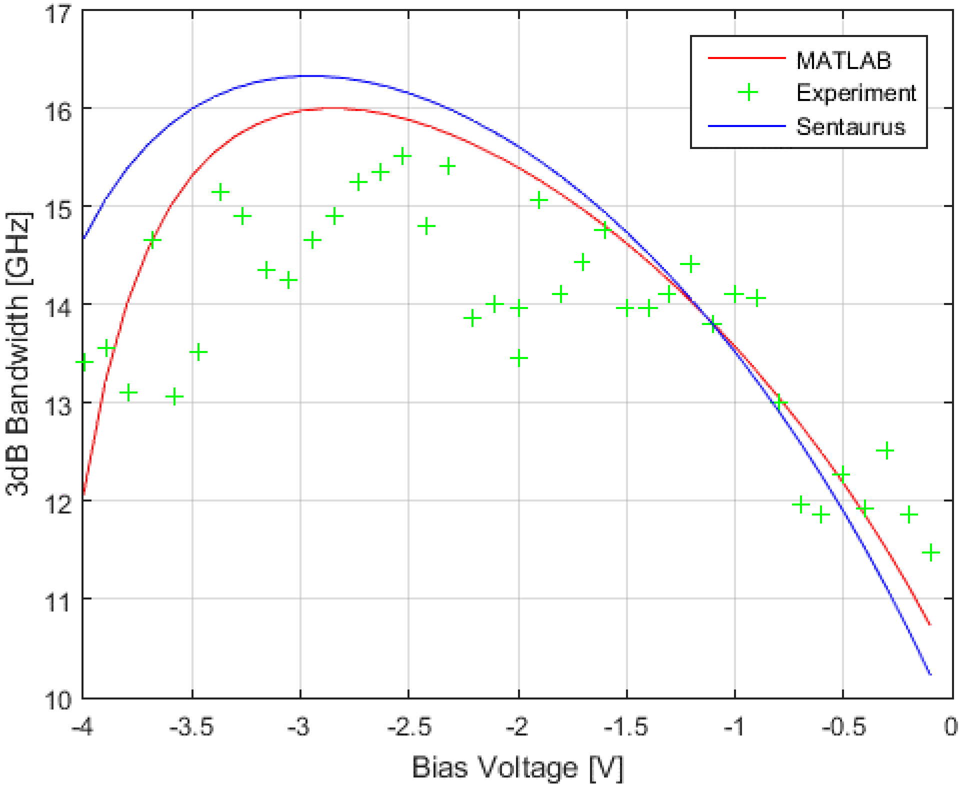

Figure 31. MATLAB simulations yield pretty good agreement with the Sentaurus model after the widths of the depletion regions taken from Sentaurus simulations rather than estimated by solving the 1D depletion equations.

One interesting phenomenon that is predicted by the theory and is observed experimentally, and as far as we know not reported previously, is the existence of the "optimal voltage" for bandwidth, which occurs at around -2.6V reverse bias.

The "optimal voltage" occurs when the spoke is depleted too much and the resistance increase due to wide depletion overwhelming the benefit of decreased junction capacitance. For junctions that are symmetric, where the P and N spokes are doped equally, this optimal voltage occurs at much higher voltages, higher than breakthrough of the diode.

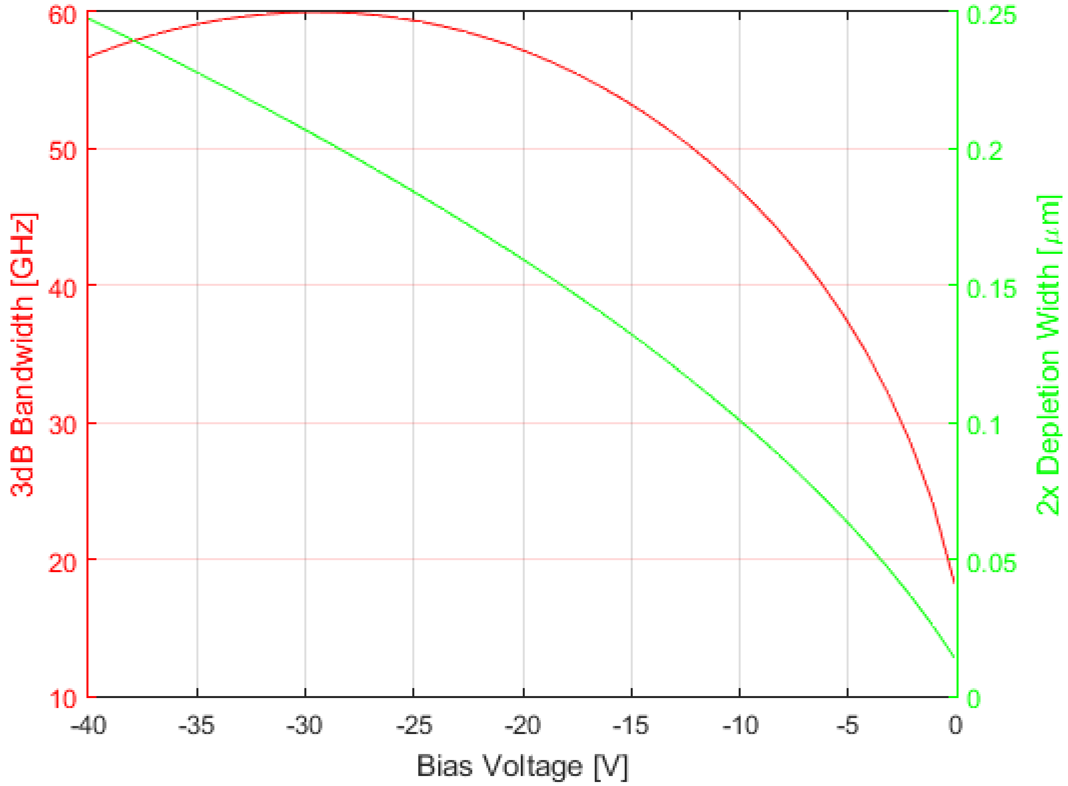

Figure 32. MATLAB Model. The junction is a symmetric PN junction with N_A=N_D=10^{18}cm^{-3} and width of the junction $0.35\ \mu m$. The optimal voltage occurs at -29.8V, much higher than typical breakdown voltages. The optimal voltage occurs when 2X depletion width (we need the factor of 2 because the junction is depleted from both sides) is roughly 2/3 width of the junction.

As can be seen in Figure 32, when the junction is symmetric ($N_A=N_D=10^{18}cm^{-3}$) the optimal voltage occurs at -29.8V, which is higher than typical breakdown voltages at this doping. The fact that the optimal voltage is so high for symmetric junctions is a partial explanation for why it has not been reported, given that most of the junctions are symmetric [40]. The optimal voltage happens when the 2X depletion width of the spoke is roughly 2/3 the width of the spoke $(0.35\ \mu m)$. We need the factor of 2X because the spoke is being depleted from the left and from the right.

However, as we have established in 2.2.2, there are certain bandwidth benefits to creating asymmetric junctions, specifically heavier doped P and lighter doped N. This allows us to increase the bandwidth by 2X while keeping the energy consumption the same. If the junction is not symmetric, one of the sides will get depleted much faster than the other and thus the N junction will be 2/3 depleted at much lower voltages.

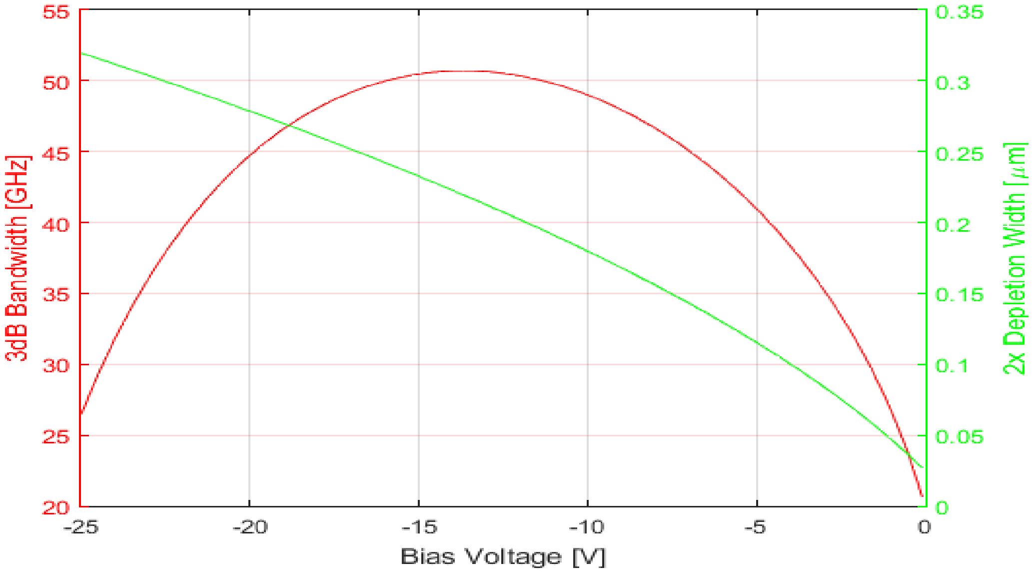

Figure 33. MATLAB Model. The junction geometry is kept the same as in Figure 32 but the doping is $N_A=10^{18}cm^{-3}$ and $N_D=5*10^{17}\ cm^{-3}$. This causes the N spoke to get half depleted at much smaller voltages. We can see that the optimal voltage occurs at -13.4V.

This can be observed in Figure 33, the junction width was kept at $0.35\ \mu m$ but the doping is $N_A=10^{18}cm^{-3}$ and $N_D=5*10^{17}\ cm^{-3}$. This causes the N junction to get 2/3 depleted at a much smaller voltage and thus cause the optimal voltage earlier (-13.4V). It is interesting to observe that the ratio of the depletion width to the overall width, at the optimal voltage, is roughly the same for Figure 32 and Figure 33.

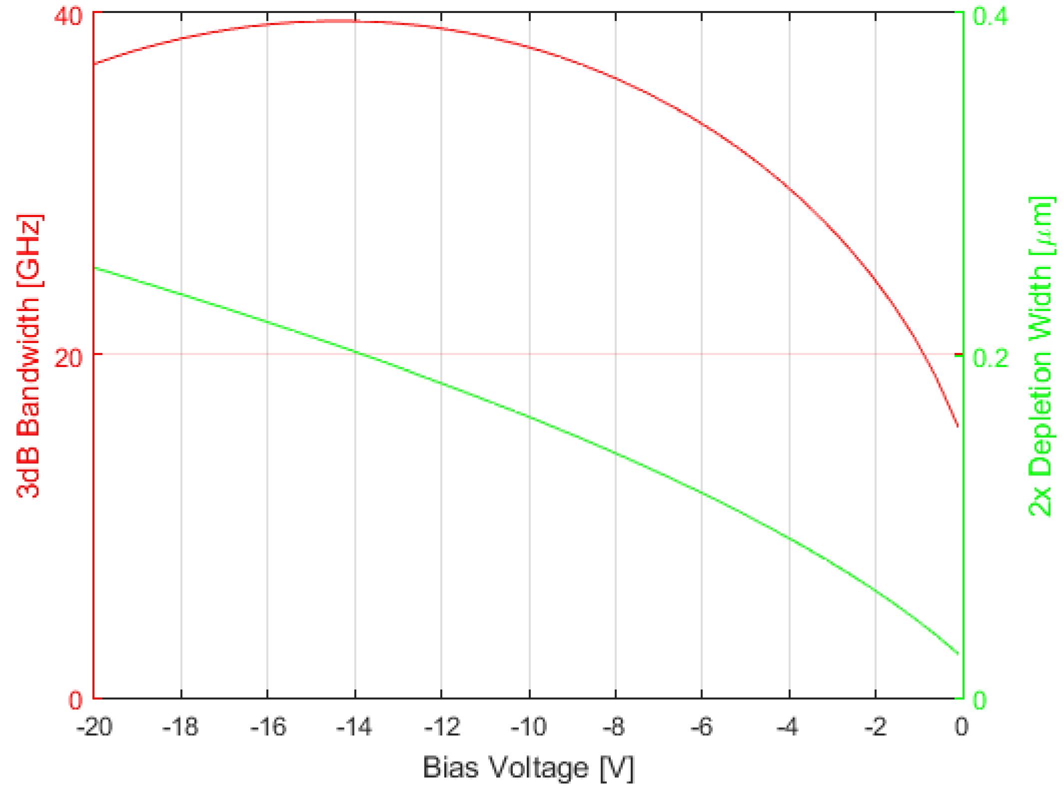

Figure 34. MATLAB Model. A symmetric junction with smaller doping that the one in Figure 32, with $N_A=N_D=5*10^{17}cm^{-3}$. The optimal voltage now occurs at -14.4V versus -29.8V for $10^{18}cm^{-3}$ doping.

Another expected effect is that the optimal voltage will occur at smaller voltages if the doping is lighter, since the depletion width increases with lower doping. This can be observed in Figure 34, with $N_A=N_D=5*10^{17}cm^{-3}$ occurring at -14.4V versus -30.3V in Figure 32. Again we can see that the optimal voltage occurs when the spokes are roughly 2/3 depleted. Since the optimal voltage for Figure 33 and Figure 34 is roughly the same, we can conclude that the voltage is dictated by the lighter doping. This makes sense intuitively since it is the lighter doped side which is depleted faster.

The optimal voltage, if smaller than -10V (which is assumed to be the breakdown voltage), for doping ranging from 10^{17} to 10^{19} is represented in Figure 35. As we go to higher doping, the optimal voltage is beyond the breakdown voltage of the junction. We can again observe that the lighter doped side dictates the optimal voltage.

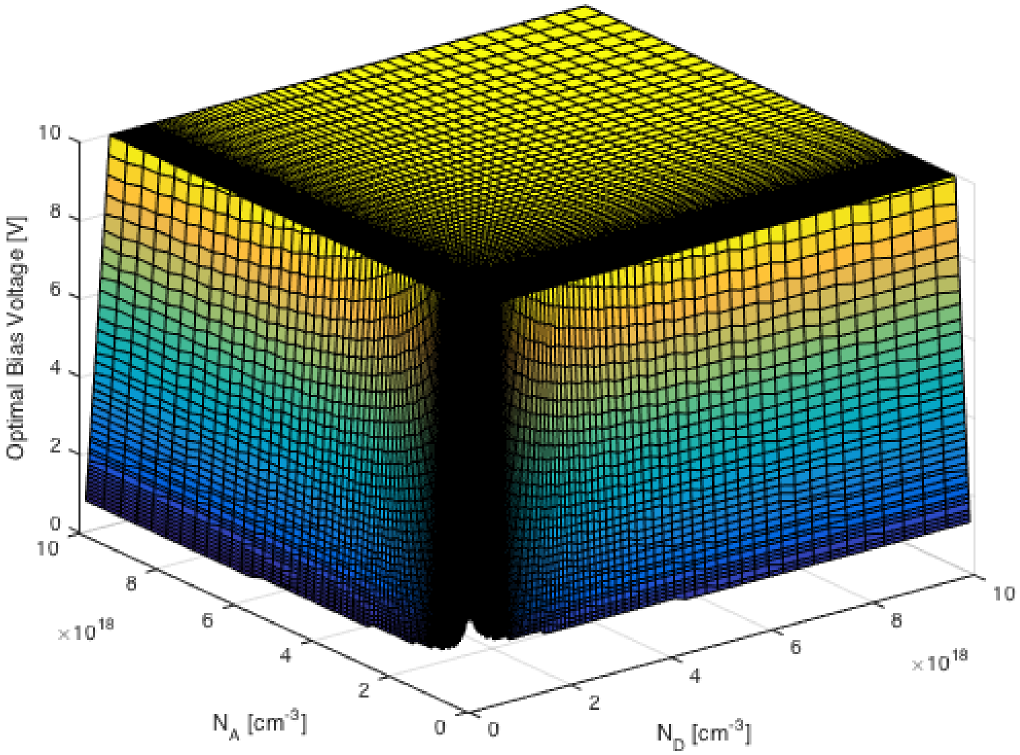

Figure 35. MATLAB model. Optimal voltage as a function of doping.

3.4. Energy Optimization

Before further optimizing the junction, we would like to stop for a moment and think about how to make our modulator more energy efficient. Assume we are at a bias voltage $V_{bias} = -1V$ and we want to know how to better improve our bandwidth. We have two choices: by increasing the bias voltage or by increasing the doping. We want to know which of these two options gives us a smaller increase in energy consumption. We will argue that increasing the doping yields a smaller energy increase. This makes sense intuitively since the energy depends as square on the voltage and only as square root on the doping (through the junction capacitance). We shall however prove the above statement with more mathematical rigor.

The above problem can be reduced to the following mathematical statement:

$$(\frac{df}{dE})_{N_A,N_D=Const} < (\frac{df}{dE})_{V=Const}$$

Where the subscript indicates which variable is held constant during the differentiation and f is the 3dB frequency. We can decompose the above inequality as follows:

$$\frac{df}{dV}\frac{dV}{dE} < \frac{df}{dN}\frac{dN}{dC}\frac{dC}{dE}$$

Where N can be either N_A or N_D depending which one yields better increase in bandwidth, and C is the capacitance of the device. We know that:

$$\frac{dV}{dE} = \frac{1}{CV}$$

And that:

$$\frac{dC}{dE} = \frac{2}{V^2}$$

If we make the assumption that the built in potential, φ_{bi} is very weakly dependent on the doping, we can deduce that:

$$\frac{dN_A}{dC} = \frac{1}{Const} \frac{2\sqrt{\frac{N_A N_D}{N_A + N_D}}(N_A + N_D)^2}{N_D^2}$$

Where $Const$ is a constant that does not depend on doping and is equal to:

$$Const = \frac{C}{\sqrt{\frac{N_A N_D}{N_A + N_D}}}$$

We can manipulate the above equation to give us:

$$\frac{dN_A}{dC} = \frac{1}{Const} \frac{2\frac{N_A N_D}{N_A + N_D}(N_A + N_D)^2}{\sqrt{\frac{N_A N_D}{N_A + N_D}} N_D^2} = \frac{2N_A N_D (N_A + N_D)^2}{N_A + N_D} \frac{1}{C N_D^2} = \frac{2N_A(N_A + N_D)}{C N_D}$$

Thus the original inequality then becomes:

$$\frac{df}{dV}\frac{dV}{dE} < \frac{df}{dN}\frac{dN}{dC}\frac{dC}{dE}$$

$$\frac{df}{dV}\frac{1}{CV} < \frac{df}{dN_{A,D}} \frac{4N_{A,D}\left(N_{A,D} + N_{D,A}\right)}{C N_{D,A} V^2}$$

$$\frac{df}{dV} < \frac{df}{dN_{A,D}} \frac{4N_{A,D}\left(N_{A,D} + N_{D,A}\right)}{N_{D,A}|V|}$$

With the choice of where to change N_A or N_D dependence on which carrier maximizes the df/dN at that specific point.

If we set the bias to V=-1V the ratio of 3dB increase in bandwidth when varying doping to when varying voltage is represented in Figure 36, on a log scale. We can see that increasing doping is always more beneficial than increasing the voltage.

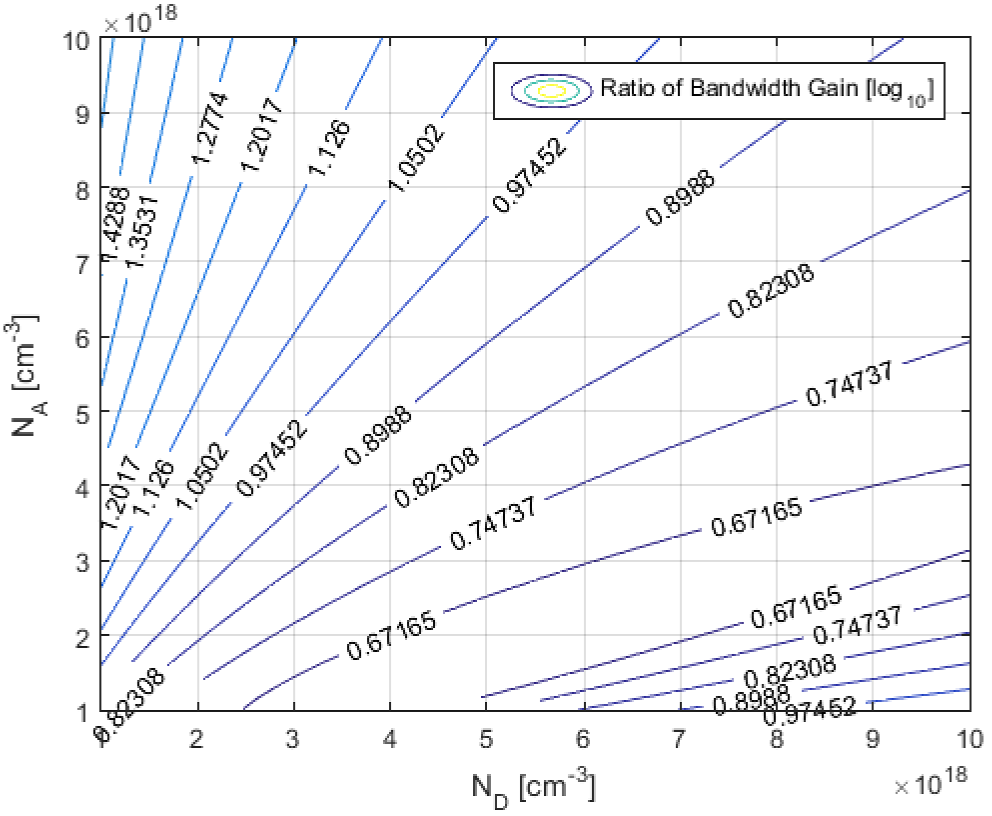

Figure 36. Ratio of 3dB increase when changing doping over when changing voltage on a $\log_{10}$ scale (V=-1V). As expected, it is always more beneficial, in terms of energy, to increase the doping rather than to increase the voltage. On average for the same increase in energy the frequency will increase 41X times more if we vary the doping. The minimum gain is 4X.

Since our statement is true for V=-1V it will also be true for all the other operational points because due to the existence of the optimal voltage, lower biases will present the biggest $\frac{df}{dV}$. The derivative will decrease as we increase the voltage, reaching 0 at the optimal voltage.

3.5. Geometry Optimization

Following the argument from the section above, we will be operating at V=-1V bias point. We will now optimize the geometry of the PN junction. We will use our MATLAB model as a guide since at low bias voltages MATLAB is in good agreement with Sentaurus simulations and experimental results.

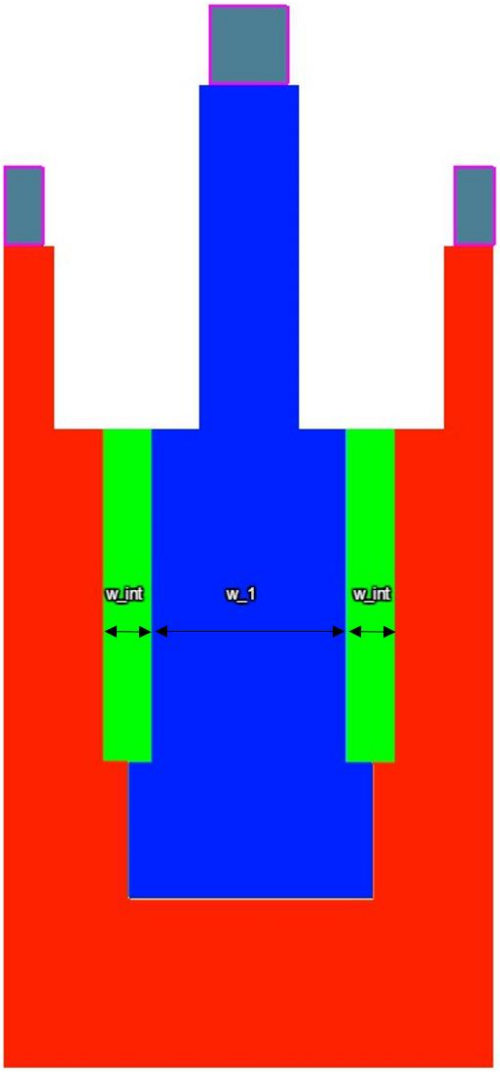

Figure 37. Parameters over which we can optimize.

The two parameters that we can optimize are w_1, the width of the P and N junctions in the middle section, and w_{int}, the width of the intrinsic region (Figure 37). All the other parameters are set by electromagnetic restrictions or layout restrictions. For example the tip of the T-Junction should be located in the center of the optical mode, to optimize ER. The length of the PN junction is the minimum required for the optical mode not to overlap with the metal contacts, causing significant optical loss.

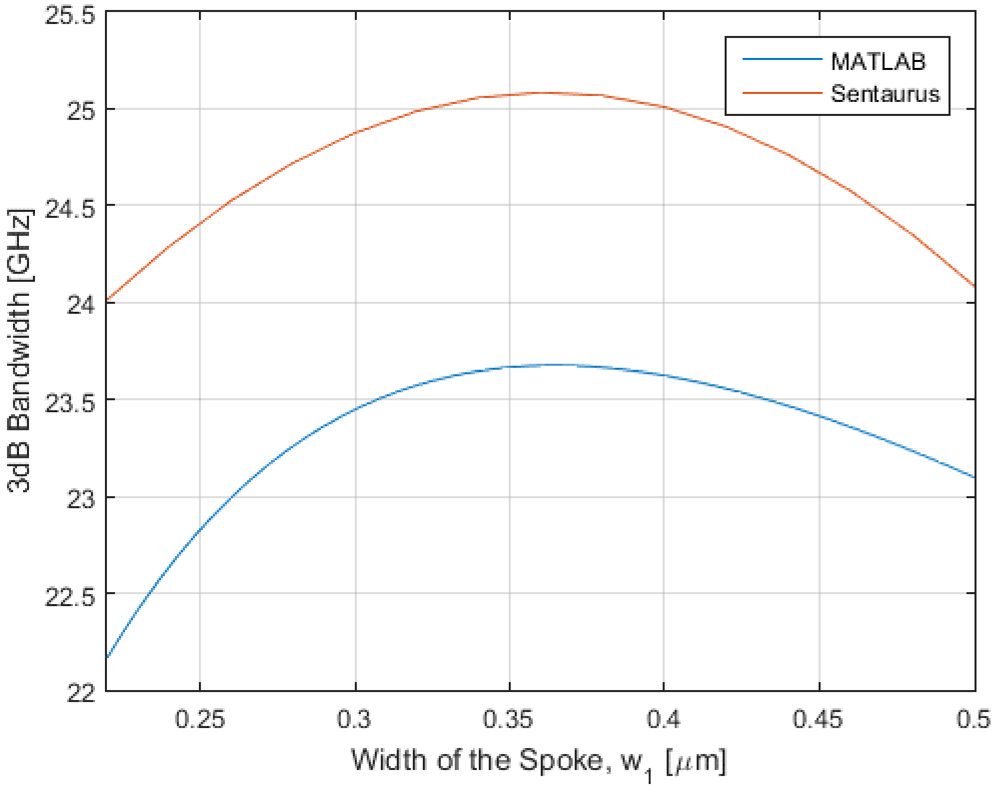

Figure 38. Optimization over w_1 at $N_A = N_D = 10^{18} cm^{-3}$ and $V = -1V$. The Sentaurus simulations predicts a maximum of $f_{3dB} = 25.1\ GHz$ at $w_1 = 0.36\mu m$ and the MATLAB model predict a $f_{3dB} = 23.7GHz$ for $w_1 = 0.37\mu m$.

First let us try to optimize the original geometry, over w_1. We expect a maximum because the wider the junction gets the smaller the resistance along the length of the junction becomes but in the same time the resistance along the width of the junction increases as well, causing a maximum. For a doping of N_A=N_D=10^{18}cm^{-3} and V=-1V, the Sentaurus simulations predicts a maximum at $w_1 = 0.36\ \mu m$ of $f_{3dB} = 25.1\ GHz$ whereas the MATLAB model predicts a maximum at $w_1 = 0.37\ \mu m$ of $f_{3dB} = 23.7\ GHz$, showing good agreement between simulations and MATLAB (Figure 38).

The next optimization of the original geometry is over w_{int}. We are expecting a maximum here because as w_{int} increases the parasitic junction capacitance decrease but the resistance along the width of the top part of the T-Junction will increase, causing a maximum. The simulations predict a maximum at $w_{int} = 0.2\mu m$ of $f_{3dB} = 20.3GHz$. The MATLAB model predicts a maximum at $w_{int} = 0.15\mu m$ of $f_{3dB} = 24.1\ GHz$ (Figure 39).

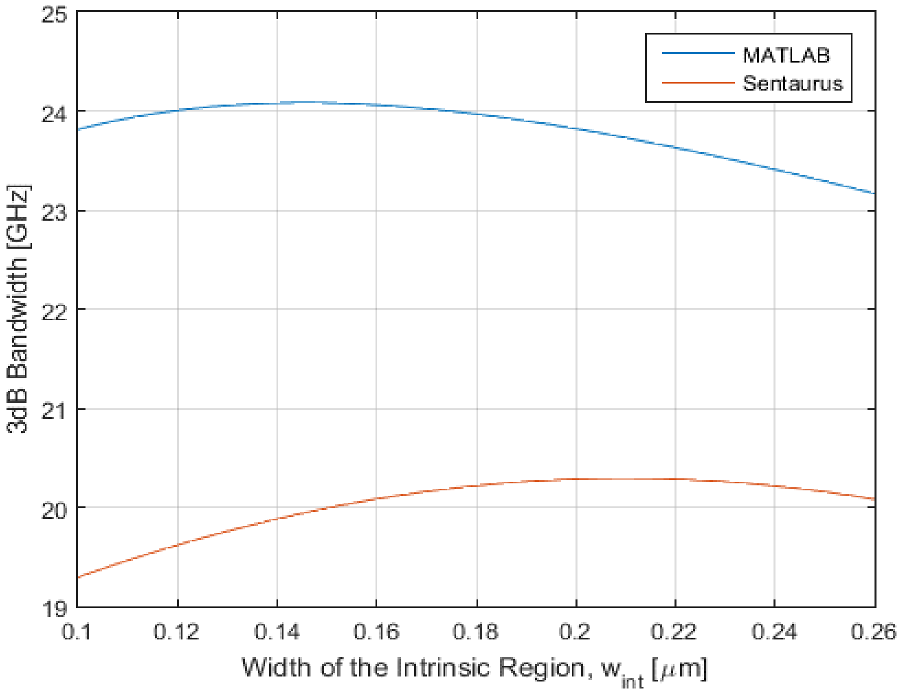

Figure 39. Optimization over w_{int} at $N_A = N_D = 10^{18}cm^{-3}$ and $V = -1V$. The Sentaurus simulations predicts a maximum of $f_{3dB} = 20.3\ GHz$ at $w_{int} = 0.2\mu m$ and the MATLAB model predicts a $f_{3dB} = 24.1GHz$ for $w_{int} = 0.15\mu m$.

In the end we ran a full optimization, over doping and geometry. We have also checked that the energy consumption does not exceed 40 fJ/bit, that the IL is kept under 1dB and that the ER is kept above 5dB. We arrived to a prediction of $f_{3dB} = 38.1\ GHz$ and $f_{3dB} = 30.0\ GHz$ according to MATLAB and Sentaurus respectively, see Table 4 for more details. With a Q of 2,000 the optical bandwidth is kept well above the electrical bandwidth (2.2.5). The IL of 0.96 dB, is just under the 1dB requirement. If we only optimize over geometry we can achieve a bandwidth of 17 GHz, according to Sentaurus. Optimizing only over geometry will allow us to increase the bandwidth without increasing the swing voltage to keep the ER constant.

Table 4. The optimization of the T-Junction modulator over doping and widths.

Model	Frequency [GHz]	$w_1[\mu m]$	$w_{int}\ [\mu m]$	$N_A\ [cm^{-3}]$	$N_D\ [cm^{-3}]$	Q	IL [dB]
MATLAB	38.1	0.32	0.09	10^{19}	10^{19}	2,000	0.96
Sentaurus	30.0	0.47	0.09	10^{19}	10^{19}	2,000	0.96

3.6. Conclusions

In this chapter we have proven that our MATLAB and Sentaurus results are in good agreement with experiment. We have been able to predict the effect of the optimal voltage (Figure 29), an effect that was not previously reported in the literature. The MATLAB model shows good agreement with the Sentaurus simulations at low bias voltages, and can be tweaked to show good agreement at high voltages. However, as proved in 3.4, the device should be operated at low voltages because of the energy savings, thus making the MATLAB model more reliable.

We have then optimized over the widths of the PN junction and doping to obtain a device that exceeds 30 GHz in 3dB bandwidth. This represents more than 2X increase in bandwidth from the previously reported device [23].

Future work on this project would be to fabricate the modulator with the design parameters specified in Table 4 and confirm that a 30 GHz bandwidth is indeed achievable in the T-Junction geometry.

4. Detectors: Bandwidth's Dependency on Intensity

Detectors are devices that perform tasks opposite to the modulators. Detectors convert optical signals into electrical ones, thus acting as RX device of the optical link. A general overview of the detectors has been presented in Section 1.3. In this Chapter we will discuss the effect, so far unexplained, which has been reported in [28]. The measured detectors demonstrated a bandwidth increase with photocurrent (Figure 40b)). We will reproduce this effect in Sentaurus and investigate its causes. We will then propose ways to alleviate this effect, and subsequently explore them through simulation.

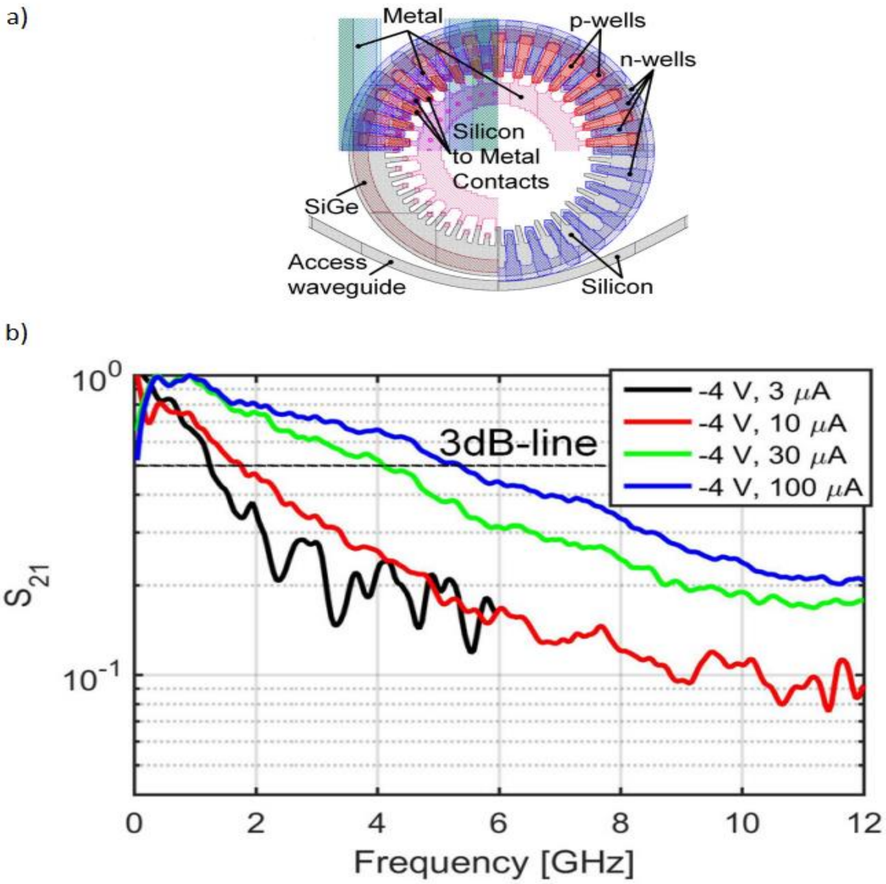

Figure 40. a) The structure of the detector [28]. The ring is divided in four quadrants and different masks are highlighted/ hidden, similarly to Figure 25 b). The additional feature of the detector is the SiGe ring designed to absorb light and generate photocurrent. b) Detectors show bandwidth increase with laser power.

4.1. The Detector

The detectors that will be studied in this Chapter were presented in [28]. Similar to the previously studied modulators, these detectors are ring detectors (Figure 40 a)). The fabrication process is very similar to that of the modulators. We also made use of the T-junction structure since the RC limit is also a limit of the detector's bandwidth. After the P and N wells are fabricated, a partial etch is used to define a 500 nm wide ring of SiGe. The Ge concentration is about 30% [28].

The bandwidth data collected from the detectors indicated a strong dependence of bandwidth on photocurrent. Figure 40 indicates that at a bias voltage of -4 V the 3dB frequency changes as much as 4 GHz when the photocurrent is increased from 3 μA to 100 μA. The literature suggests either no bandwidth dependence on laser power or a decrease in bandwidth due to field cancellation. This effect was not previously reported in the literature and will be discussed at length in this Chapter.

4.2. Sentaurus Model

In this section we will present the Sentaurus simulation model that was used to simulate the detectors. The goal of the simulation was to reproduce the bandwidth dependence on the photocurrent and to use the tools available in Sentaurus to better understand the effect. We started by simulating the detectors, including the T-junction, as well as the 3D structure of the detector. The detector requires a 3D model, unlike the modulator, due to the partial etch of the SiGe. As illustrated in Figure 41, the SiGe's partial etch leaves room for the P and N regions under it. Once the bandwidth dependence on photocurrent was observed, we continued to simplify the geometry of the simulated detector to reduce the simulation time. After each simplification, we checked that the bandwidth dependence was still present.

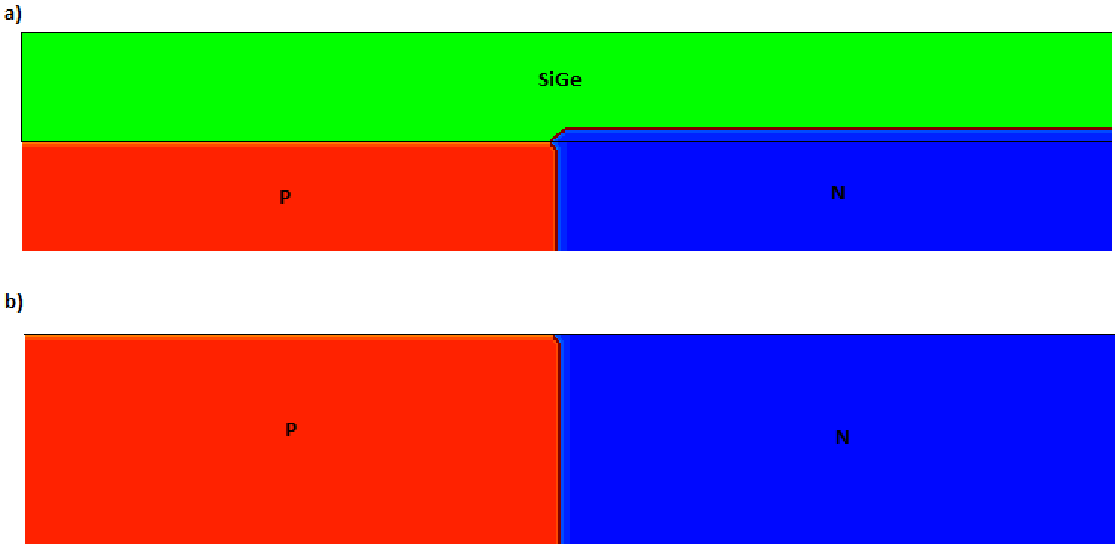

Figure 41. a) The cross section view of the detector in the SiGe region. The picture illustrates the 3D structure of the detector with SiGe's partial etch leaving room for the P and N regions under the SiGe region. SiGe is 50% of the overall thickness. b) The cross section view in the region with no SiGe.

In the end, we managed to reduce the initial detector to a simple 2D lateral PN junction with a SiGe region at its end. This reduced the simulation time from 42 hours to just under an hour, and significantly eased the task of studying the physics underlying the bandwidth dependence on photocurrent. The simplified device, presented in Figure 42, had periodic boundary conditions imposed on its top and bottom, similarly to the modulator in Figure 23. The N region is depicted in red, the P region in blue and the SiGe region in green. The Anode and Cathode contacts are in grey with a pink outline. The beam, at 1200nm, was illuminating the SiGe region, generating photocurrent. Different beam intensities were selected in order to study the bandwidth dependence on the photocurrent.

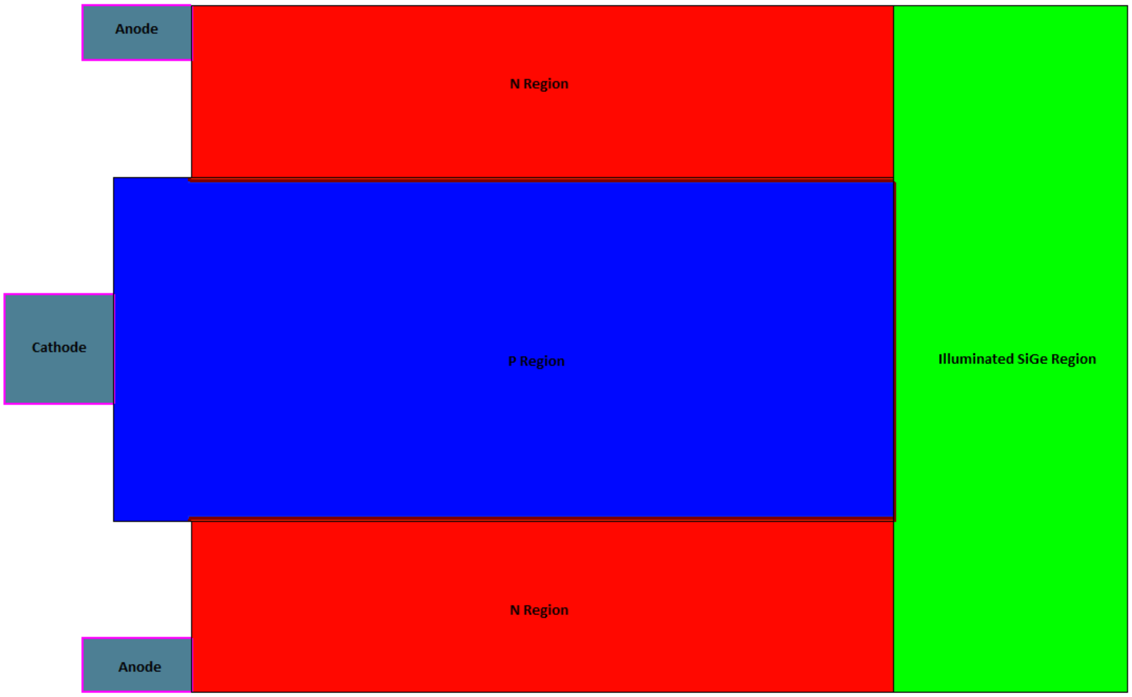

Figure 42. Snapshot of the simulated detector. Similarly to Figure 23, the periodic boundary conditions were imposed on the top and the bottom of the device. The beam was designed to illuminate the SiGe region, the simulation was run at different beam intensities, in order to study the bandwidth dependence on photocurrent.

To reproduce the results illustrated in Figure 40, we had to take into account that the photocurrent reported in Figure 40 is collected by the whole, 30 junction, detector. We set the 3 different beam intensities to generate 33 nA, 0.33 μA, and 3.3 μA of photocurrent, in a single junction. This yielded a total photocurrent of 1, 10, and 100 μA which are the experimental conditions.

4.3. Analyzing the data

In this section we will discuss how we extracted the 3dB bandwidth of the detector and how we extracted the electrical characteristics of the device. One of the factors that can limit the detector's bandwidth is the transit time of the carriers. The transit time is the time that it takes carriers to travel through the depleted, or high-field region. Given the fact that most of the simulations occurred at a high bias voltage of -4V, the electric field presented in the depleted region was around the saturation field. The high electric field resulted in carriers travelling at the saturation velocity, which for Silicon is around 10^7 cm/s (Figure 43). This allows us to estimate that the transit 3dB frequency is on the order of 100 GHz and thus, since we are dealing with bandwidth under 10 GHz, the RC should be considered as the dominant factor in the detector's performance.

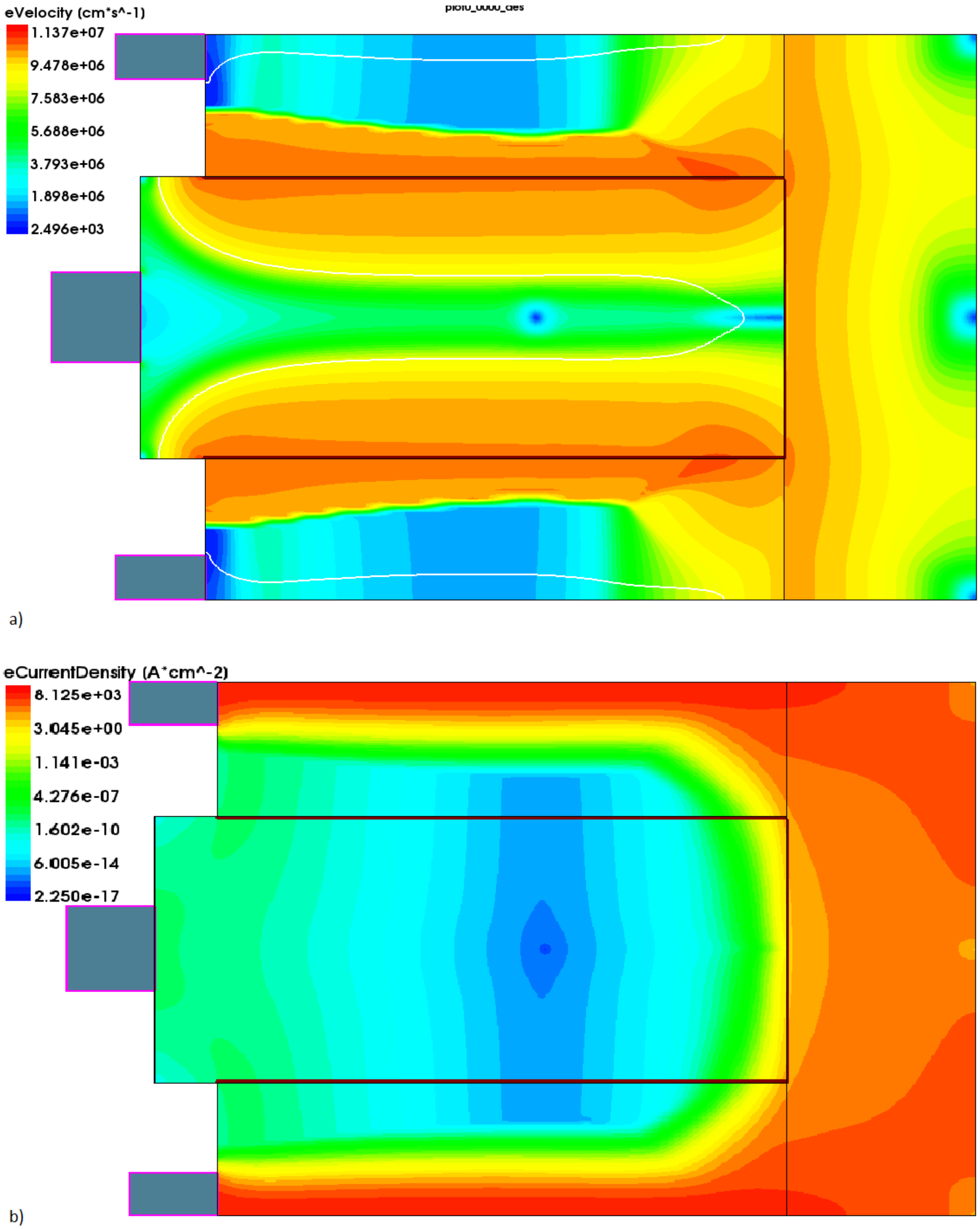

Figure 43. The distribution of the speed a) and current b) of electrons throughout the device. The velocity of the electrons is around 10^7 cm/s, the saturation velocity in Silicon, in the depleted regions, due to a high bias voltage of -4V.

In order to estimate the RC limit we have to think about the detector on a circuit level. We will start with just the resistance of the spokes and the capacitance of the junction. We will analyze the impact of parasitic capacitances and resistances later on in the Chapter. Figure 44 represents the large signal circuit model of the detector. I_{photo} is the current generated in the SiGe region. The spoke resistances are represented with the resistors labeled R_n and R_p. The junction capacitance is C_j, and the bias voltage is V_{bias}. This is a schematic representation of the circuit, ideally we would have a distributed RC ladder, as discussed in 2.2.3.

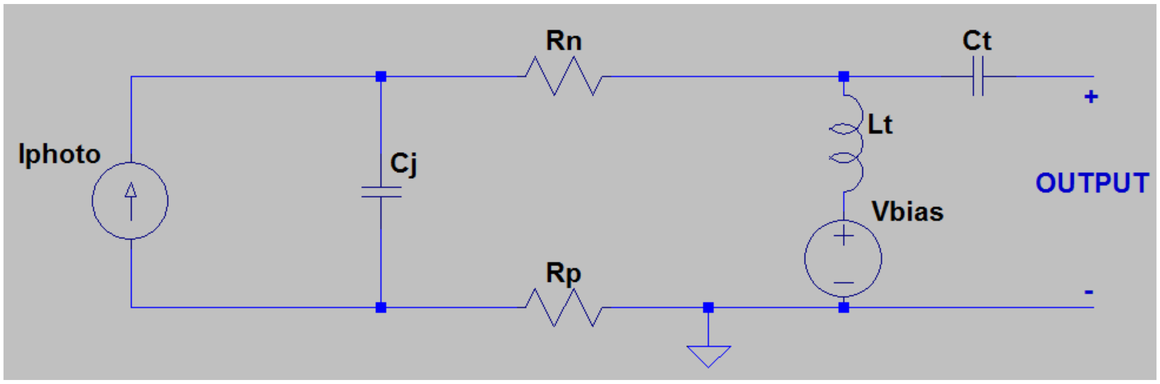

Figure 44. Represents the large signal equivalent circuit model of the detector. I_{photo} is the current generated in the SiGe region, C_j is the junction capacitance, R_n and R_p represent the spoke resistances, and V_{bias} is the bias voltage of the detector. L_t and C_t are the inductor and capacitor of the bias tee, respectively.

We can now run two kinds of simulation. The first type of simulation we will call - an optical simulation and it will help us figure out the 3dB bandwidth of the detector. We impose a small signal photo current through I_{photo} and set V_{bias} at a constant DC bias. The equivalent small signal circuit will then look like in Figure 45 a). The inductor becomes an open circuit for frequencies higher than 100 MHz, and the capacitor can be approximated as a short. To determine the 3dB frequency of the detector we would monitor the current at its terminals and then take the FFT of the current, to determine the 3dB bandwidth.

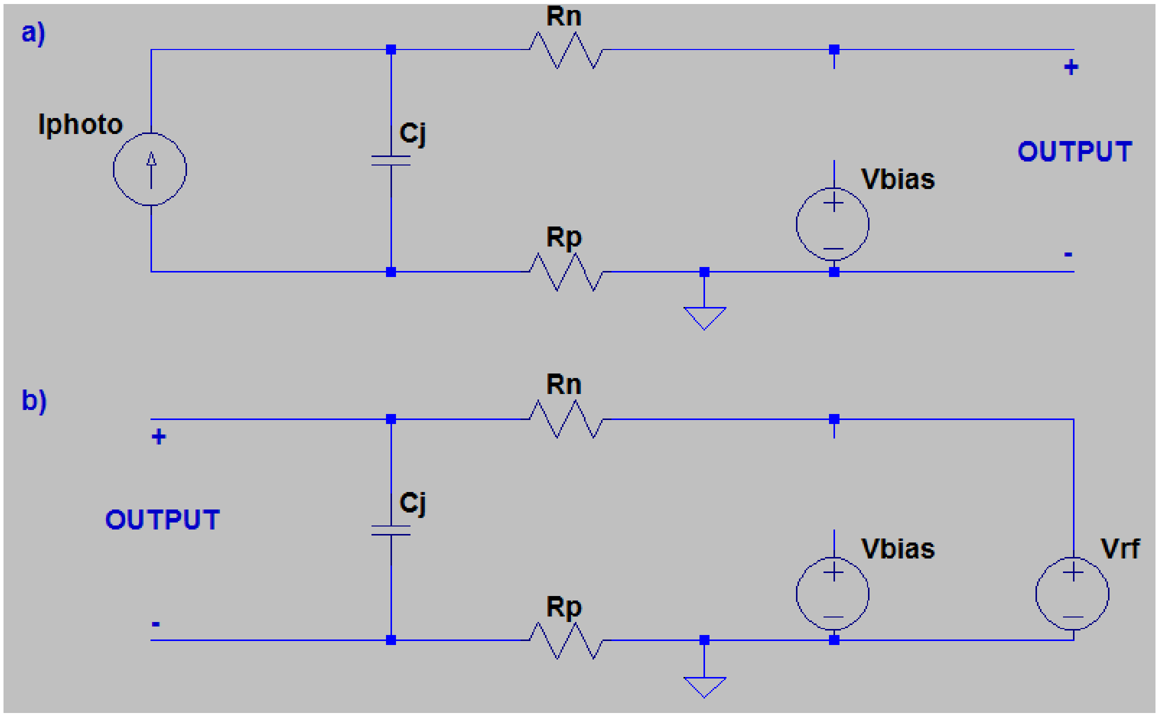

Figure 45. Equivalent small signal circuits used during simulations, the notations are consistent with Figure 44. a) The equivalent circuit for determining the 3dB bandwidth of the detector. b) The equivalent circuit for determining the RC characteristics of the detector.

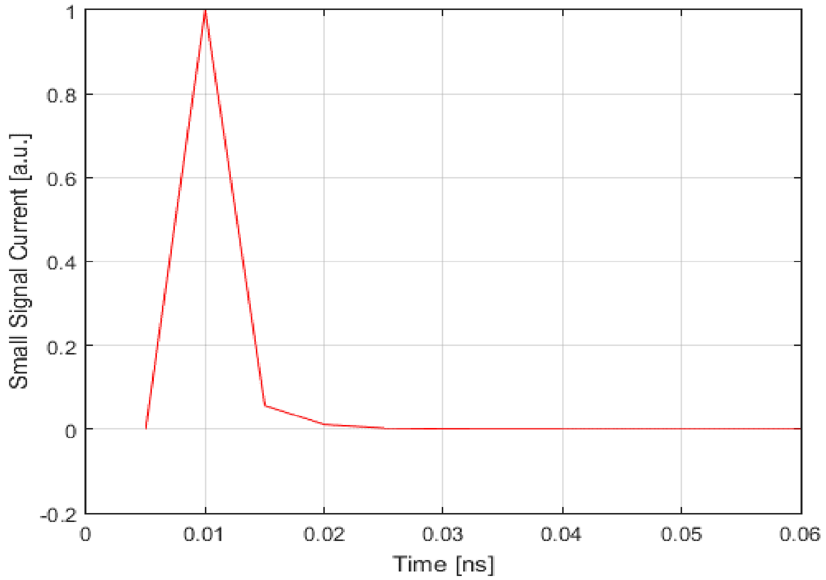

Figure 46 The small signal current recorded as a result of imposing a voltage step on Vbias.

In order to determine the RC characteristics of the detector we would set I_{photo} to a constant current and impose a small signal on $V_{bias.}$ We will call this – the electrical simulation. This would yield a small signal circuit as in Figure 45 b). We could further monitor the small signal current at the terminals and determine the equivalent $R = R_p + R_n$, and C_j. The recorded current is depicted in **Error! Reference source not found.**, R would be estimated as $R = \frac{V_{step}}{I_{peak}}$ (we used the assumption that capacitors are shorted at short times). C_j is computed as $C_j = \frac{Q}{V_{step}} = \frac{\int I dt}{V_{step}}$.

From the optical simulations we could determine if the bandwidth is increasing with photocurrent or not. The electrical simulation would give us the tools to analyze the mechanism underlying the effect observed in the optical simulation. The bandwidth dependence on photocurrent was reproduced and is depicted in Figure 47. We can clearly see that the 3dB frequency increases from 7.8 GHz to 9.6 GHz as the photocurrent goes from 1 μA to 100 μA. The RC frequency extracted from the electrical simulation suggest the same trend. The results are summarized in Table 5. We can observe significant increase in bandwidth at 100 μA of photocurrent. The data Sentaurus data shows similar trends to the experimental data but does not replicate it exactly because we have simulated a simplified version of the detector in order to decrease simulations time, the 3D structures demonstrated lower bandwidths, around 5 GHz. This is might be due to the N and P regions under the SiGe, in a 3D structure – which facilitates the generated carrier extraction. The uncertainty in doping also contributes to the error.

Table 5. The summary of the experimental results and the simulation results.

Photocurrent [μA]	1	10	100
Experimental Bandwidth [GHz]	1.2	1.7	5.3
Sentaurus Bandwidth [GHz]	7.8	7.9	9.6

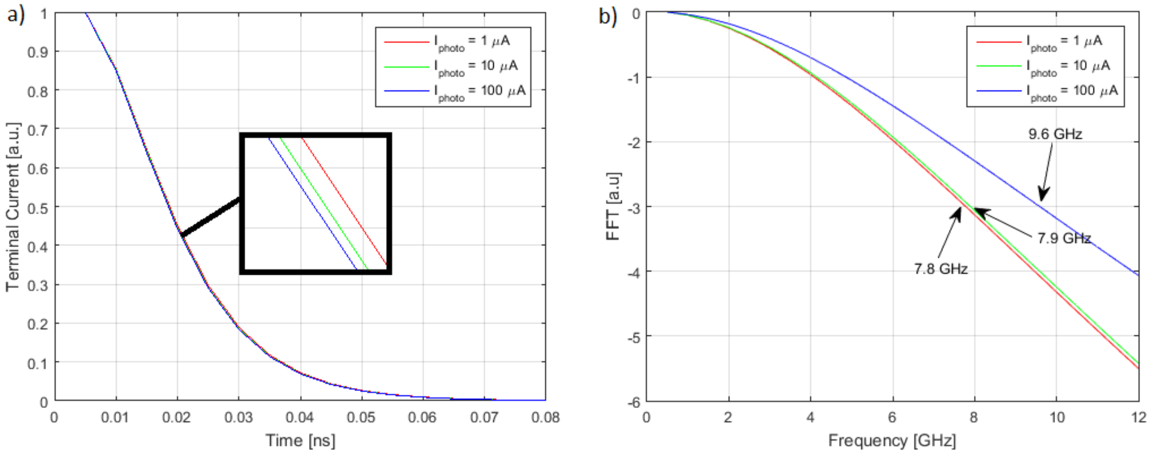

Figure 47. Bandwidth of the detector as a function of photocurrent. Time domain a) and FFT b). As in Figure 40, the bandwidth increases. The 3dB frequency varies from 7.8 GHz to 9.6 GHz with the photocurrent increasing from 1 μA to 100 μA.

4.4. Explaining the Effect

Having elaborated ways to determine the R, C, and the 3dB bandwidth of the detector, and having reproduced the bandwidth increase with photocurrent, we can now proceed to explain the effect. Since the transit time is small enough (4.3), we will primarily focus on the R and C of the detector. As stated above, the RC bandwidth recovers the increase in bandwidth with photocurrent that the optical simulation shows.

First, let's examine what exactly happens to the resistances and capacitances of the detector, when we observe the effect. In Figure 48, we can see three simulations at different photocurrents (1, 10, and 100 μA corresponding to a), b), and c) respectively), and with electron density plotted. The white lines depict the depletion regions. We used

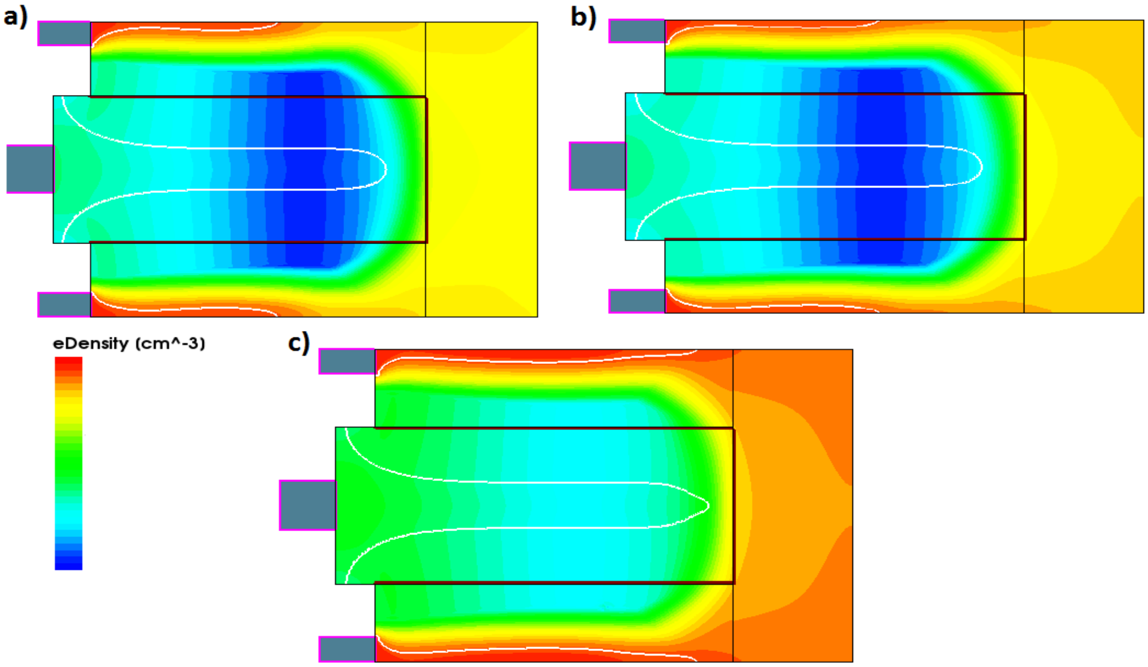

Figure 48. Three simulations with different photocurrent and electron density plotted. The white contours indicate the depletion regions. a) Detector with 1 μA photocurrent. We can see that the device is heavily depleted due to small doping concentrations and high bias voltage, -4 V. b) Detector

with 10 μA photocurrent. The electrons generated by the photocurrent widen the depletion regions a little bit. c) Detector with 100 μA photocurrent. The electrons generated by the photocurrent modify the width and length of the depletion region significantly (compared to a) and b)). Different depletion regions yield different resistances and junction capacitances.

doping consistent with the one used as fitting parameter in Chapter 3. We can observe that the device in a) is heavily depleted as a result of the chosen doping, and high bias voltage (-4 V). Once we inject enough photocarriers, they can modify the shape of the depletion regions, by "repopulating" parts of the detector. The quasi neutral region (QNR) in b) is slightly longer than the one in a), however the repopulating can be observed much better in c) where the photocurrent is much higher than in a) and b) (100 μA instead of 1 and 10 μA, respectively). Due to a higher photocurrent the voltage drop across the resistances of the P and N spokes leads to a smaller voltage that has to be dropped across the depletion regions – therefore activating the previously depleted regions and widening the QNRs (Figure 49). The resistance of the QNR regions is in the tens of kilo ohms.

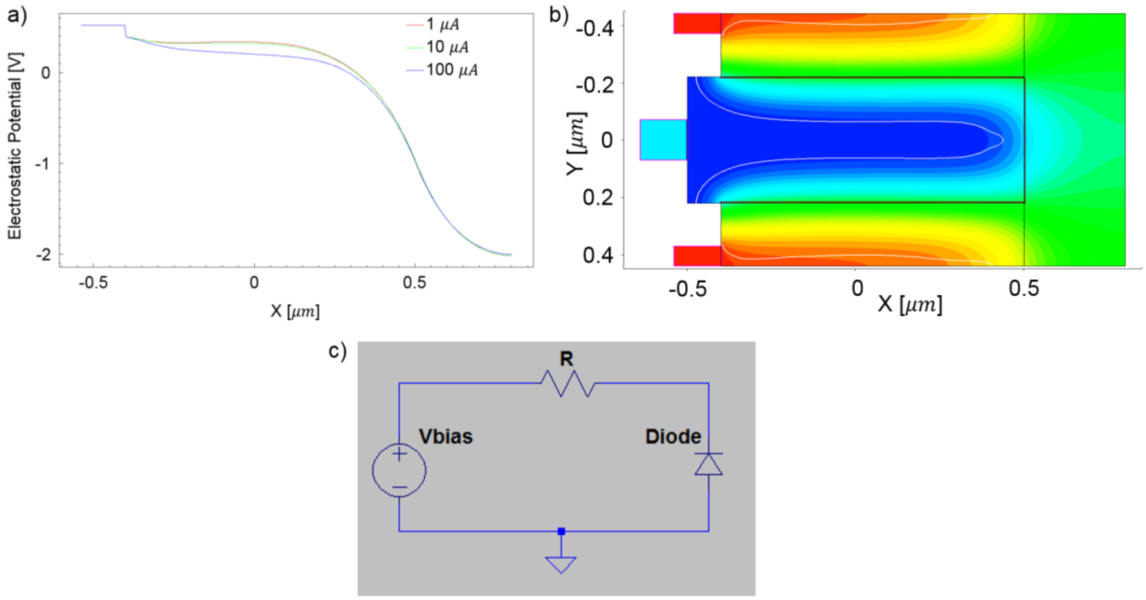

Figure 49. A higher photocurrent will lead to a bigger drop in voltage and widening of the QNR regions. a) The voltage decays faster with higher photocurrent. b) The electrostatic potential

distribution throughout the detector, the potential in a) is plotted along Y=-0.45 and Y=0.45 μm. c) A electrical representation of the detector. The bigger the photocurrent through the resistance, R, the smaller is the voltage across the Diode, thus the regions are less depleted.

We have now realized that at low doping and high reverse biases, the device becomes heavily depleted and the photocarriers can activate the regions of the detectors, when enough of them are injected into the device. The variations in width and length of the active region with photocurrent, leads to different resistances and capacitances at different photocurrents, thus changing the 3dB bandwidth.

Now that we understand how the photocurrent changes the bandwidth, let’s take a closer look at how the resistance and the capacitance changes. Figure 50 depicts the change in resistance and capacitance as we increase the photocurrent. We note that the capacitance change is dominant since the capacitance decreases by 17% while the resistance increases by 7%. The resistance increases with photocurrent because, as shown in Figure 48, the depletion region’s length increases as the device gets “undepleted” by the carriers generated by the photocurrent. However, the resistance does not increase proportionally to the length of the depletion region because as it lengthens, the depletion region also become wider – the two effects cancelling each other.

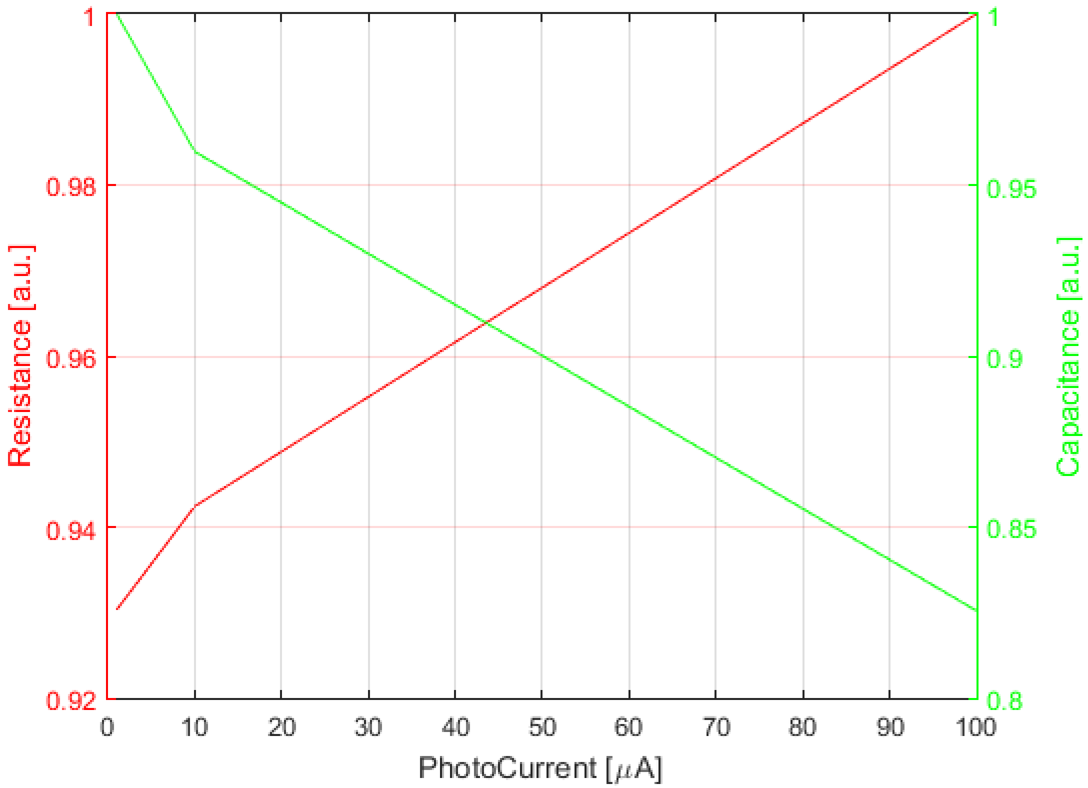

Figure 50. The change in resistance (on the left axis) and in capacitance (on the right axis). The variations in capacitance are bigger - 17% versus only 7% in resistance. The resistance increases with higher photocurrent as the length of the depletion region increases (Figure 48). The resistance does not increase proportionally to the length because as the depletion region lengthens is also becomes wider. The capacitance decrease with photocurrent due to decreasing amount of charge needed to accommodate voltage changes. The RC product recovers the bandwidth in Figure 47.

Even if the resistance increases slightly, the overall 3dB frequency increases because the capacitance decreases. To understand the decrease in capacitance we need to think in terms of differential charge i.e. the charge needed to be supplied in order to accommodate a change in voltage. When the N region is highly depleted, as in Figure 48 a) and b) the difference in length between the active P and N regions are significant. Therefore when there is a change in voltage, the N region has to grow both laterally and in length. However when the P and N active regions are bigger, as in Figure 48 c), the charge needs to only be supplied to the sides of the N region. Therefore less charge has to be supplied at higher photocurrent, diminishing the capacitance (Figure 51).

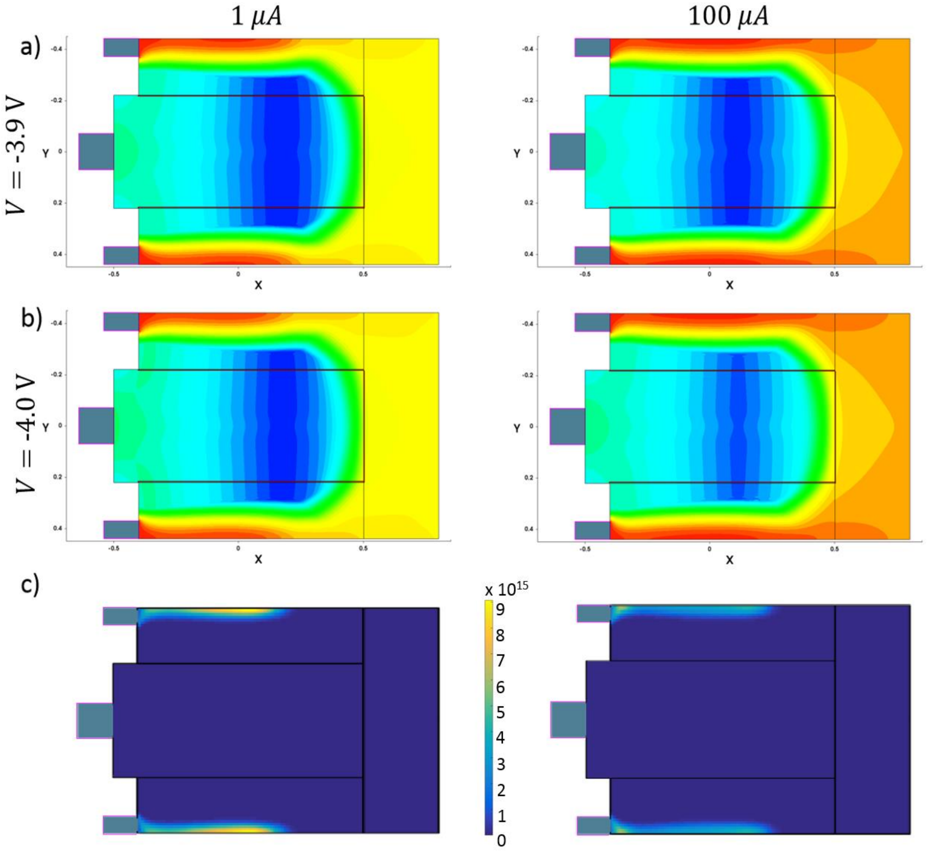

Figure 51. All the devices on the left are at 1 μA of photocurrent and the ones on the right at 100 μA. a) The electron density in the detectors at -3.9 V bias. b) The electron density in the detectors at -4 V bias. c) The difference between a) and b). We can easily observe that for the 1 μA case, there has been a lot of charge supplied to the N regions since the QNR region has to grow laterally and in length. For the 100 μA case the charge supply is very small, corresponding to a smaller capacitance.

An additional reason for why the 3dB bandwidth increases, is the transit time. The transit 3dB frequency is around 10x the RC 3dB frequency. However, when the N region becomes “undepleted” and the transit region shrinks, the transit frequency is around 20x the RC frequency. The total frequency is computed as $f = \frac{f_{3dB}*f_{transit}}{f_{3dB}+f_{transit}}$, thus the transition from 10x to 20x contributes roughly 5% increase in the total frequency (around 0.5 GHz for $f_{3dB} = 10GHz$).

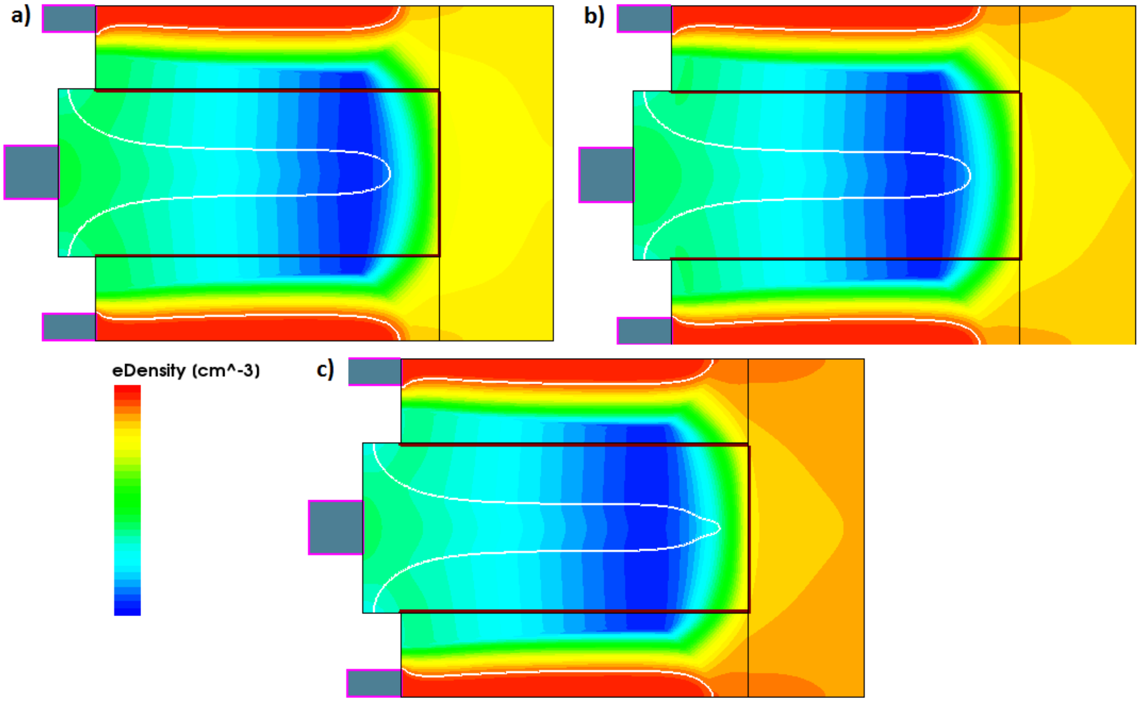

Figure 52 Three simulations with different photocurrent, biased at -4V. We can see that because the doping is increased, the N region is not as depleted as previously, and thus the photocurrent does not significantly modify the RC or the transit time.

We now have an understanding of why the bandwidth increases with photocurrent. A simple solution for the problem is to increase the doping, thus not allowing the photocurrent to significantly impact the bandwidth. Figure 52 shows 3 simulations – a), b), and c) with 1, 10, 100 μA of photocurrent respectively. The doping is higher, by 20%, than in Figure 48 but the bias voltage was kept at -4V. We can observe that the N region is not as heavily depleted as previously and thus the photocurrent does not have a significant say in determining the RC constant or the transit times. The 3dB bandwidth associated with the three simulations are 13.5 GHz for a) and b) and 13.4 GHz for c). Thus increasing the doping helps alleviate the bandwidth dependence on photocurrent.

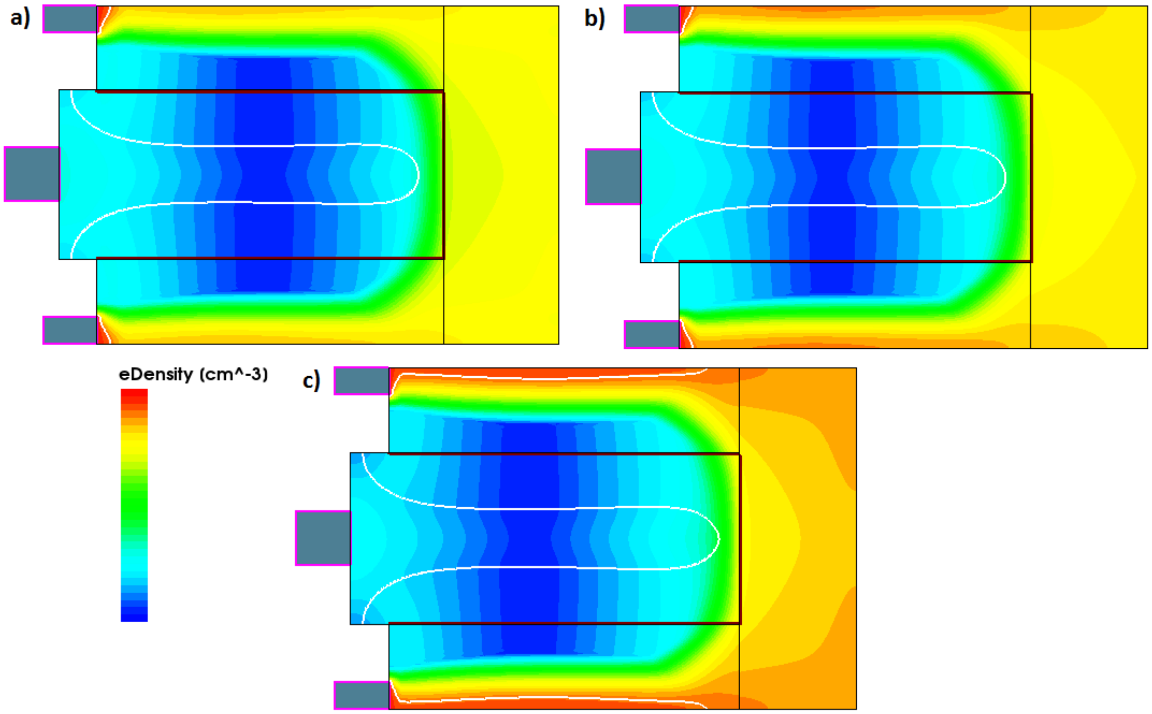

Figure 53. Three simulations with different photocurrents at -4V bias. The N region is weakly doped and in a) and b) it is severely depleted. c) displays a bigger active region due to photocarriers.

We have thought about what happens if we increase the doping, now let us try to understand what happens if we significantly decrease the doping. If we decrease the doping, let's say for simplicity of the N side, the N side will be heavily depleted. Figure 53, displays three simulations at -4V bias and with the same photocurrents as in the previous simulations. The N side is very lightly doped and therefore significantly depleted. Figure 53 a) and b) display very narrow active regions, the active region becomes bigger in c) due to photocarries. When the junction is depleted heavily, the bandwidth actually decreases with photocurrent. Figure 53 a), b), and c) demonstrate a 3dB bandwidth of 13.1, 13.0 and 12.46 GHz, respectively. This is due to the fact that both the resistance and capacitance increase because of an increased length of the active region. The slight increase in width does not counteract the significant increase in length in case of the resistance. The incremental charge reasoning for decreased capacitance does not hold true anymore, due to large increase in length. Overall the bandwidth decreases.

In this part of Chapter 4, we have seen that when the doping is big enough, the bandwidth is independent of photocurrent. When the doping is moderate the bandwidth will increase with photocurrent, reproducing the effects observed experimentally. Once we decrease the doping radically, the bandwidth will actually decrease with photocurrent due to the increased length of the active regions. Overall, increasing the doping of the P and N regions is a viable solution to the bandwidth dependence on photocurrent.

4.5. Parasitics

In this part of Chapter 4, we will examine the effect of parasitics on bandwidth dependence on photocurrent. A large signal circuit representation of the detector, including the parasitics is shown in Figure 54. The difference between the new schematics and Figure 44 are R_{shunt} and $C_{pad.}$ R_{shunt} allows us to treat the photocurrent generated in the SiGe region as a non-ideal current source. R_{shunt} accounts for the fact that some carriers might recombine in the SiGe or depleted regions, while trying to reach the active region. C_{pad} represents the pad capacitance, and as mentioned in 2.2.1, is on the order of 6fF.

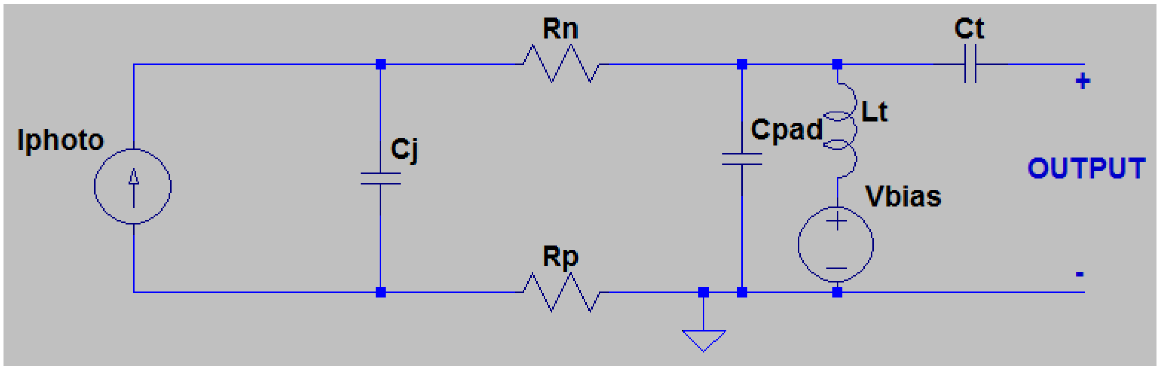

Figure 54. Large signal circuit representing the detector, parasitics included. The differences between the current schematics and Figure 44 are R_{shunt} and C_{pad}. R_{shunt} reflects the fact that the photocurrent generated by the illumination is not a perfect current source, and that some carriers might recombine in the transit regions or SiGe, before reaching the active regions. C_{pad} represents the capacitance of the pads, which as stated in 2.2.1, is on the order of 6fF.

Simulations conducted at different photocurrents and at different bias voltages demonstrate equal currents through the Anode and Cathode, the differences being on the order of 10^{-15} A. This allows us to approximate R_{shunt} as an open circuit, and further neglect it. C_{jun} is on the order of 0.1 fF, thus much smaller than C_{pad} (6fF). The small signal circuit, for optical simulations, is represented in Figure 55. After solving the differential equation for the current flowing through C_{pad}, we get:

$$I_{pad} \propto I_{photo}(1 - e^{-\frac{t}{RC}})$$

Where $R = R_n + R_p$ and $C = \frac{C_j C_{pad}}{C_j + C_{pad}}$. If $C_{pad} \gg C_j$ then $C \to C_j$. This is the case considered in the experiment and in simulation i.e. C_{pad} is simply neglected. However, when the detector is manufactured as part of the circuit, the pad capacitance is much smaller than C_j, in this case it has the effect of minimizing the overall capacitance, and increasing the bandwidth of the circuit. Also, because most of the bandwidth variation with photocurrent come from the variation in C_j, the effect will become less significant.

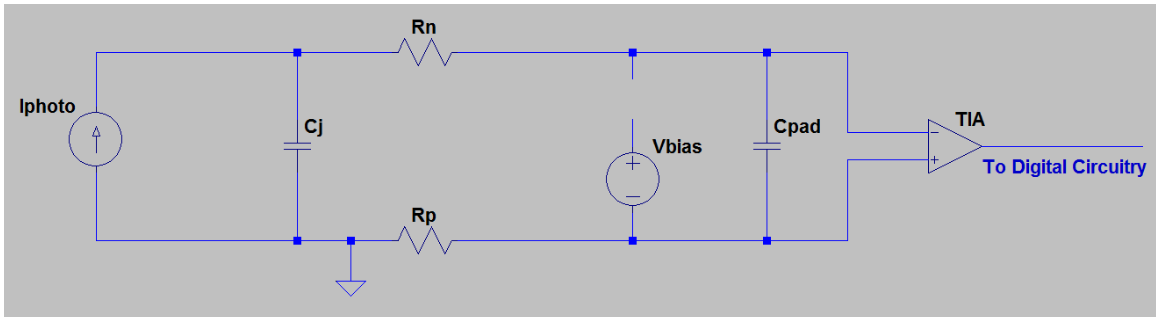

Figure 55. Small signal circuit, including the parasitic $C_{pad} << C_j$. The detector is driving a trans-impedance amplifier which further samples the data through digital circuitry [41].

Measurements of the detector's performance on chip i.e. without pads, confirm the increased bandwidth. In Figure 55, the detector is driving a trans-impedance amplifier (TIA) [41]. There was no bandwidth variation with photocurrent observed, as predicted by the theoretical model above. The measurements were performed by Chen Sun, from UC Berkley. The measured bandwidth at -4 V is around 4 GHz. The measurements were completed at currents ranging from 6 to 40 μA. Therefore, when C_{pad} becomes smaller than C_j, the bandwidth increases due to a smaller RC and the bandwidth dependence on photocurrent decreases, because most of the bandwidth variation comes from the variation in C_j.

4.6. Conclusions

In this Chapter we have explained the bandwidth dependence on photocurrent observed experimentally and reported in [28]. We have reproduced the effect in Sentaurus simulations. We have discovered that because the P and N spokes become heavily depleted, the photocurrent can "undeplete" them by injecting carriers into the depleted regions. Since the width and length of the active region determines the resistance and capacitances of the spoke – the photocurrent can effectively control the RC bandwidth of the detector. Most of the control on bandwidth comes through the junction capacitance which decreases due to a decreased charge needed to be supplied to accommodate a changing bias voltage.

We have demonstrated, through simulations, that the bandwidth dependence on photocurrent disappears when the doping is increased. We also simulated very lightly doped junctions and showed that the bandwidth can actually decrease with photocurrent, due to significant lengthening of the active regions.

We have finally considered the parasitics of the detector. We have shown that having a pad capacitance that is smaller than the junction capacitance can lead to a faster detector, and to a reduced bandwidth dependence on photocurrent. This expectations have been demonstrated through measurement of detectors integrated with electronics i.e. in the absence of big pad capacitances.

Ultimately we have explained the observed effect and elaborated that increasing the doping of the detector or diminishing the pad capacitance can reduce bandwidth dependence on photocurrent.

5. Summary and Future Work

Throughout this Thesis we have discussed topics related to the design of optical modulators and detectors. We have analyzed modulator design from scratch, presented experimental evidence that our models are valid and elaborated designs to be implemented in new tape-outs. Detector design has not been analyzed so thoroughly since we have only dealt with specific effects concerning bandwidth dependence on photocurrent.

5.1. Modulators

We have covered design of optical modulators in Chapters 2 and 3. Chapter 2 has mostly been concerned with building a MATLAB model to accurately predict the behavior of the modulators. We have tested the model against the existing lateral PN junction modulators, presented in [21]. We have concluded, that since the optical mode is not omnipresent throughout the modulator, we only need strong modulation in the outer regions of the device. The idea of the T-junction was developed based on the above mentioned observations, and the MATLAB model confirmed that we can expect significant increase in bandwidth.

Chapter 3 has been dedicated to validation of the T-junction MATLAB model and to further optimizations. We have measured T-junction devices and confirmed their superior bandwidth. We have further created a Sentaurus model and observed strong agreement between MATLAB and Sentaurus models, and experimental data. We have also experimentally observed the theoretically predicted “optimal voltage”. Good correlation between the three sets of data encouraged us to further optimize the T-junction design. In the end we have concluded that a bandwidth in excess of 30 GHz was possible with the T-junction design (Table 6). Increasing the doping however would increase the loss and reduce the ER. To keep the ER constant we would need to increase the voltage swing, which would lead to an increase in energy consumption. Optimizing only over geometry allows us to increase the bandwidth to 17 GHz, at -1V bias, without affecting the ER.

Table 6. The optimization of the T-Junction modulator over doping and widths.

Model	Frequency [GHz]	$w_1 [\mu m]$	w_{int} $[\mu m]$	N_A $[cm^{-3}]$	N_D $[cm^{-3}]$	Q	IL [dB]
MATLAB	38.1	0.32	0.09	10^{19}	10^{19}	2,000	0.96
Sentaurus	30.0	0.47	0.09	10^{19}	10^{19}	2,000	0.96

Further work would include fabrication of modulators with the new designs. Once we can measure the new modulators we can confirm if indeed a 30 GHz bandwidth is achievable with T-junctions. In case it is not, we have to check our MATLAB and Sentaurus models against the new sets of data and account for any discrepancies.

One could spend time designing an optical mode that is narrower than the present one. This would allow to decrease the width of the PN junctions, thus decreasing the RC capacitance and increasing the bandwidth. Decreasing the width of the optical beam would also allow us to modulate it more efficiently, by placing capacitances right at the center of the mode.

Another path worth exploring, is to have different width for the P and N regions. As mentioned in section 3.5, geometrical optimization significantly affect the resistance of the spoke. Since the resistivity of the holes and electrons is different, intuitively, it makes sense to hold the ρ/w (resistivity divided by width) as a constant, leading to a wider P region. This will also allow the ER to increase since the T edge, between the P and N regions will be a longer part of a cell, adding modulating capacitance.

5.2. Detectors

Chapter 4 was dedicated to the experimentally observed bandwidth dependence on photocurrent in detectors. The effect has not been reported prior in the literature, thus Chapter 4 was dedicated to explaining it.

Through Sentaurus simulations, we have concluded that when the P and N junctions are doped lightly, severe depletion of the spokes can be undone by carriers injected by the photocurrent. This allows for a decrease in capacitance and in transit time as the photocurrent increases, thus increasing the overall bandwidth of the detector.

The solution to the above-mentioned effect is to increase the doping of N and P sides, thus avoiding severe depletion of the spokes and dependence on the photocurrent. This can be achieved by selecting mask that have higher doping or by superposing several masks of the same polarity. We have also elaborated electrical circuit equivalents of the detector and concluded that when the parasitic pad capacitances are reduced, the bandwidth dependence can be alleviated and the bandwidth can be increased overall.

Future work on detectors should include fabricating devices with higher doping and verifying experimentally that there is no bandwidth dependence, even with high pad capacitance present.

6. Appendix A: Code Reference

This Appendix contains most of the code used to simulate the devices in MATLAB or Sentaurus.

6.1. Modulator

6.1.1. MATLAB_Theory_Doping_Optimization

```
% Dinis Cheian
% Optimize bandwidth over doping
% High-speed modulator in zero-change CMOS photonics Alloatti et. al.
% With Masetti's Model, used by Sentaurus
clear all
cd('C:\Users\T5810\Dropbox (MIT)\MATLAB\Modulator\Theory\New_Geometry')

w_0= 0.18e-4;                % width of the P and N region before the
intrinsic region
w_1= 0.35e-4;               % width of the P and N region where the
intrinsic region is present
w_in= 0.09e-4;               % width of the top T
w_2=w_in+w_1;               % width of the intrinsic region

l_0p= 0.62e-4;             % P region before the intrnsic portion
l_1p= 0.6e-4;              % P region along the intrinsic region
l_2p= 0.25e-4;             % P region on top of the intrinsic region

l_0n= 0.33e-4;              % N region before the intrinsic region
l_1n= l_1p;                 % same as l_1p but for N
l_2n= l_2p;                 % same as l_2p but for N
l_3n= 0.3e-4;               % N region on top of the P region
t=0.08e-4;                  % thikness of the silicon

%Constants
e_s=11.7*8.84e-14;          % [F/cm] epsilon of the silicon
q=1.6e-19;                  % [C] elementary charge
V_t=25.9e-3;                % [V] thermal voltage
n_i=1e10;                   % [cm^-3] intrinsic concentration of
carriers

%% Find the best fit for experimental data and compare Sentaurus,
MATLAB and Experiment
% Best for Modulator 4: 9.4e16, 7.6e16
% load V_sim.mat
% load f_sim.mat
LetterSize=15;
load V_exp.mat
load f_exp.mat
load V_exp_2.mat
load f_exp_2.mat
load V_sim.mat
```

```
load f_sim.mat
V_exp=[V_exp,V_exp_2];
f_exp=[f_exp,f_exp_2];
f_sim=f_sim/1e9;
V_th=linspace(-0.1,-4,40);
N_A=9.4e16;
N_D=7.6e16;
f_th=NaN(1,length(V_th));
for m=1:length(N_A)
    m
    for n=1:length(N_D)
        for i=1:length(V_th)
                phi(i)=V_t*log(N_D*N_A/n_i^2);
% the build in potential
                % depletion regions with no intrinsic region
                w_n_depl(i)=sqrt(2*e_s*(phi(i)-
V_th(i))*N_A/(q*N_D*(N_A+N_D)));
                w_p_depl(i)=sqrt(2*e_s*(phi(i)-
V_th(i))*N_D/(q*N_A*(N_A+N_D)));
                w_depl(i)=w_n_depl(i)+w_p_depl(i);
                % depletion regions with intrinsic region
                w_n_depl_in(i)=(sqrt(w_in^2+2*e_s/q*(N_A+N_D)*(phi(i)-
V_th(i))/(N_A*N_D))-w_in)/(1+N_D/N_A);
                w_p_depl_in(i)=(sqrt(w_in^2+2*e_s/q*(N_A+N_D)*(phi(i)-
V_th(i))/(N_A*N_D))-w_in)/(1+N_A/N_D);
                w_depl_in(i)=w_n_depl_in(i)+w_p_depl_in(i);
                % P resistance
                R_P0(i)=resistivity('h',N_A)*l_0p*1/(t*w_0);     %
Resistance before the intrinsic region
                R_P1(i)=resistivity('h',N_A)*l_1p*1/(t*(w_1-
2*w_p_depl_in(i)));  % Resistance along the intrinsic region
                R_P1_lat(i)=resistivity('h',N_A)*(w_1/2-
w_p_depl_in(i))*1/(t*l_1p);   % Lateral resistance along the intrinsic
region
                R_P2(i)=resistivity('h',N_A)*(l_2p-
w_p_depl(i))*1/(t*(w_2-2*w_p_depl(i))); % Resistance on top of the
intrinsic region
                R_P2_lat(i)=resistivity('h',N_A)*(w_2/2-
w_p_depl(i))*1/(t*(l_2p-w_p_depl(i))); % Lateral resistance along the
intrinsic region
                % N resistance
                R_N0(i)=resistivity('e',N_D)*l_0n*1/(t*w_0);     %
Resistance before the intrinsic region
                R_N1(i)=resistivity('e',N_D)*l_1n*1/(t*(w_1-
2*w_n_depl_in(i)));  % Resistance along the intrinsic region
                R_N1_lat(i)=resistivity('e',N_D)*(w_1/2-
w_n_depl_in(i))*1/(t*l_1n);   % Lateral resistance along the intrinsic
region
                R_N2(i)=resistivity('e',N_D)*l_2n*1/(t*(w_2-
2*w_n_depl(i))); % Resistance on top of the intrinsic region
                R_N2_lat(i)=resistivity('e',N_D)*(w_2/2-
w_n_depl(i))*1/(t*l_2n); % Lateral resistance along the intrinsic
region
                R_N3(i)=resistivity('e',N_D)*l_3n*1/(t*(w_2-
w_n_depl(i)));
                % Capacitance
```

```
                if ((R_P0(i)>=0) & (R_P1(i)>=0) & (R_P1_lat(i)>=0) &
(R_P2(i)>=0) & (R_P2_lat(i)>=0) &...
                (R_N0(i)>=0) & (R_N1(i)>=0) & (R_N1_lat(i)>=0) &
(R_N2(i)>=0) & (R_N2_lat(i)>=0) & (R_N3(i)>=0))
                    C_1(i)=e_s/(w_depl_in(i)+w_in)*l_1p*t;
% Cap in the intrinsic region
                    C_2(i)=e_s/(w_depl(i))*l_2p*t;
% Capacitance in the T part lateral
                    C_3(i)=e_s/(w_depl(i))*w_2*t;
% Capacitance on the top of the T junction

tau(i)=C_1(i)*(R_P0(i)+R_N0(i)+R_P1(i)/2+R_N1(i)/2+R_P1_lat(i)+R_N1_lat
(i))+...

2*C_2(i)*(R_P0(i)+R_N0(i)+R_P1(i)+R_N1(i)+R_P2(i)/2+R_N2(i)/2+R_P2_lat(
i)+R_N2_lat(i))+...

C_3(i)*(R_P0(i)+2*R_N0(i)+R_P1(i)+2*R_N1(i)+R_P2(i)+2*R_N2(i)+2*R_N3(i)
/2);
                    C(i)=C_1(i)+2*C_2(i)+C_3(i);
                    R(i)=tau(i)/C(i);
                    f_th(i)=1/(2*pi*tau(i))*1/1e9;
                end
        end
        %Sum(m,n)=sum((f_th-f_exp).^2);
    end
end


%% Sweep over all dopings at V=-1

V_th=-1.0;
N_A=logspace(17,19,100);
N_D=logspace(17,19,101)+1e16;
f_th=NaN(length(N_A),length(N_D));
for m=1:length(N_A)
    m
    for n=1:length(N_D)
                phi(m,n)=V_t*log(N_D(n)*N_A(m)/n_i^2);
% the build in potential
                % depletion regions with no intrinsic region
                w_n_depl(m,n)=sqrt(2*e_s*(phi(m,n)-
V_th)*N_A(m)/(q*N_D(n)*(N_A(m)+N_D(n))));
                w_p_depl(m,n)=sqrt(2*e_s*(phi(m,n)-
V_th)*N_D(n)/(q*N_A(m)*(N_A(m)+N_D(n))));
                w_depl(m,n)=w_n_depl(m,n)+w_p_depl(m,n);
                % depletion regions with intrinsic region

w_n_depl_in(m,n)=(sqrt(w_in^2+2*e_s/q*(N_A(m)+N_D(n))*(phi(m,n)-
V_th)/(N_A(m)*N_D(n)))-w_in)/(1+N_D(n)/N_A(m));

w_p_depl_in(m,n)=(sqrt(w_in^2+2*e_s/q*(N_A(m)+N_D(n))*(phi(m,n)-
V_th)/(N_A(m)*N_D(n)))-w_in)/(1+N_A(m)/N_D(n));
                w_depl_in(m,n)=w_n_depl_in(m,n)+w_p_depl_in(m,n);
                % P resistance
```

```
                R_P0(m,n)=resistivity('h',N_A(m))*l_0p*1/(t*w_0);     %
Resistance before the intrinsic region
                R_P1(m,n)=resistivity('h',N_A(m))*l_1p*1/(t*(w_1-
2*w_p_depl_in(m,n)));  % Resistance along the intrinsic region
                R_P1_lat(m,n)=resistivity('h',N_A(m))*(w_1/2-
w_p_depl_in(m,n))*1/(t*l_1p);  % Lateral resistance along the intrinsic
region
                R_P2(m,n)=resistivity('h',N_A(m))*(l_2p-
w_p_depl(m,n))*1/(t*(w_2-2*w_p_depl(m,n))); % Resistance on top of the
intrinsic region
                R_P2_lat(m,n)=resistivity('h',N_A(m))*(w_2/2-
w_p_depl(m,n))*1/(t*(l_2p-w_p_depl(m,n))); % Lateral resistance along
the intrinsic region
                % N resistance
                R_N0(m,n)=resistivity('e',N_D(n))*l_0n*1/(t*w_0);     %
Resistance before the intrinsic region
                R_N1(m,n)=resistivity('e',N_D(n))*l_1n*1/(t*(w_1-
2*w_n_depl_in(m,n)));  % Resistance along the intrinsic region
                R_N1_lat(m,n)=resistivity('e',N_D(n))*(w_1/2-
w_n_depl_in(m,n))*1/(t*l_1n);  % Lateral resistance along the intrinsic
region
                R_N2(m,n)=resistivity('e',N_D(n))*l_2n*1/(t*(w_2-
2*w_n_depl(m,n))); % Resistance on top of the intrinsic region
                R_N2_lat(m,n)=resistivity('e',N_D(n))*(w_2/2-
w_n_depl(m,n))*1/(t*l_2n); % Lateral resistance along the intrinsic
region
                R_N3(m,n)=resistivity('e',N_D(n))*l_3n*1/(t*(w_2-
w_n_depl(m,n)));
                % Capacitance
                if ((R_P0(m,n)>=0) & (R_P1(m,n)>=0) &
(R_P1_lat(m,n)>=0) & (R_P2(m,n)>=0) & (R_P2_lat(m,n)>=0) &...
                (R_N0(m,n)>=0) & (R_N1(m,n)>=0) & (R_N1_lat(m,n)>=0) &
(R_N2(m,n)>=0) & (R_N2_lat(m,n)>=0) & (R_N3(m,n)>=0))
                    C_1(m,n)=e_s/(w_depl_in(m,n)+w_in)*l_1p*t;
% Cap in the intrinsic region
                    C_2(m,n)=e_s/(w_depl(m,n))*l_2p*t;
% Capacitance in the T part lateral
                    C_3(m,n)=e_s/(w_depl(m,n))*w_2*t;
% Capacitance on the top of the T junction

tau(m,n)=C_1(m,n)*(R_P0(m,n)+R_N0(m,n)+R_P1(m,n)/2+R_N1(m,n)/2+R_P1_lat
(m,n)+R_N1_lat(m,n))+...

2*C_2(m,n)*(R_P0(m,n)+R_N0(m,n)+R_P1(m,n)+R_N1(m,n)+R_P2(m,n)/2+R_N2(m,
n)/2+R_P2_lat(m,n)+R_N2_lat(m,n))+...

C_3(m,n)*(R_P0(m,n)+2*R_N0(m,n)+R_P1(m,n)+2*R_N1(m,n)+R_P2(m,n)+2*R_N2(
m,n)+2*R_N3(m,n)/2);
                    f_th(m,n)=1/(2*pi*tau(m,n))*1/1e9;
                end
    end
end

surf(N_D,N_A,f_th);
xlabel('N_D [cm^{-3}]');
ylabel('N_A [cm^{-3}]');
zlabel('3dB Bandwidth [GHz]');
```

```
%% Find the optimal voltages for all dopings
V_th=linspace(-0.1,-10,100);     % operating voltage range
N_A=logspace(17,19,100);
N_D=logspace(17,19,101);
f_th=NaN(length(N_A),length(N_D));
phi=NaN(length(N_A),length(N_D),length(V_th));
w_n_depl=NaN(length(N_A),length(N_D),length(V_th));
w_p_depl=NaN(length(N_A),length(N_D),length(V_th));
w_depl=NaN(length(N_A),length(N_D),length(V_th));
w_n_depl_in=NaN(length(N_A),length(N_D),length(V_th));
w_p_depl_in=NaN(length(N_A),length(N_D),length(V_th));
w_depl_in=NaN(length(N_A),length(N_D),length(V_th));
R_P0=NaN(length(N_A),length(N_D),length(V_th));
R_P1=NaN(length(N_A),length(N_D),length(V_th));
R_P1_lat=NaN(length(N_A),length(N_D),length(V_th));
R_P2=NaN(length(N_A),length(N_D),length(V_th));
R_P2_lat=NaN(length(N_A),length(N_D),length(V_th));
R_N0=NaN(length(N_A),length(N_D),length(V_th));
R_N1=NaN(length(N_A),length(N_D),length(V_th));
R_N1_lat=NaN(length(N_A),length(N_D),length(V_th));
R_N2=NaN(length(N_A),length(N_D),length(V_th));
R_N2_lat=NaN(length(N_A),length(N_D),length(V_th));
R_N3=NaN(length(N_A),length(N_D),length(V_th));
R_N3_lat=NaN(length(N_A),length(N_D),length(V_th));
C_1=NaN(length(N_A),length(N_D),length(V_th));
C_2=NaN(length(N_A),length(N_D),length(V_th));
C_3=NaN(length(N_A),length(N_D),length(V_th));
C_4=NaN(length(N_A),length(N_D),length(V_th));
C_opt=NaN(length(N_A),length(N_D),length(V_th));
C=NaN(length(N_A),length(N_D),length(V_th));
tau=NaN(length(N_A),length(N_D),length(V_th));

for m=1:length(N_A)
    m
    for n=1:length(N_D)
        for i=1:length(V_th)
                phi(m,n,i)=V_t*log(N_D(n)*N_A(m)/n_i^2);
% the build in potential
                % depletion regions with no intrinsic region
                w_n_depl(m,n,i)=sqrt(2*e_s*(phi(m,n,i)-
V_th(i))*N_A(m)/(q*N_D(n)*(N_A(m)+N_D(n))));
                w_p_depl(m,n,i)=sqrt(2*e_s*(phi(m,n,i)-
V_th(i))*N_D(n)/(q*N_A(m)*(N_A(m)+N_D(n))));
                w_depl(m,n,i)=w_n_depl(m,n,i)+w_p_depl(m,n,i);
                % depletion regions with intrinsic region

w_n_depl_in(m,n,i)=(sqrt(w_in^2+2*e_s/q*(N_A(m)+N_D(n))*(phi(m,n,i)-
V_th(i))/(N_A(m)*N_D(n)))-w_in)/(1+N_D(n)/N_A(m));

w_p_depl_in(m,n,i)=(sqrt(w_in^2+2*e_s/q*(N_A(m)+N_D(n))*(phi(m,n,i)-
V_th(i))/(N_A(m)*N_D(n)))-w_in)/(1+N_A(m)/N_D(n));
                w_depl_in(m,n,i)=w_n_depl_in(m,n,i)+w_p_depl_in(m,n,i);
                % P resistance
                R_P0(m,n,i)=resistivity('h',N_A(m))*l_0p*1/(t*w_0);
% Resistance before the intrinsic region
                R_P1(m,n,i)=resistivity('h',N_A(m))*l_1p*1/(t*(w_1-
2*w_p_depl_in(m,n,i)));  % Resistance along the intrinsic region
```

```
                R_P1_lat(m,n,i)=resistivity('h',N_A(m))*(w_1/2-
w_p_depl_in(m,n,i))*1/(t*l_1p);  % Lateral resistance along the
intrinsic region
                R_P2(m,n,i)=resistivity('h',N_A(m))*(l_2p-
w_p_depl(m,n,i))*1/(t*(w_2-2*w_p_depl(m,n,i))); % Resistance on top of
the intrinsic region
                R_P2_lat(m,n,i)=resistivity('h',N_A(m))*(w_2/2-
w_p_depl(m,n,i))*1/(t*(l_2p-w_p_depl(m,n,i))); % Lateral resistance
along the intrinsic region
                % N resistance
                R_N0(m,n,i)=resistivity('e',N_D(n))*l_0n*1/(t*w_0);
% Resistance before the intrinsic region
                R_N1(m,n,i)=resistivity('e',N_D(n))*l_1n*1/(t*(w_1-
2*w_n_depl_in(m,n,i)));  % Resistance along the intrinsic region
                R_N1_lat(m,n,i)=resistivity('e',N_D(n))*(w_1/2-
w_n_depl_in(m,n,i))*1/(t*l_1n);  % Lateral resistance along the
intrinsic region
                R_N2(m,n,i)=resistivity('e',N_D(n))*l_2n*1/(t*(w_2-
2*w_n_depl(m,n,i))); % Resistance on top of the intrinsic region
                R_N2_lat(m,n,i)=resistivity('e',N_D(n))*(w_2/2-
w_n_depl(m,n,i))*1/(t*l_2n); % Lateral resistance along the intrinsic
region
                R_N3(m,n,i)=resistivity('e',N_D(n))*l_3n*1/(t*(w_2-
w_n_depl(m,n,i)));
                % Capacitance
                if ((R_P0(m,n,i)>=0) & (R_P1(m,n,i)>=0) &
(R_P1_lat(m,n,i)>=0) & (R_P2(m,n,i)>=0) & (R_P2_lat(m,n,i)>=0) &...
                (R_N0(m,n,i)>=0) & (R_N1(m,n,i)>=0) &
(R_N1_lat(m,n,i)>=0) & (R_N2(m,n,i)>=0) & (R_N2_lat(m,n,i)>=0) &
(R_N3(m,n,i)>=0))
                    C_1(m,n,i)=e_s/(w_depl_in(m,n,i)+w_in)*l_1p*t;
% Cap in the intrinsic region
                    C_2(m,n,i)=e_s/(w_depl(m,n,i))*l_2p*t;
% Capacitance in the T part lateral
                    C_3(m,n,i)=e_s/(w_depl(m,n,i))*w_2*t;
% Capacitance on the top of the T junction

tau(m,n,i)=C_1(m,n,i)*(R_P0(m,n,i)+R_N0(m,n,i)+R_P1(m,n,i)/2+R_N1(m,n,i
)/2+R_P1_lat(m,n,i)+R_N1_lat(m,n,i))+...

2*C_2(m,n,i)*(R_P0(m,n,i)+R_N0(m,n,i)+R_P1(m,n,i)+R_N1(m,n,i)+R_P2(m,n,
i)/2+R_N2(m,n,i)/2+R_P2_lat(m,n,i)+R_N2_lat(m,n,i))+...

C_3(m,n,i)*(R_P0(m,n,i)+2*R_N0(m,n,i)+R_P1(m,n,i)+2*R_N1(m,n,i)+R_P2(m,
n,i)+2*R_N2(m,n,i)+2*R_N3(m,n,i)/2);
                    f_th(m,n,i)=1/(2*pi*tau(m,n,i))*1/1e9;
                end
        end
        [a b c]=ind2sub(size(f_th),find(f_th==max(f_th(m,n,:))));
        V_max(m,n)=abs(V_th(c));
        f_max(m,n)=f_th(a,b,c);
    end
end

surf(N_D,N_A,V_max);
xlabel('N_D [cm^{-3}]');
ylabel('N_A [cm^{-3}]');
```

```
zlabel('Optimal Bias Voltage [V]');
```

6.1.2. MATLAB_Theory_Geometry_Optimization

```
Dinis Cheian
% Optimize bandwidth over geometry
% High-speed modulator in zero-change CMOS photonics Alloatti et. al.
% With Masetti's Model, used by Sentaurus
clear all
%cd('C:\Users\T5810\Dropbox
(MIT)\MATLAB\Modulator\Theory\New_Geometry')

%Constants
e_s=11.7*8.84e-14;          % [F/cm] epsilon of the silicon
q=1.6e-19;                  % [C] elementary charge
V_t=25.9e-3;                % [V] thermal voltage
n_i=1e10;                   % [cm^-3] intrinsic concentration of
carriers

l_0p= 0.62e-4;             % P region before the intrinsic portion
l_1p= 0.6e-4;              % P region along the intrinsic region
l_2p= 0.25e-4;             % P region on top of the intrinsic region

l_0n= 0.33e-4;              % N region before the intrinsic region
l_1n= l_1p;                 % same as l_1p but for N
l_2n= l_2p;                 % same as l_2p but for N
l_3n= 0.3e-4;               % N region on top of the P region
t=0.08e-4;                  % thikness of the silicon
%%
load w1_sim
load f_w1_sim
w_0= 0.18e-4;               % width of the P and N region before the
intrinsic region (is fixed by design rules/metal layout)
w_1= linspace(0.02e-4,0.8e-4,100);                  % width of the P and N
region where the intrinsic region is present
w_in=0.09e-4;               % width of the intrinsic region
w_2= w_in+w_1;               % width of the top T
N_A=2e17;
N_D=2e17;
V_th=-1;

for i=1:length(w_1)
                phi(i)=V_t*log(N_D*N_A/n_i^2);
% the build in potential
                % depletion regions with no intrinsic region
                w_n_depl(i)=sqrt(2*e_s*(phi(i)-
V_th)*N_A/(q*N_D*(N_A+N_D)));
                w_p_depl(i)=sqrt(2*e_s*(phi(i)-
V_th)*N_D/(q*N_A*(N_A+N_D)));
                w_depl(i)=w_n_depl(i)+w_p_depl(i);
                % depletion regions with intrinsic region
                w_n_depl_in(i)=(sqrt(w_in^2+2*e_s/q*(N_A+N_D)*(phi(i)-
V_th)/(N_A*N_D))-w_in)/(1+N_D/N_A);
                w_p_depl_in(i)=(sqrt(w_in^2+2*e_s/q*(N_A+N_D)*(phi(i)-
V_th)/(N_A*N_D))-w_in)/(1+N_A/N_D);
```

```
                w_depl_in(i)=w_n_depl_in(i)+w_p_depl_in(i);
                % P resistance
                R_P0(i)=resistivity('h',N_A)*l_0p*1/(t*w_0);     %
Resistance before the intrinsic region
                R_P1(i)=resistivity('h',N_A)*l_1p*1/(t*(w_1(i)-
2*w_p_depl_in(i)));  % Resistance along the intrinsic region
                R_P1_lat(i)=resistivity('h',N_A)*(w_1(i)/2-
w_p_depl_in(i))*1/(t*l_1p);  % Lateral resistance along the intrinsic
region
                R_P2(i)=resistivity('h',N_A)*(l_2p-
w_p_depl(i))*1/(t*(w_2(i)-2*w_p_depl(i))); % Resistance on top of the
intrinsic region
                R_P2_lat(i)=resistivity('h',N_A)*(w_2(i)/2-
w_p_depl(i))*1/(t*(l_2p-w_p_depl(i))); % Lateral resistance along the
intrinsic region
                % N resistance
                R_N0(i)=resistivity('e',N_D)*l_0n*1/(t*w_0);     %
Resistance before the intrinsic region
                R_N1(i)=resistivity('e',N_D)*l_1n*1/(t*(w_1(i)-
2*w_n_depl_in(i)));  % Resistance along the intrinsic region
                R_N1_lat(i)=resistivity('e',N_D)*(w_1(i)/2-
w_n_depl_in(i))*1/(t*l_1n);  % Lateral resistance along the intrinsic
region
                R_N2(i)=resistivity('e',N_D)*l_2n*1/(t*(w_2(i)-
2*w_n_depl(i))); % Resistance on top of the intrinsic region
                R_N2_lat(i)=resistivity('e',N_D)*(w_2(i)/2-
w_n_depl(i))*1/(t*l_2n); % Lateral resistance along the intrinsic
region
                R_N3(i)=resistivity('e',N_D)*l_3n*1/(t*(w_2(i)-
w_n_depl(i)));
                % Capacitance
                if ((R_P0(i)>=0) & (R_P1(i)>=0) & (R_P1_lat(i)>=0) &
(R_P2(i)>=0) & (R_P2_lat(i)>=0) &...
                (R_N0(i)>=0) & (R_N1(i)>=0) & (R_N1_lat(i)>=0) &
(R_N2(i)>=0) & (R_N2_lat(i)>=0) & (R_N3(i)>=0))
                    C_1(i)=e_s/(w_depl_in(i)+w_in)*l_1p*t;
% Cap in the intrinsic region
                    C_2(i)=e_s/(w_depl(i))*l_2p*t;
% Capacitance in the T part lateral
                    C_3(i)=e_s/(w_depl(i))*w_2(i)*t;
% Capacitance on the top of the T junction

tau(i)=C_1(i)*(R_P0(i)+R_N0(i)+R_P1(i)/2+R_N1(i)/2+R_P1_lat(i)+R_N1_lat
(i))+...

2*C_2(i)*(R_P0(i)+R_N0(i)+R_P1(i)+R_N1(i)+R_P2(i)/2+R_N2(i)/2+R_P2_lat(
i)+R_N2_lat(i))+...

C_3(i)*(R_P0(i)+2*R_N0(i)+R_P1(i)+2*R_N1(i)+R_P2(i)+2*R_N2(i)+2*R_N3(i)
/2);
                    f_th(i)=1/(2*pi*tau(i))*1/1e9;
                end
end
```

```
%% Optimize over w_int
load win_sim
load f_win_sim
w_0= 0.18e-4;               % width of the P and N region before the
intrinsic region (is fixed by design rules/metal layout)
w_1= 0.46e-4;               % width of the P and N region where the
intrinsic region is present
w_in=linspace(0.01e-4,0.3e-4,101);               % width of the
intrinsic region
w_2= w_in+w_1;               % width of the top T
N_A=2e17;
N_D=2e17;
V_th=-1;


for i=1:length(w_in)
                phi(i)=V_t*log(N_D*N_A/n_i^2);
% the build in potential
                % depletion regions with no intrinsic region
                w_n_depl(i)=sqrt(2*e_s*(phi(i)-
V_th)*N_A/(q*N_D*(N_A+N_D)));
                w_p_depl(i)=sqrt(2*e_s*(phi(i)-
V_th)*N_D/(q*N_A*(N_A+N_D)));
                w_depl(i)=w_n_depl(i)+w_p_depl(i);
                % depletion regions with intrinsic region

w_n_depl_in(i)=(sqrt(w_in(i)^2+2*e_s/q*(N_A+N_D)*(phi(i)-
V_th)/(N_A*N_D))-w_in(i))/(1+N_D/N_A);

w_p_depl_in(i)=(sqrt(w_in(i)^2+2*e_s/q*(N_A+N_D)*(phi(i)-
V_th)/(N_A*N_D))-w_in(i))/(1+N_A/N_D);
                w_depl_in(i)=w_n_depl_in(i)+w_p_depl_in(i);
                % P resistance
                R_P0(i)=resistivity('h',N_A)*l_0p*1/(t*w_0);     %
Resistance before the intrinsic region
                R_P1(i)=resistivity('h',N_A)*l_1p*1/(t*(w_1-
2*w_p_depl_in(i)));  % Resistance along the intrinsic region
                R_P1_lat(i)=resistivity('h',N_A)*(w_1/2-
w_p_depl_in(i))*1/(t*l_1p);  % Lateral resistance along the intrinsic
region
                R_P2(i)=resistivity('h',N_A)*(l_2p-
w_p_depl(i))*1/(t*(w_2(i)-2*w_p_depl(i))); % Resistance on top of the
intrinsic region
                R_P2_lat(i)=resistivity('h',N_A)*(w_2(i)/2-
w_p_depl(i))*1/(t*(l_2p-w_p_depl(i))); % Lateral resistance along the
intrinsic region
                % N resistance
                R_N0(i)=resistivity('e',N_D)*l_0n*1/(t*w_0);     %
Resistance before the intrinsic region
                R_N1(i)=resistivity('e',N_D)*l_1n*1/(t*(w_1-
2*w_n_depl_in(i)));  % Resistance along the intrinsic region
                R_N1_lat(i)=resistivity('e',N_D)*(w_1/2-
w_n_depl_in(i))*1/(t*l_1n);  % Lateral resistance along the intrinsic
region
                R_N2(i)=resistivity('e',N_D)*l_2n*1/(t*(w_2(i)-
2*w_n_depl(i))); % Resistance on top of the intrinsic region
```

```
                R_N2_lat(i)=resistivity('e',N_D)*(w_2(i)/2-
w_n_depl(i))*1/(t*l_2n); % Lateral resistance along the intrinsic
region
                R_N3(i)=resistivity('e',N_D)*l_3n*1/(t*(w_2(i)-
w_n_depl(i)));
                % Capacitance
                if ((R_P0(i)>=0) & (R_P1(i)>=0) & (R_P1_lat(i)>=0) &
(R_P2(i)>=0) & (R_P2_lat(i)>=0) &...
                (R_N0(i)>=0) & (R_N1(i)>=0) & (R_N1_lat(i)>=0) &
(R_N2(i)>=0) & (R_N2_lat(i)>=0) & (R_N3(i)>=0))
                    C_1(i)=e_s/(w_depl_in(i)+w_in(i))*l_1p*t;
% Cap in the intrinsic region
                    C_2(i)=e_s/(w_depl(i))*l_2p*t;
% Capacitance in the T part lateral
                    C_3(i)=e_s/(w_depl(i))*w_2(i)*t;
% Capacitance on the top of the T junction

tau_1(i)=C_1(i)*(R_P0(i)+R_N0(i)+R_P1(i)/2+R_N1(i)/2+R_P1_lat(i)+R_N1_l
at(i));

tau(i)=C_1(i)*(R_P0(i)+R_N0(i)+R_P1(i)/2+R_N1(i)/2+R_P1_lat(i)+R_N1_lat
(i))+...

2*C_2(i)*(R_P0(i)+R_N0(i)+R_P1(i)+R_N1(i)+R_P2(i)/2+R_N2(i)/2+R_P2_lat(
i)+R_N2_lat(i))+...

C_3(i)*(R_P0(i)+2*R_N0(i)+R_P1(i)+2*R_N1(i)+R_P2(i)+2*R_N2(i)+2*R_N3(i)
/2);
                    f_th(i)=1/(2*pi*tau(i))*1/1e9;
                end
end

plot(w_in/1e-4,f_th,'LineWidth',1.5);
%xlim([win_sim(1) win_sim(end)]);
xlabel('Width of the Intrinsic Region, w_{i} [\mum]','fontsize',15);
ylabel('Bandwidth [GHz]','fontsize',15);
grid on


%% Optimize over w_1 and w_int
w_0= 0.18e-4;               % width of the P and N region before the
intrinsic region (is fixed by design rules/metal layout)
w_1= linspace(0.1e-4,0.6e-4,100);               % width of the P and N
region where the intrinsic region is present
w_in=linspace(0.01e-4,0.2e-4,101);               % width of the
intrinsic region
%w_2= w_in+w_1;               % width of the top T
N_A=1e18;
N_D=1e18;
V_th=-1;

for i=1:length(w_1)
    %i
    for j=1:length(w_in)
                phi(i,j)=V_t*log(N_D*N_A/n_i^2);
% the build in potential
```

```
                % depletion regions with no intrinsic region
                w_n_depl(i,j)=sqrt(2*e_s*(phi(i,j)-
V_th)*N_A/(q*N_D*(N_A+N_D)));
                w_p_depl(i,j)=sqrt(2*e_s*(phi(i,j)-
V_th)*N_D/(q*N_A*(N_A+N_D)));
                w_depl(i,j)=w_n_depl(i,j)+w_p_depl(i,j);
                % depletion regions with intrinsic region

w_n_depl_in(i,j)=(sqrt(w_in(j)^2+2*e_s/q*(N_A+N_D)*(phi(i,j)-
V_th)/(N_A*N_D))-w_in(j))/(1+N_D/N_A);

w_p_depl_in(i,j)=(sqrt(w_in(j)^2+2*e_s/q*(N_A+N_D)*(phi(i,j)-
V_th)/(N_A*N_D))-w_in(j))/(1+N_A/N_D);
                w_depl_in(i,j)=w_n_depl_in(i,j)+w_p_depl_in(i,j);
                % P resistance
                R_P0(i,j)=resistivity('h',N_A)*l_0p*1/(t*w_0);     %
Resistance before the intrinsic region
                R_P1(i,j)=resistivity('h',N_A)*l_1p*1/(t*(w_1(i)-
2*w_p_depl_in(i,j)));  % Resistance along the intrinsic region
                R_P1_lat(i,j)=resistivity('h',N_A)*(w_1(i)/2-
w_p_depl_in(i,j))*1/(t*l_1p);  % Lateral resistance along the intrinsic
region
                R_P2(i,j)=resistivity('h',N_A)*(l_2p-
w_p_depl(i,j))*1/(t*((w_1(i)+w_in(j))-2*w_p_depl(i,j))); % Resistance
on top of the intrinsic region
                R_P2_lat(i,j)=resistivity('h',N_A)*((w_1(i)+w_in(j))/2-
w_p_depl(i,j))*1/(t*(l_2p-w_p_depl(i,j))); % Lateral resistance along
the intrinsic region
                % N resistance
                R_N0(i,j)=resistivity('e',N_D)*l_0n*1/(t*w_0);     %
Resistance before the intrinsic region
                R_N1(i,j)=resistivity('e',N_D)*l_1n*1/(t*(w_1(i)-
2*w_n_depl_in(i,j)));  % Resistance along the intrinsic region
                R_N1_lat(i,j)=resistivity('e',N_D)*(w_1(i)/2-
w_n_depl_in(i,j))*1/(t*l_1n);  % Lateral resistance along the intrinsic
region

R_N2(i,j)=resistivity('e',N_D)*l_2n*1/(t*((w_1(i)+w_in(j))-
2*w_n_depl(i,j))); % Resistance on top of the intrinsic region
                R_N2_lat(i,j)=resistivity('e',N_D)*((w_1(i)+w_in(j))/2-
w_n_depl(i,j))*1/(t*l_2n); % Lateral resistance along the intrinsic
region

R_N3(i,j)=resistivity('e',N_D)*l_3n*1/(t*((w_1(i)+w_in(j))-
w_n_depl(i,j)));
                % Capacitance
                if ((R_P0(i,j)>=0) & (R_P1(i,j)>=0) &
(R_P1_lat(i,j)>=0) & (R_P2(i,j)>=0) & (R_P2_lat(i,j)>=0) &...
                (R_N0(i,j)>=0) & (R_N1(i,j)>=0) & (R_N1_lat(i,j)>=0) &
(R_N2(i,j)>=0) & (R_N2_lat(i,j)>=0) & (R_N3(i,j)>=0))
                    C_1(i,j)=e_s/(w_depl_in(i,j)+w_in(j))*l_1p*t;
% Cap in the intrinsic region
                    C_2(i,j)=e_s/(w_depl(i,j))*l_2p*t;
% Capacitance in the T part lateral
                    C_3(i,j)=e_s/(w_depl(i,j))*(w_1(i)+w_in(j))*t;
% Capacitance on the top of the T junction
```

```
tau(i,j)=C_1(i,j)*(R_P0(i,j)+R_N0(i,j)+R_P1(i,j)/2+R_N1(i,j)/2+R_P1_lat
(i,j)+R_N1_lat(i,j))+...

2*C_2(i,j)*(R_P0(i,j)+R_N0(i,j)+R_P1(i,j)+R_N1(i,j)+R_P2(i,j)/2+R_N2(i,
j)/2+R_P2_lat(i,j)+R_N2_lat(i,j))+...

C_3(i,j)*(R_P0(i,j)+2*R_N0(i,j)+R_P1(i,j)+2*R_N1(i,j)+R_P2(i,j)+2*R_N2(
i,j)+2*R_N3(i,j)/2);
                    f_th(i,j)=1/(2*pi*tau(i,j))*1/1e9;
                end
    end
end
```

6.1.3. MATLAB_Energy_Check

```
function [E_True]=E_Check(C,V,w);
    E_junction=C*V^2/2;                         % compute energy for
one junction
    E_total=2*pi*3.82e-4/(2*w)*E_junction;      % compute total energy
of all junctions
    E_True=1*(E_total<40e-15);                  % check if it exceeds
40fJ/bit
end
```

6.1.4. MATLAB_ER_Check

```
function [ER_True]=ER_Check(C,w);
    ER_total=2*pi*3.82e-4/(2*w)*C;      % compute total energy of all
junctions
    ER_True=1*(ER_total>3.2e-17*30);                  % check if it
exceeds 40fJ/bit
end
```

6.1.5. MATLAB_IL_Check

```
function [IL_true]=IL_Check(N_A,N_D)
    alpha_0=42;                     % cm^-1
http://www.cleanroom.byu.edu/OpticalCalc.phtml
    alpha_n=2.88e-18;              % from "Free Carrier Absorption in
Silicon" Schroder et al. (3),(4)
    alpha_p=2.16e-18;              % assuming Lambda=1.2um
    alpha=(alpha_0+alpha_n*N_D+alpha_p*N_A)*2*pi*3.8e-4; % average
radius in the center of the beam 3.82um
    IL=10*log10(exp(-alpha));  % compute the IL
    IL_true=1*(IL>-1);
end
```

6.1.6. MATLAB_Resistivity

```
function [rho]=resistivity(carrier, N)
    % Define the parameters for the Masetti Model
    % as in sdevice_ug on page 348
    q=1.6e-19;
    mumin1=[52.2,44.9];
    mumin2=[52.2,0];
```

```
    mu1=[43.4,29.0];
    Pc=[0,9.23e16];
    Cr=[9.68e16,2.23e17];
    Cs=[3.43e20,6.10e20];
    alpha=[0.680,0.719];
    beta=[2.0,2.0];
    % determine if its electron or hole
    c=1*(carrier=='e')+2*(carrier=='h');
    % find mu_const
    T=300;
    mumax=[1417,470.5];
    exponent=[2.5,2.2];
    mu_const=mumax(c)*(T/300)^(-exponent(c));
    % compute the resistivity
    mu=mumin1(c)*exp(-Pc(c)/N)+...
         (mu_const-mumin2(c))/(1+(N/Cr(c))^alpha(c))-...
        mu1(c)/(1+(Cs(c)/N)^beta(c));
    rho=1/(q*mu*N);
end
```

6.1.7. MATLAB_Sentaurus_Data_Analysis

```
% Dinis Cheian
% Analyze the Modulator Sentaurus results
clear all
cd('C:\Users\T5810\Dropbox (MIT)\MATLAB\Modulator\Simulations')
% First set of data

% First set of data
M=csvread('data.txt');      % read out the whole file
M=transpose(M);

%%
s=size(M);                   % determine the size for usage in the loop
f_win_sim=zeros(1,s(2)/2);          % create array where the 3dB
frequencies will be stored
win_sim=linspace(0.42,0.7,15);  % deduce the voltage range, based that
we start at -0.1 and increase by 0.1
for i=1:s(2)/2
    i
    M_local=M(:,2*i);        % store a local value of the current
response
    t_local=M(:,2*i-1);      % store a local value of time
    index=find(t_local==1.1e-13);  % find the point when the voltage is
shifter
    M_new(:,2*i-1)=t_local(index:s(1));             % and the time
    M_new(:,2*i)=(M_local(index:s(1))-M_local(s(1)))/(M_local(index)-
M_local(s(1))); % Cut the vector at where it starts to decay
    [y(:,i),x(:,i)]=take_fft(M_new(:,2*i-1),M_new(:,2*i));      % take
the fft
    y(:,i)=y(:,i)/y(1,i);                           % scale the fft
    y(:,i)=20*log10(y(:,i));                        % compute fft in dB
    X=x(:,i);                                       % prepare for model
of fft
    X=X(1:20);                                      % prepare for model
    Y=y(:,i);                                       % prepare for model
```

```
    Y=Y(1:20);                                      % prepare for model
    Model=fit(Y,X,'smoothingspline');               % create the model
    f_win_sim(i)=feval(Model,-3)/1e9;                 % find the 3dB
frequency
end
```

6.1.8. MATLAB_Take_FFT

```
function [FFT,f]=take_fft(time,data)
    Fs=length(time)/time(end);      % Sampling Frequency
    Y=fft(data);
    L=length(data);
    P2=abs(Y/L);
    P1=P2(1:L/2+1);
    P1(2:end-1)=2*P1(2:end-1);
    f=Fs*(0:(L/2))/L;
    f=f(2:end);
    FFT=P1(2:end);
end
```

6.1.9. MATLAB_Experiment_Data_Analysis

```
% Dinis Cheian
% Determine 3dB frequency of the modulator
%% Back to back and detector S21
clear all
cd('C:\Users\T5810\Dropbox (MIT)\MATLAB\Modulator\Experiment')
S21_bb=dlmread('back_to_back.txt');
f_bb=S21_bb(:,1);
S21_bb=S21_bb(:,4);
S21_bb=20*log10(S21_bb/max(S21_bb));
S21_bb=fit(f_bb,S21_bb,'smoothingspline');
f_bb=linspace(0.05,20,401);
S21_bb=feval(S21_bb,f_bb);

S21_det=dlmread('PD_2010_DataSheet_Response.txt');
f_det=S21_det(:,1);
S21_det=S21_det(:,2);
S21_det=fit(f_det,S21_det,'smoothingspline');
f_det=f_bb;
S21_det=feval(S21_det,f_det);

%% Modulator 4, Load the Data
f_exp_2=zeros(1,20);
V_exp_2=linspace(0,-2,20);
for i=12
    i
    % Load data
    file=int2str(i);
    file=strcat('230_4/',file,'.txt');
    data=dlmread(file);
    f_local=data(:,1);
    S21_local=data(:,4);
    % scale to dB and subtract back to back and detector
    S21_local=20*log10(S21_local/mean(S21_local(1:10)));
    S21_local=S21_local-S21_bb-S21_det;
```

```
    S21_local=S21_local-mean(S21_local(1:10));
    %f_local=f_local(10:end);
    %S21_local=S21_local(10:end);
    % build a model using power fit
    model=fit(f_local,S21_local,'power2');
    S21_local_model=feval(model,f_local);
    index=find(S21_local_model<S21_local_model(1)-3);
    f_exp_2(i)=f_local(index(1));
    f_4(:,i)=f_local;
    S21_4(:,i)=S21_local;
end
```

6.1.10. SENTAURUS_Draw_T_Junction

```
; Draw the Structure

; P regions

(sdegeo:create-rectangle (position -0.09 -0.62 0)     (position 0.09 0 0) "Silicon" "P_0")

(sdegeo:create-rectangle (position -0.175 0 0)             (position 0.175 0.6 0)
"Silicon" "P_1")

(sdegeo:create-rectangle (position -0.22 0.6 0)      (position 0.22 0.85 0) "Silicon"
"P_2")

; N regions

(sdegeo:create-rectangle (position -0.35 -0.33 0)     (position -0.44 0 0) "Silicon"
"N_0_1")

(sdegeo:create-rectangle (position -0.265 0 0)             (position -0.44 0.6 0)
"Silicon" "N_1_1")

(sdegeo:create-rectangle (position -0.22 0.6 0)      (position -0.44 0.85 0) "Silicon"
"N_2_1")


(sdegeo:create-rectangle (position 0.35 -0.33 0)     (position 0.44 0 0) "Silicon"
"N_0_2")

(sdegeo:create-rectangle (position 0.265 0 0)             (position 0.44 0.6 0)
"Silicon" "N_1_2")

(sdegeo:create-rectangle (position 0.22 0.6 0)             (position 0.44 0.85 0)
"Silicon" "N_2_2")

(sdegeo:create-rectangle (position 0.44 0.85 0)      (position -0.44 1.15 0) "Silicon"
"N_up")
```

```
; The contacts
(sdegeo:create-rectangle (position -0.07 -0.76 0)		(position  0.07 -0.62 0)
"Aluminum" "Cathode")
(sdegeo:create-rectangle (position -0.37 -0.47 0)		(position -0.44 -0.33 0)
"Aluminum" "Anode_1")
(sdegeo:create-rectangle (position  0.37 -0.47 0)		(position  0.44 -0.33 0)
"Aluminum" "Anode_2")


; The intrinsic regions
(sdegeo:create-rectangle (position -0.175 0 0)		(position -0.265 0.6 0) "Silicon"
"Int_1")
(sdegeo:create-rectangle (position  0.175 0 0)		(position  0.265 0.6 0) "Silicon"
"Int_2")


; Assign the metal contacts
(sdegeo:define-contact-set "Anode_contact" 4  (color:rgb 0 0 1 ) "##")
(sdegeo:define-contact-set "Cathode_contact" 4  (color:rgb 0 1 0 ) "##")


(sdegeo:set-contact-boundary-edges (list (car (find-body-id (position -0.01 -0.64 0))))
"Cathode_contact")
(sdegeo:set-contact-boundary-edges (list (car (find-body-id (position -0.43 -0.35 0))))
"Anode_contact")
(sdegeo:set-contact-boundary-edges (list (car (find-body-id (position  0.43 -0.35 0))))
"Anode_contact")


; Dope the Silicon
; P Regions
(sdedr:define-constant-profile "P_doping" "BoronActiveConcentration" 9.4e16)
(sdedr:define-constant-profile-region "Dope_P_1" "P_doping" "P_0")
(sdedr:define-constant-profile-region "Dope_P_2" "P_doping" "P_1")
(sdedr:define-constant-profile-region "Dope_P_3" "P_doping" "P_2")
```

```
; N Regions
(sdedr:define-constant-profile "N_doping" "ArsenicActiveConcentration" 7.6e16)
(sdedr:define-constant-profile-region "Dope_N_1" "N_doping" "N_0_1")
(sdedr:define-constant-profile-region "Dope_N_2" "N_doping" "N_0_2")
(sdedr:define-constant-profile-region "Dope_N_3" "N_doping" "N_1_1")
(sdedr:define-constant-profile-region "Dope_N_4" "N_doping" "N_1_2")
(sdedr:define-constant-profile-region "Dope_N_5" "N_doping" "N_2_1")
(sdedr:define-constant-profile-region "Dope_N_6" "N_doping" "N_2_2")
(sdedr:define-constant-profile-region "Dope_N_up" "N_doping" "N_up")


; Define the Mesh
(sdedr:define-refeval-window "Cover_all_Window" "Rectangle"  (position 0.44 -0.76 0)
(position -0.44 1.15 0))
(sdedr:define-refinement-size "Typical_Size" 0.01 0.01 0.01 0.001 0.001 0.001 )
(sdedr:define-refinement-placement "General_Mesh" "Typical_Size" (list "window"
"Cover_all_Window" ) )
```

6.1.11. SENTAURUS_Vary_w_spoke

```
; Draw the Structure
; P regions
(sde:define-parameter "w" 0.42)
(sde:define-parameter "w_half" (/ w 2))
(sde:define-parameter "w_half_neg" (* w_half -1))
(sde:define-parameter "w_p2" (+ w_half 0.045))
(sde:define-parameter "w_p2_neg" (* w_p2 -1))
(sde:define-parameter "w_n0" (+ w 0.09))
(sde:define-parameter "w_n0_neg" (* w_n0 -1))
(sde:define-parameter "w_n0_1" (+ w_n0_neg 0.09))
(sde:define-parameter "w_n0_1_neg" (* w_n0_1 -1))
```

```
(sde:define-parameter "w_n1" (- w_n0 w_half))
(sde:define-parameter "w_n1_neg" (* w_n1 -1))
(sde:define-parameter "w_an1" (- w_n0 0.07))
(sde:define-parameter "w_an2" (* w_an1 -1))

(sdegeo:create-rectangle (position -0.09 -0.62 0)      (position 0.09 0 0) "Silicon" "P_0")
(sdegeo:create-rectangle (position w_half_neg 0 0)  (position w_half 0.6 0) "Silicon"
"P_1")
(sdegeo:create-rectangle (position w_p2_neg 0.6 0)  (position w_p2 0.85 0) "Silicon"
"P_2")
; N regions
(sdegeo:create-rectangle (position w_n0_1 -0.33 0)  (position w_n0_neg 0 0) "Silicon"
"N_0_1")
(sdegeo:create-rectangle (position w_n1_neg 0 0)              (position w_n0_neg 0.6 0)
"Silicon" "N_1_1")
(sdegeo:create-rectangle (position w_p2_neg 0.6 0)  (position w_n0_neg 0.85 0) "Silicon"
"N_2_1")


(sdegeo:create-rectangle (position w_n0_1_neg -0.33 0)      (position w_n0 0 0) "Silicon"
"N_0_2")
(sdegeo:create-rectangle (position w_n1 0 0)                    (position w_n0 0.6 0)
"Silicon" "N_1_2")
(sdegeo:create-rectangle (position w_p2 0.6 0)                  (position w_n0 0.85 0)
"Silicon" "N_2_2")
(sdegeo:create-rectangle (position w_n0 0.85 0)       (position w_n0_neg 1.15 0) "Silicon"
"N_up")


; The contacts
(sdegeo:create-rectangle (position -0.07 -0.76 0)               (position  0.07 -0.62 0)
"Aluminum" "Cathode")
(sdegeo:create-rectangle (position  w_an2 -0.47 0)              (position  w_n0_neg -0.33 0)
"Aluminum" "Anode_1")
```

```
(sdegeo:create-rectangle (position  w_an1 -0.47 0)            (position  w_n0 -0.33 0) "Aluminum" "Anode_2")


; The intrinsic regions

(sdegeo:create-rectangle (position w_half_neg 0 0)  (position w_n1_neg 0.6 0) "Silicon" "Int_1")

(sdegeo:create-rectangle (position w_half 0 0)         (position  w_n1 0.6 0) "Silicon" "Int_2")


; Assign the metal contacts

(sdegeo:define-contact-set "Anode_contact" 4  (color:rgb 0 0 1 ) "##")

(sdegeo:define-contact-set "Cathode_contact" 4  (color:rgb 0 1 0 ) "##")

(sdegeo:set-contact-boundary-edges (list (car (find-body-id (position -0.01 -0.64 0)))) "Cathode_contact")

(sdegeo:set-contact-boundary-edges (list (car (find-body-id (position w_an2 -0.47 0)))) "Anode_contact")

(sdegeo:set-contact-boundary-edges (list (car (find-body-id (position w_an1 -0.47 0)))) "Anode_contact")


; Dope the Silicon

; P Regions

(sdedr:define-constant-profile "P_doping" "BoronActiveConcentration" 9.4e16)

(sdedr:define-constant-profile-region "Dope_P_1" "P_doping" "P_0")

(sdedr:define-constant-profile-region "Dope_P_2" "P_doping" "P_1")

(sdedr:define-constant-profile-region "Dope_P_3" "P_doping" "P_2")


; N Regions

(sdedr:define-constant-profile "N_doping" "ArsenicActiveConcentration" 7.6e16)

(sdedr:define-constant-profile-region "Dope_N_1" "N_doping" "N_0_1")

(sdedr:define-constant-profile-region "Dope_N_2" "N_doping" "N_0_2")
```

```
(sdedr:define-constant-profile-region "Dope_N_3" "N_doping" "N_1_1")
(sdedr:define-constant-profile-region "Dope_N_4" "N_doping" "N_1_2")
(sdedr:define-constant-profile-region "Dope_N_5" "N_doping" "N_2_1")
(sdedr:define-constant-profile-region "Dope_N_6" "N_doping" "N_2_2")
(sdedr:define-constant-profile-region "Dope_N_up" "N_doping" "N_up")


; Define the Mesh
(sdedr:define-refeval-window "Cover_all_Window" "Rectangle"  (position w_n0 -0.76 0)
(position w_n0_neg 1.15 0))
(sdedr:define-refinement-size "Typical_Size" 0.01 0.01 0.01 0.001 0.001 0.001 )
(sdedr:define-refinement-placement "General_Mesh" "Typical_Size" (list "window"
"Cover_all_Window" ) )


(sde:save-model "modulator")
(sdeio:save-dfise-bnd (get-body-list) "modulator.bnd")


(sde:set-meshing-command "snmesh -a -c boxmethod")
(sdedr:append-cmd-file "")
(sde:build-mesh "snmesh" "-a -c boxmethod" "./modulator")
```

6.1.12. SENTAURUS_Vary_w_intrinsic

```
; Draw the Structure
; P regions
(sde:define-parameter "w_in" 0.3)
(sde:define-parameter "w_in_half" (/ w_in 2))
(sde:define-parameter "w_p1" (+ w_in_half 0.21))
(sde:define-parameter "w_p1_neg" (/ w_p1 -1))
(sde:define-parameter "w_int1_neg" (- -0.21 w_in))
(sde:define-parameter "w_int1" (/ w_int1_neg -1))
```

```
(sde:define-parameter "w_up" (+ w_int1 0.21))

(sde:define-parameter "w_down" (- w_int1_neg 0.21))

(sde:define-parameter "w_an1" (- w_up 0.07))

(sde:define-parameter "w_an2" (+ w_down 0.07))

(sde:define-parameter "w_n0_1" (+ w_down 0.09))

(sde:define-parameter "w_n0_2" (- w_up 0.09))


(sdegeo:create-rectangle (position -0.09 -0.62 0)      (position 0.09 0 0) "Silicon" "P_0")

(sdegeo:create-rectangle (position -0.21 0 0)          (position 0.21 0.6 0) "Silicon" "P_1")

(sdegeo:create-rectangle (position w_p1_neg 0.6 0)  (position w_p1 0.85 0) "Silicon"
"P_2")

; N regions

(sdegeo:create-rectangle (position w_n0_1 -0.33 0)  (position w_down 0 0) "Silicon"
"N_0_1")

(sdegeo:create-rectangle (position w_int1_neg 0 0)             (position w_down 0.6 0)
"Silicon" "N_1_1")

(sdegeo:create-rectangle (position w_p1_neg 0.6 0)  (position w_down 0.85 0) "Silicon"
"N_2_1")


(sdegeo:create-rectangle (position w_n0_2 -0.33 0)  (position w_up 0 0) "Silicon"
"N_0_2")

(sdegeo:create-rectangle (position w_int1 0 0)                 (position w_up 0.6 0)
"Silicon" "N_1_2")

(sdegeo:create-rectangle (position w_p1 0.6 0)                 (position w_up 0.85 0)
"Silicon" "N_2_2")

(sdegeo:create-rectangle (position w_up 0.85 0)       (position w_down 1.15 0) "Silicon"
"N_up")


; The contacts

(sdegeo:create-rectangle (position -0.07 -0.76 0)              (position  0.07 -0.62 0)
"Aluminum" "Cathode")
```

```
(sdegeo:create-rectangle (position  w_an2 -0.47 0)		(position w_down -0.33 0) "Aluminum" "Anode_1")
(sdegeo:create-rectangle (position  w_an1 -0.47 0)		(position  w_up -0.33 0) "Aluminum" "Anode_2")


; The intrinsic regions
(sdegeo:create-rectangle (position -0.21 0 0) (position  w_int1_neg 0.6 0) "Silicon" "Int_1")
(sdegeo:create-rectangle (position  0.21 0 0) (position  w_int1 0.6 0) "Silicon" "Int_2")


; Assign the metal contacts
(sdegeo:define-contact-set "Anode_contact" 4  (color:rgb 0 0 1 ) "##")
(sdegeo:define-contact-set "Cathode_contact" 4  (color:rgb 0 1 0 ) "##")


(sdegeo:set-contact-boundary-edges (list (car (find-body-id (position -0.01 -0.64 0)))) "Cathode_contact")
(sdegeo:set-contact-boundary-edges (list (car (find-body-id (position w_an2 -0.47 0)))) "Anode_contact")
(sdegeo:set-contact-boundary-edges (list (car (find-body-id (position w_an1 -0.47 0)))) "Anode_contact")


; Dope the Silicon
; P Regions
(sdedr:define-constant-profile "P_doping" "BoronActiveConcentration" 9.4e16)
(sdedr:define-constant-profile-region "Dope_P_1" "P_doping" "P_0")
(sdedr:define-constant-profile-region "Dope_P_2" "P_doping" "P_1")
(sdedr:define-constant-profile-region "Dope_P_3" "P_doping" "P_2")


; N Regions
(sdedr:define-constant-profile "N_doping" "ArsenicActiveConcentration" 7.6e16)
```

```
(sdedr:define-constant-profile-region "Dope_N_1" "N_doping" "N_0_1")
(sdedr:define-constant-profile-region "Dope_N_2" "N_doping" "N_0_2")
(sdedr:define-constant-profile-region "Dope_N_3" "N_doping" "N_1_1")
(sdedr:define-constant-profile-region "Dope_N_4" "N_doping" "N_1_2")
(sdedr:define-constant-profile-region "Dope_N_5" "N_doping" "N_2_1")
(sdedr:define-constant-profile-region "Dope_N_6" "N_doping" "N_2_2")
(sdedr:define-constant-profile-region "Dope_N_up" "N_doping" "N_up")

; Define the Mesh
(sdedr:define-refeval-window "Cover_all_Window" "Rectangle"  (position w_up -0.76 0) (position w_down 1.15 0))
(sdedr:define-refinement-size "Typical_Size" 0.01 0.01 0.01 0.001 0.001 0.001 )
(sdedr:define-refinement-placement "General_Mesh" "Typical_Size" (list "window" "Cover_all_Window" ) )

(sde:save-model "modulator")
(sdeio:save-dfise-bnd (get-body-list) "modulator.bnd")

(sde:set-meshing-command "snmesh -a -c boxmethod")
(sdedr:append-cmd-file "")
(sde:build-mesh "snmesh" "-a -c boxmethod" "./modulator")
```

6.1.13. SENTAURUS_Modulator

```
File {
        * Input Files
        Grid="modulator_msh.tdr"

        * Output Files
        Current="modulator_des.plt"
```

```
	Plot="modulator_des.tdr"
	Output="modulator_des.log"
}

Electrode {
	{Name="Anode_contact" Voltage=0.0}
	{Name="Cathode_contact" Voltage=(-1.0 at 1e-13, -1.00001 at 1.1e-13) }
}
Physics {
	Mobility(DopingDep HighFieldSat Enormal)
	EffectiveIntrinsicDensity(OldSlotBoom)
}

Plot {
	eDensity hDensity
	eCurrent hCurrent
	eQuasiFermi hQuasiFermi
	eTemperature
	ElectricField eEparallel hEparallel
	Potential SpaceCharge
	SRHRecombination Auger AvalancheGeneration
	eMobility hMobility eVelocity hVelocity
	Doping DonorConcentration AcceptorConcentration
}

Math{
	PeriodicBC(
		(Direction=0
```

```
                 Coordinates=(-0.72 0.72)
                )
        )
        Extrapolate
        Transient=BE
        Iterations=10
        Notdamped=100
        RhsMin=1e-20
        RhsMax=1e+40
}

Solve {
        Coupled(Iterations=300){Poisson}
        Coupled(Iterations=300){Electron}
        Coupled(Iterations=300){Hole}
        Coupled(Iterations=300){Poisson Electron Hole}
        Transient(InitialTime=0 FinalTime=5e-10
                Initialstep=5e-15 Increment=1.1 Decrement=1.2
                 Maxstep=1e-13 Minstep=1e-16)
                {Coupled{Poisson Electron Hole}
                Plot ( Time=(0; 1.1e-13; 2e-13; 1e-12; 2e-12; 3e-12; 4e-12; 5e-12; 6e-12; 7e-12; 8e-12; 9e-12; 1e-11) NoOverwrite)}
}

CurrentPlot {
eDensity(Integrate(Region=N_2_1))
eDensity(Integrate(Region=N_2_2))
eDensity(Integrate(Region=N_up))
hDensity(Integrate(Region=P_2))
```

```
}
```

6.1.14. SVISUAL_Extract_Data

```
load_file /homes/dcheian/sentaurus/simulation/Modulator/Best/modulator_des.plt


create_plot -1d

select_plots Plot_1

create_curve -plot Plot_1 -dataset modulator_des -axisX time -axisY {IntegrP_3 hDensity}


set I_01 [get_curve_data Curve_1 -plot Plot_1 -axisY]

set t_01 [get_curve_data Curve_1 -plot Plot_1 -axisX]


set fp [open "data_one.txt" "w"]

puts $fp $t_01

puts $fp $I_01

close $fp
```

6.2. Detector

6.2.1. MATLAB_Optical_Simulation_Data_Analysis

```
% Dinis Cheian
% analysis of Detector bandwidth with laser power
%% SiGe Load all the Data
clear all
cd('C:\Users\T5810\Dropbox (MIT)\MATLAB\Detector\Bandwidth and Laser Power')

I0=csvread('data_opt.txt');     % read out the whole file
I0=transpose(I0);
[a b]=ind2sub(size(I0),find(I0==0));    % search for the 0 entries
a=sort(a);                              % sort a
index_0=find(a>5,1);                    % find where the 0 rows start
zero_pos=a(index_0)-1;                    % find where the 0 rows start
if (length(zero_pos)~=0)
    I0=I0(1:zero_pos,:);
end
```

6.2.2. MATLAB_Electrical_Simulation_Data_Analysis

```
% Dinis Cheian
% analysis of Detector bandwidth with laser power
%% SiGe Load all the Data
clear all
cd('C:\Users\T5810\Dropbox (MIT)\MATLAB\Detector\Bandwidth and Laser
Power')

I0=csvread('data_elec.txt');     % read out the whole file
I0=transpose(I0);
[a b]=ind2sub(size(I0),find(I0==0));    % search for the 0 entries
a=sort(a);                              % sort a
index_0=find(a>5,1);                    % find where the 0 rows start
zero_pos=a(index_0)-1;                    % find where the 0 rows start
if (length(zero_pos)~=0)
    I0=I0(1:zero_pos,:);
end

%%
e_s=11.7*8.84e-14;          % permeability of silicon
v_sat=1e7;                  % saturation velocity of silicon
A=0.2e-4*80e-7;             % area of interaction
for j=1:6
    x=I0(:,2*j-1);          % time vector
    y=I0(:,2*j);            % current vector
    y=y-y(end);             % small signal current, subtract DC current
    y(1)=y(2);              % get rid of turn on current
    index=find(y==max(y),1);% find maximum of current
    R(j)=1e-5/y(index);     % compute R=V_small/I
    Q(j)=trapz(x,y);        % compute the charge as Q=int Idt
    C(j)=Q(j)/1e-5;         % compute capacitance as C=Q/V_small
    f_RC(j)=1/(2*pi*R(j)*C(j))*1/1e9;   % compute frequency due to RC
as f=1/(2pi*tau_RC)
    %d(j)=(5*e_s*A)/C(j)+0.32e-4;  % compute the distance travelled in
high speed regions
    d=[0.15e-4, 0.15e-4, 0.15e-4, 1.01e-4, 1.01e-4, 0.27e-4];  %
compute the distance travelled in high speed regions
    f_tr(j)=2.636*v_sat/(2*pi*d(j))*1/1e9; % compute the frequency due
to transit time as 2.636/(2pi*tau_transit)
    f(j)=f_RC(j)*f_tr(j)/(f_RC(j)+f_tr(j)); % compute the final
frequency
end
```

6.2.3. SENTAURUS_Optical_Simulation

```
File {

        * Input Files

        Grid="detector_msh.tdr"



        * Output Files

        Current="detector_des.plt"
```

```
		Plot="detector_des.tdr"
		Output="detector_des.log"
}

Electrode {
		{Name="Anode_contact" Voltage=0.0}
		{Name="Cathode_contact" Voltage=-4}
}

Physics (Material= "SiliconGermanium") {
		MoleFraction(
				xFraction = 0.3
		)
}

Physics {
		OptBeam((
				WaveLength=783e-7
				WavePower=1.43001e4
				SemAbs (model=RSS)
				SemSurf=0.00
				SemWind=(0.5e-4 0.8e-4)
				WaveTime=(0 50e-13)
				WaveTSigma=1e-20
				*WaveXYSigma=1e-7
		)
		(
				WaveLength=783e-7
```

```
			WavePower=1.43000e4
			SemAbs (model=RSS)
			SemSurf=0.0
			SemWind=(0.5e-4 0.8e-4)
			WaveTime=(50e-13 3e-9)
			WaveTSigma=1e-20
			*WaveXYSigma=1e-7
		))
		Mobility(DopingDep HighFieldSat Enormal)
		EffectiveIntrinsicDensity(OldSlotBoom)
}

Plot {
		OpticalIntensity
		OpticalGeneration
		OptBeam
		eDensity hDensity
		eCurrent hCurrent
		eQuasiFermi hQuasiFermi
		eTemperature
		ElectricField eEparallel hEparallel
		Potential SpaceCharge
		SRHRecombination Auger AvalancheGeneration
		eMobility hMobility eVelocity hVelocity
		Doping DonorConcentration AcceptorConcentration
		ValenceBandEnergy ConductionBandEnergy
}
```

```
Math{
	PeriodicBC(
		(Direction=1
		 Coordinates=(-0.44 0.44)
		)
	)
	-CheckUndefinedModels
	Extrapolate
	Transient=BE
	Iterations=25
	Notdamped=100
	RhsMin=1e-20
	RhsMax=1e+50
	RhsFactor=1e50
}

Solve {
	Coupled(Iterations=100){Poisson}
	Coupled(Iterations=100){Electron}
	Coupled(Iterations=100){Hole}
	Coupled(Iterations=100){Poisson Electron Hole}
	Transient(InitialTime=0 FinalTime=2e-9
		Initialstep=50e-13 Increment=1.1 Decrement=1.2
		 Maxstep=50e-13 Minstep=1e-13)
		{Coupled{Poisson Electron Hole}
		Plot ( Time=(0e-13; 50e-13; 100e-13) NoOverwrite)}
}
```

```
CurrentPlot {
eDensity((0.55, -0.4, 0))
hDensity((0.55, -0.4, 0))
ElectricField(Integrate(Region=SiGe))
}
```

6.2.4. SENTAURUS_Electrical_Simulation

```
File {
	* Input Files
	Grid="detector_msh.tdr"

	* Output Files
	Current="detector_des.plt"
	Plot="detector_des.tdr"
	Output="detector_des.log"
}

Electrode {
	{Name="Anode_contact" Voltage=0.0}
	{Name="Cathode_contact" Voltage=(-4.0 at 50e-13, -4.00001 at 50.1e-13)}
}

Physics (Material= "SiliconGermanium") {
	MoleFraction(
		xFraction = 0.3
	)
}
```

```
Physics {
        OptBeam(
                WaveLength=783e-7
                WavePower=1.43001e4
                SemAbs (model=RSS)
                SemSurf=0.00
                SemWind=(0.5e-4 0.8e-4)
                WaveTime=(0 2e-9)
                WaveTSigma=1e-20
                *WaveXYSigma=1e-7
        )
        Mobility(DopingDep HighFieldSat Enormal)
        EffectiveIntrinsicDensity(OldSlotBoom)
}

Plot {
        OpticalIntensity
        OpticalGeneration
        OptBeam
        eDensity hDensity
        eCurrent hCurrent
        eQuasiFermi hQuasiFermi
        eTemperature
        ElectricField eEparallel hEparallel
        Potential SpaceCharge
        SRHRecombination Auger AvalancheGeneration
        eMobility hMobility eVelocity hVelocity
        Doping DonorConcentration AcceptorConcentration
```

```
    ValenceBandEnergy ConductionBandEnergy
}

Math{
    PeriodicBC(
        (Direction=1
         Coordinates=(-0.44 0.44)
        )
    )
    -CheckUndefinedModels
    Extrapolate
    Transient=BE
    Iterations=25
    Notdamped=100
    RhsMin=1e-20
    RhsMax=1e+50
    RhsFactor=1e50
}

Solve {
    Coupled(Iterations=100){Poisson}
    Coupled(Iterations=100){Electron}
    Coupled(Iterations=100){Hole}
    Coupled(Iterations=100){Poisson Electron Hole}
    Transient(InitialTime=0 FinalTime=2e-9
        Initialstep=50e-13 Increment=1.1 Decrement=1.2
         Maxstep=50e-13 Minstep=1e-13)
        {Coupled{Poisson Electron Hole}
```

```
                Plot ( Time=(0e-13; 50e-13; 100e-13) NoOverwrite)}
}
```

7. Bibliography

[1] J. Bravo-Abad and et al., "Ultrafast photodetection in an all-silicon chip enabled by two-photon absorption," *Applied Physics Letters,* vol. 94, 2009.

[2] P. Gepner and et al., "Evaluating Performance of New Quad-Core Intel Xeon 5500 Family Processors for HPC Parallel Processing and Applied Mathematics," *Springer Berlin / Heidelberg,* vol. 6067, pp. 1-10, 2010.

[3] J. Chang and et al., "A 45nm 24MB on-die L3 cache for the 8-core multi-threaded Xeon Processor," *VLSI Circuits,* pp. 152-153, 2009.

[4] A. L. Shimpi, "http://www.anandtech.com/," AnandTech, 19 November 2008. [Online]. Available: http://www.anandtech.com/show/2671. [Accessed 19 February 2016].

[5] H. Wei and et al., "Compact thermal modeling for temperature-aware design," in *41st annual Design Automation Conference,* San Diego, CA, USA, 2004.

[6] S. Rusu and et al., "A 45 nm 8-Core Enterprise Xeon Processor," *Solid-State Circuits, IEEE Journal of,* vol. 45, pp. 7-14, 2010.

[7] F. Mahony and et al., The future of electrical I/O for microprocessors, 2009, pp. 31-34.

[8] J. S. Orcutt, Monolithic Electronic-Photonic Integration in State-of-the-Art CMOS Processes, Cambridge: Massachusetts Institute of Technology., 2012.

[9] A. Biberman and et al., "First Experimental Bit-Error-Rate Validation of 12.5-Gb/s," *Optical Society of America,* 2010.

[10] M. G. Douglas and et al., "Demonstration of a High Extinction Ratio Monolithic CMOS Integrated Nanophotonic Transmitter and 16 Gb/s Optical Link," *IEEE Journal of Selected Topics in Quantum Electronics,* vol. 21, no. 4, 2015.

[11] I. Young and et al., "Optical I/O Technology for Tera-Scale Computing," *Solid-State Circuits, IEEE Journal of,* vol. 44, pp. 18-31, 2010.

[12] Y. Cheng-Guan and et al., "Quarter-micron optical gate power pHEMT technology," in *Microwave Conference, 2008. APMC 2008,* Asia-Pacific, 2008.

[13] R. Soref and et al., "Electrooptical Effects in Silicon," *IEEE Journal of Quantum Electronics,* vol. 23, no. 1, pp. 123-129, 1987.

[14] A. Mekis, "Lighting up the chip," *Nature Photonics*, vol. 2, pp. 389-390, 2008.

[15] D. G. Rabus, "Ring Resonators: Theory and Modeling," in *Integrated Ring Resonators*, Springer Berlin Heidelberg, 2007, pp. 3-40.

[16] E. Timurdogan and et al., "An ultralow power athermal silicon modulator," *Nature Communications*, pp. 1-11, 2014.

[17] W. Green and et al., "Ultra-compact, low rf power, 10 gb/s silicon," *Optics Express*, vol. 15, no. 25, 2007.

[18] D. Thomson and et al., "50-gb/s silicon optical modulator," *IEEE Photonics Technology Letters*, vol. 24, no. 4, pp. 234-236, 2012.

[19] Q. Xu and et al., "12.5 gbit/s carrier-injection-based silicon micro-ring silicon modulators," *Optics Express*, vol. 15, no. 2, pp. 430-436, 2007.

[20] M. Watts and et al., "Vertical junction silicon microdisk modulators and switches," *Optics Express*, vol. 19, no. 22, 2011.

[21] J. Shainline and et al., "Depletion-mode carrier-plasma optical modulator in zero-change advanced CMOS," *Optics Letters*, vol. 38, no. 15, pp. 2657-2659, 2013.

[22] M. Wade and et al., "Spoked-ring microcavities: enabling seamless integration of nanophotonics in unmodified advanced CMOS microelectronics chips," in *Optical Fiber Communications*, San Francisco, CA, USA, 2014.

[23] L. Alloatti and et al., "High-speed modulator in zero-change CMOS photonics," *Applied Physics Letters*, 2016.

[24] M.-J. Lee and et al., "A silicon avalanche photodetector fabricated with standard CMOS technology with over 1 THz gain-bandwidth product," *Optical Express*, vol. 18, no. 23, pp. 24189-24149, 2010.

[25] H. Meng and et al., "Sub-bandgap polysilicon photodetector in zero-change CMOS process for telecommunication wavelength," *The Optical Society*, vol. 23, no. 15, pp. 32643-32653, 2015.

[26] F. Chou and et al., "Effect of deep n-well bias in an 850-nm Si photodiode fabricated using the CMOS process," *IEEE Photon. Technol. Lett.*, vol. 25, no. 7, pp. 659-662, 2013.

[27] K. Iliyama and et al., "10 GHz bandwidth of Si avalanche photodiode fabricated by standard 0.18 μm CMOS process," in *Proc. OptoElectron. Commun. Conf.*, 2014.

[28] L. Alloatti and et al., "Resonance-enhanced waveguide-coupled silicon-germanium

detector," *Applied Physics Letters,* vol. 108, 2016.

[29] K. Gerasimos and et al., "Sensitive solution-processed," *Nature,* vol. 1, pp. 531-534, 2007.

[30] S. Chen and et al., "“A monolithically-integrated chip-to-chip optical link in bulk CMOS," *IEEE J. Solid-State Circuits,* vol. 50, no. 4, pp. 828-844, 2015.

[31] M. Rakowski and et al., "A 4× 20 Gb/s WDM ring-based hybrid CMOS silicon photonics transceiver," in *Proc. IEEE Int. Solid-State Circuits Conf,* 2015.

[32] K. Yu and et al., "24 Gb/s 0.71 pJ/b Si-photonic source-synchronous receiver with adaptive equalization and microring wavelength stabilization," in *Proc. IEEE Int. Solid-State Circuits Conf.,* 2015.

[33] K. Li and et al., "Silicon photonic transceiver circuits with microring resonator bias-based wavelength stabilization in 65 nm CMOS," *IEEE J. Solid-State Circuits,* vol. 49, no. 6, pp. 1419-1436, 2014.

[34] Y. Liu and et al., "10-Gbps, 5.3-mW optical transmitter and receiver circuits in 40-nm CMOS," *IEEE J. Solid-State Circuits,* vol. 47, no. 9, pp. 2049-2067, 2012.

[35] C. Sun and et al., "A 45 nm CMOS-SOI Monolithic Photonics Platform," *IEEE JOURNAL OF SOLID-STATE CIRCUITS,* 2016.

[36] C. Bulucea, "Recalculation of Irvin's resistivity curves for diffused layers in silicon using updated bulk resistivity data," *Solid-State Electronics,* vol. 36, pp. 489-493, 1993.

[37] M. Rabaey, "The Wire," in *Digital Integrated Circuits: A Design Perspective,* Prentice Hall, 1995, pp. 103-143.

[38] H. Bakoglu, "Interconnection Resistance," in *Circuits, Interconnections, and Packaging for VLSI,* Addison Wesley Longman, 1990, pp. 198 - 201.

[39] Synopsys, "Sentaurus Device User Guide," 2015.

[40] G. Reed and et al., "Silicon Optical Modulators," *Nature Photonics,* vol. 4, pp. 518-526, 2010.

[41] C. Sun and et al., "A 45 nm CMOS-SOI Monolithic Photonics Platform With Bit-Statistics-Based Resonant Microring Thermal Tuning," *IEEE Journal of Solid-State Circuits,* vol. 51, no. 4, pp. 893 - 907, 2016.

[42] S. Hagness, "FDTD Computational Electromagnetics Modeling of Microcavity Lasers and Resonant Optical Structures," NORTHWESTERN UNIVERSITY,

Evanston, Illinois, 1998.